Sensitivity Enhancement of Near Field Probes Using Negative Materials

by

Muhammed Said Boybay

A thesis
presented to the University of Waterloo
in fulfillment of the
thesis requirement for the degree of
Doctor of Philosophy
in
Electrical and Computer Engineering

Waterloo, Ontario, Canada, 2009

I hereby declare that I am the sole author of this thesis. This is a true copy of the thesis, including any required final revisions, as accepted by my examiners.

I understand that my thesis may be made electronically available to the public.

Abstract

In the last decade, design and application of negative materials have been one of the most interesting subjects in the electromagnetic research. The extraordinary properties of double negative (DNG) and single negative (SNG) materials have been studied extensively over this period. In this thesis, one of the unusual properties of negative materials, the evanescent amplification, is used to improve the sensitivity of the near field probes.

The effect of placing DNG and SNG layers between the near field probes and the targets are investigated theoretically. A sensitivity definition is introduced for evanescent probes and it is shown using quantitative measures that the sensitivity can be increased using DNG and SNG materials for a target in vacuum and for a buried target. The electromagnetic loss of the negative materials and the mismatch between the material properties of the host medium and DNG and SNG materials are studied. Using an unmatched DNG layer or SNG layer enhances the sensitivity within an evanescent spectrum range while a lossless and matched DNG layer improves the sensitivity of entire evanescent spectrum.

The idea of using negative materials is implemented over conventional near field probes by numerical experiments. Sensitivities of open-ended waveguides and open-ended coaxial lines for a specific application are studied in the presence of negative materials. In the case of precursor pitting detection on airplane bodies, the sensitivity of an open-ended waveguide probe is increased by 35 times for a $\lambda/10$ sized cubic crack. It is also shown that the negative material increases the quality of the image generated by the probe. The sensitivity improvement is also verified for an open-ended coaxial line. A 11 times improvement is achieved for a similar detection practice, with a $\lambda/20$ sized crack. The effect of coaxial line size and the dielectric material on the sensitivity enhancement are studied.

The improvement is studied theoretically and numerically for an electrically small dipole. Theoretical studies show that when a small dipole is placed within a spherical shell made of DNG materials, the antenna parameters of the dipole becomes more sensitive to the position of a target placed outside the negative material shell. The field distribution generated by a small dipole in a multilayered spherical medium is studied for this purpose. Numerical analysis of a small dipole placed next to a planar DNG layer is presented. The DNG layer increases the sensitivity of the dipole due to a $\lambda/30$ sized metallic target by 5.5 times.

To provide experimental verification, the sensitivity of an electrically small loop is studied. SNG materials with a negative permeability around 1.25 GHz are designed using modified split ring resonators (MSRR). By using the effective parameters of the designed structure, a sensitivity improvement of 10 times is achieved numerically. The improvement is verified using fabricated MSRR structures. The sensitivity of the small loop is enhanced by 9 times for a $\lambda/12.2$ sized metallic target. The sensitivity improvements are achieved within the frequency band where the MSRR structures behave as a μ-negative SNG material.

Acknowledgements

First of all, I would like to express my sincere gratitude to my advisor, Dr. Omar Ramahi. I cannot thank him enough for his guidance and friendly assistance that helped me improve my technical skills and academic knowledge. I believe that having discussions with him is a peerless privilege.

I owe a debt of gratitude to my committee members Dr. Chettypalayam Selvakumar, Dr. Sujeet Chaudhuri and Dr. Kostadinka Bizheva for serving in my examination committee and for their invaluable feedback. I greatly appreciate the time they devoted and their sincere advices. I would like to thank Dr. Mohamed Bakr for participating in my defence exam as the external faculty member.

I would like to thank my colleagues Mohammed Bait-Suwailam, Zhao Ren, Leila Yousefi, Ali Kabiri, Babak Alavikia, Mani Kashanianfard, Hussein Attia and Nael Suwan. Their friendly discussions always inspire new ideas.

Thanks to my former officemates Nezih Topaloglu and Caglar Elbuken. Thank you to Cem E. Sozgen, Serdar Salci and Zekeriya Aksoy. Their friendships gave color to the time I spent in Waterloo.

I extend my deepest thanks to my parents Saadet and Mustafa Boybay, and to my sisters Zeyneb and Zehra for their faithful support and love. I would always be indebted to them.

This research was supported by Research in Motion and the National Science and Engineering Research Council of Canada under the RIM/NSERC Industrial Research Associate Chair Program.

Dedication

To my parents

Contents

List of Tables

List of Figures

Chapter 1

Introduction

1.1 Motivation

Noninvasive detection is a challenging research area with a wide range of applications and solution techniques. The primary applications are material characterization, crack detection on aluminum or steel bodies, land mine detection, defect tests in ICs, and detection of biological anomalies. Although a good number of characterization techniques have been proposed and are being used for these problems using electromagnetic waves, acoustic waves, or chemical vapors, these techniques need to be improved, due to the high false result rates (e.g. 15% in mammography) and difficulties in detecting small targets, such as early stage tumor detection and anti personnel land mine detection [1–4].

Among the aforementioned characterization techniques, microwave near field detection has the potential of considerable improvements. The recently discovered evanescent field amplification phenomenon [5] has the potential of altering classical understanding of near field probes.

By sensing the electrical and magnetic properties of materials, the near field detection technique provides information about the material composition of the sample under test with a subwavelength resolution [6–12]. Generally an electrically small non-radiating tip is used to generate evanescent fields with high spatial frequency [13]. When the evanescent field experiences a change in the electrical properties of the medium, the field distribution in the vicinity of the probe changes leading to a change in the reflection coefficient of the probe.

Near-field probes have been implemented to detect precursor pitting on airplane bodies [11], delamination in IC packages [14,15], fatigue cracks in stainless steel [16], characterization of layered dielectrics [17], etc. Different probe geometries such as open-ended waveguides, open-ended coaxial lines, and microstrip resonator structures are used for these applications. Spatial resolutions as low as $\lambda/750000$ have been achieved [18]. Different control mechanisms are proposed to increase the resolution [19–21].

In order to obtain higher resolutions, higher spatial frequencies are needed in the evanescent spectrum generated by the probe. Since the evanescent fields with high spatial frequencies decay fast, the near-field probe technique is limited to surface or near surface detection schemes. In fact, the probe has to be very close to the sample (almost touching). In Refs. [22, 23], it was shown that the evanescent field amplification property of single negative (SNG) and double negative (DNG) metamaterials can increase the sensitivity and the range of near field detectors. Furthermore, Ref. [23] showed that the sensitivity does not necessarily increase monotonically with the DNG or SNG material thickness.

Methods for designing μ-negative and ϵ-negative metamaterials and the theory of evanescent field amplification were presented in Refs. [5, 24, 25]. In Refs. [26, 27], experimental studies have been conducted to realize such materials, thus providing further support of the theory. Evanescent field amplification was experimentally observed by placing SNG and DNG materials in a waveguide operating in the cutoff regime [28, 29]. In addition, experimental studies for exploring the perfect lens phenomenon, which is a consequence of evanescent field amplification, were presented using split ring resonators [30] and transmission line structures [31–35]. The numerical simulation of the negative materials and their extraordinary properties were reported in the literature [36–40].

Although images of sources with subwavelength resolution have been studied theoretically and experimentally, study of the sensitivity improvement of near field probes has not been reported. In this thesis, the effect of using double negative (DNG) and single negative (SNG) materials on the sensitivity of the near field probes are presented. Theoretical analysis have been conducted to establish a fundamental understanding of using near field probes in conjunction with negative materials. Numerical and experimental studies are conducted for specific probe types and specific applications to verify the theoretical findings.

In the following sections of this chapter, a brief overview of theories and models developed for the study of near field probes is presented. An introduction to negative materials and the outline of the thesis are presented.

1.2 Near Field Probe Theories

In order to present a background on the near field theories, some example studies and discussions are presented in this section. The term near field covers both the microwave regime and the optical regime since they are both governed by the Maxwell's equations. Although the theory and the underlying physics are very similar, there are some differences that are needed to be taken into account. The first difference is the change in the material properties. The ϵ, μ and electromagnetic loss parameters for materials are different in these two regimes. Therefore the operation frequency is scalable as long as the proper material properties are used. Another difference is the homogeneity of the medium. ϵ and μ of the materials are defined by assuming that the piece of material in which the properties are studied is composed of too many atoms or molecules, and these building blocks are much smaller than the operation wavelength. Therefore the microwave and optical theories are interchangeable as long as the medium is homogeneous. In addition, the quantization of the energy is not considered in the electromagnetic theory.

An overview of related techniques and some recent studies are presented in the rest of this section.

Fourier Transform

Analyzing the near field by decomposing to its fourier components first discussed in Ref. [41]. The theory discussed in this study was developed for scanning tunneling microscopy [42–44]. Consequently there are fundamental differences between this microscopy technique and the near field probe sensors. In Ref. [41], it is assumed that the surface to be scanned is illuminated by an external source other than the near field probe. Therefore this study solves the field distribution above a surface when the surface is excited by an external source which is different than the operation principles of the near field probes as described in Chapter 2. Although the solution presented in Ref. [41] intends to solve a different problem, it is summarized in this section because of the use of plane wave decomposition. In the approach presented in Chapter 2 of this thesis, plane wave analysis is conducted. Therefore the Fourier transform study is mentioned in this section.

As outlined in Ref. [45], the incident field ($E_d(r,\omega)$) and the surface profile ($\Gamma(x,y)$) are represented by the Fourier transform as

$$E_d(r,\omega) = \int\int dk_x dk_y F_d(\mathbf{k},\omega) e^{i\mathbf{k}\cdot\mathbf{r}} \tag{1.1}$$

$$\Gamma(x,y) = \int\int dk_x dk_y \gamma(k_x,k_y) e^{i(k_x x + k_y y)}. \tag{1.2}$$

By expressing the $F_d(\mathbf{k}, \omega)e^{i\mathbf{k}\cdot\mathbf{r}}$ term in Eq. 1.1 as a power series of $\Gamma(x, y)$ and by assuming that the surface profile function has a small amplitude, the fourier transform of the field is approximated as

$$F_d(k_x, k_y, \omega) = i(\epsilon' - \epsilon)\gamma(k_x - q_x, k_y - q_y)\mathbf{A}(k_x, k_y) \cdot \mathbf{E}_0(\mathbf{r}, \omega). \tag{1.3}$$

q_x and q_y are the incident wave vector components and E_0 is the field distribution when Γ is zero. $\mathbf{A}$ is a linear transform and can be found in Ref. [45]. As a result, the field distribution can be expressed in terms of the surface profile and the field distribution in the case of a flat surface.

Perturbation Theory

The perturbation theory is used to calculate the frequency shift in a resonator due to a small change in the material properties. By assuming that there is a change in the permittivity and permeability with an unchanged geometry, the resonance frequency shift, $\triangle f_r$, is calculated using [21, 46, 47]

$$\frac{\triangle f_r}{f_r} = \frac{\int_v (\triangle\epsilon \mathbf{E}_1 \cdot \mathbf{E}_0 + \triangle\mu \mathbf{H}_1 \cdot \mathbf{H}_0) dv}{\int_v (\epsilon_0 |E_0|^2 + \mu_0 |H_0|^2) dv} \tag{1.4}$$

where $\triangle\epsilon$ and $\triangle\mu$ are the change in the permittivity and permeability and v is the perturbed volume. $\mathbf{E}_0$ and $\mathbf{H}_0$ are the field distributions without the perturbation and $\mathbf{E}_1$ and $\mathbf{H}_1$ are the field distributions with the perturbation. If the change in the permittivity and permeability are small then the field distributions can be assumed unchanged and the resonance frequency becomes [47]

$$\frac{\triangle f_r}{f_r} = \frac{\int_v (\triangle\epsilon |E_0|^2 + \triangle\mu |H_0|^2) dv}{\int_v (\epsilon_0 |E_0|^2 + \mu_0 |H_0|^2) dv}. \tag{1.5}$$

Note that this approach assumes that the permittivity and permeability of the entire volume are perturbed by the same amount. On the other hand if the change in the material properties is limited to a small part of the cavity, this approach can be used only if the reflection between the perturbed region and unperturbed region is negligible.

Circuit Model

In order to quantify the data obtained from a microscope setup in terms of material properties, the interaction between the probe and the sample was studied in circuit element terms. In Ref. [48], the near field probe was modeled by a small capacitor. The near field probe was assumed to be a sphere and the capacitance between a sphere and a metallic plane was calculated as

$$C = 4\pi\epsilon_0 R_0 \sinh\alpha \sum_{n=2}^{\infty} \frac{1}{\sinh n\alpha}. \tag{1.6}$$

By defining R_0 as the tip radius and g as the separation between the tip and the sample, the other parameters in Eq. 1.6 were expressed as $\alpha = \cosh^{-1}(1 + a')$ and $a' = g/R_0$. Since the interaction between the probe and the surface is modeled by a circuit element, the resonance frequency shift can be calculated as a function of the separation between the tip and the sample.

In addition to the resonance frequency shift, in order to calculate the loss in the conductive plane, the field distribution was calculated in the case of a sphere placed on top of a conducting plane. The boundary conditions were satisfied by summing a series of image charges. In addition, by using the image charges, the application was extended to characterization of thin films in Ref. [49].

As a result, by using the quality factor of the resonator and the field strength on the sample, the loss parameters can be calculated.

Small Dipole

A more accurate solution to a similar structure discussed in the previous part was presented in Ref. [50] in order to understand tip-sample interaction. The authors approximated the tip as a sphere and calculated the field distribution between the probe and the sample by assuming that there is a small dipole at the center of the sphere. The field formulation presented in Ref. [51] for a dipole over an imperfect conductive plane was used. The importance of this theory is the study of full electromagnetic field distribution. On the other hand since the theoretical relation between the dipole strength and the tip geometry was lacking in the original work, the effect of the tip size is not related to the sensitivity of the probe.

Numerical Analysis

In addition to analytical solutions for specific structures, numerical analysis have been widely used to analyze the probe-sample interaction. Some examples of numerical analysis of small tips or waveguide probes can be found in [45, 52–54]. The common approach in this technique is to obtain the field distribution by using a numerical tool and to use the perturbation theory.

1.3 Positive and Negative Materials

In this study, terms positive and negative materials refer to electrical and magnetic properties of the materials. Positive materials have both permittivity ϵ and permeability μ larger than 0. Double negative (DNG) materials have both ϵ and μ negative. Finally single negative (SNG) materials can be either ϵ negative or μ negative. Although some metals behave as ϵ negative SNG materials at optical frequencies, there is no natural μ negative SNG or DNG materials. μ negative SNG or DNG materials, however, can be obtained by periodically structured artificial materials which are described as metamaterials.

The idea of materials having negative ϵ and μ simultaneously was introduced in 1968 by Vaselago, [55]. In his paper, Vaselago analyzed the behavior of propagating waves in double negative (DNG) materials. He showed that the refractive index, n, of a DNG material should be chosen negative, $n = -\sqrt{\epsilon\mu}$, where ϵ and μ are the relative permittivity and permeability of the medium. Using this negative refractive index, he demonstrated that light bends differently at a boundary between a positive and a DNG material, compared to the refraction at a boundary between two positive materials, as shown in Figure 1.1. Due to the fact that DNG materials were not realizable until late 90s, scientists never gave sufficient interest to the double negative phenomenon.

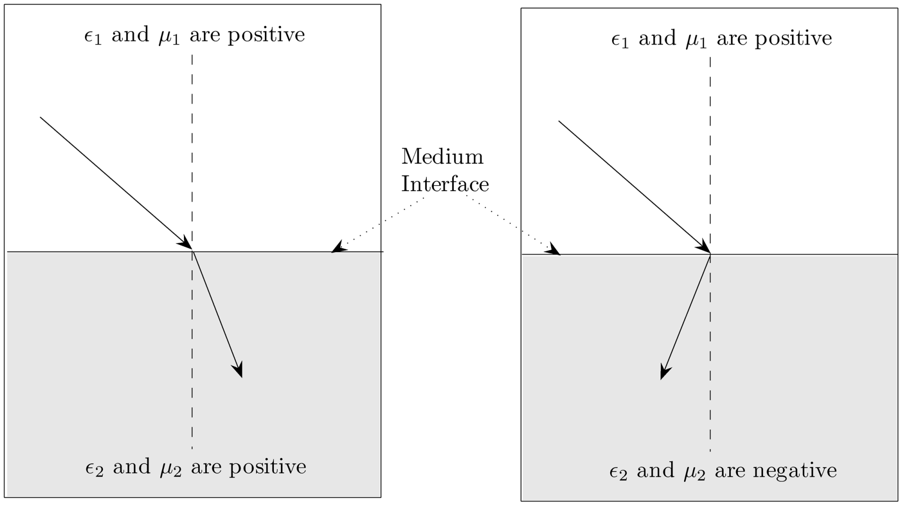

Figure 1.1: Ray refraction (a) for a positive-positive boundary and (b) for a positive-negative boundary

In 2000, two major breakthroughs guided attentions of many scientists to the DNG materials. The first one was the experimental realization of the DNG materials using split ring resonators [56], as discussed in Chapter 6. This invention was followed by Pendry's theoretical work showing evanescent field amplification and perfect lens [5] concepts. Other than the different refraction characteristics and evanescent field amplification, DNG materials exhibit some other extraordinary properties. The reversed Doppler effect and reversed Cherenkov radiation are examples of these extraordinary properties.

Among the unusual properties of the negative materials, evanescent field amplification is the main interest of this work. Although it has been shown that a perfect lens cannot be manufactured using realistic DNG materials [57, 58], it was demonstrated that the DNG materials amplify evanescent fields and superlensing effect is realizable [59–64]. An analysis of the transmission characteristics of DNG slabs is presented in Appendix A where the theoretical background of the evanescent field amplification is discussed.

1.4 Outline of the Thesis

This thesis consists of six chapters in addition to the Introduction. In Chapter 2, the sensitivity of evanescent field probes is investigated theoretically in the presence of a layer made of DNG and SNG materials. Chapters 3 and 4 present the application of the sensitivity improvement to the open-ended waveguides and open-ended coaxial lines. Chapter 5 presents the theoretical analysis of the sensitivity of an electrically small dipole placed in a spherical DNG shell. The numerical analysis of small dipoles placed next to a negative layer is also presented in this chapter. Chapter 6 presents experimental validation of the sensitivity improvement. The sensitivity of an electrically small loop is studied experimentally and numerically. Finally, in Chapter 7, the contributions and possible potential research directions are summarized.

Chapter 2

Theory of Evanescent Field Probes with Metamaterials

2.1 Introduction

Evanescent field imaging is a powerful surface characterization technique and a promising method for non-invasive subsurface imaging. The technique senses electrical and magnetic properties of materials with subwavelength resolution. Resolution values as low as $\lambda/10^6$ [65] have been reported. The technique has been used on various materials, such as biological samples [66], circuit boards [67] or semiconductor samples [12]. A more recent application of the method for subsurface imaging focused on the detection of corrosion precursor pitting [11]. However, due to the fast decay of evanescent fields, the technique in Ref. [11] was limited to detection of targets buried under a layer of thin paint.

Since evanescent or near-field imaging has the capability to detect changes in the electrical and magnetic properties of materials, it is a strong candidate to detect biological anomalies, land mines and hidden or subsurface objects. A comparison between the penetration characteristics of propagating and evanescent fields is presented in Appendix B. In Ref. [68], it was shown that super-resolution images can be constructed in half space problems if the evanescent field components are captured. For these diverse applications, the common challenge is the sensitivity of the evanescent field probes.

Recent developments in the double negative (DNG) and single negative (SNG) metamaterials offer a solution to these problems. By using the evanescent field amplification property, DNG or SNG based superlenses can be used to improve the sensitivity and range of the evanescent probe imaging methods.

DNG materials have gathered the attention of many scientists and engineers since the discovery of superlensing effect [5] and the physical realization of DNG materials [26]. Theoretical field calculations in DNG materials and transmission through a DNG lens were reported in previous works [5, 62, 63]. In Ref. [69], the superlensing effect was combined with the nonlinear inverse scattering algorithms and was used for achieving subwavelength resolution images. Since DNG materials are dispersive and lossy, there are practical limitations on the superlensing effect [58]. The nature of DNG materials makes it impossible to have a perfect lens, whereas the superlensing effect, which refers to the subwavelength resolution capabilities of such lenses by evanescent field amplification, can be realized under less severe conditions.

Numerical methods using the finite difference time domain (FDTD) [70,71] and finite element methods (FEM) [72, 73] were implemented to simulate DNG materials. The evanescent field amplification and superlensing effect were demonstrated numerically. Experimental verifications of these extraordinary behaviors were achieved by using two dimensional transmission lines grids loaded with circuit elements [31] and split ring resonator structures [28,30] for DNG materials, and by using silver superlenses [74] for SNG materials.

Although the theory of the evanescent field imaging using DNG materials, in the context of superlensing, is well developed, its application to evanescent probe imaging has not been fully explored since the previous studies focused on detecting the evanescent spectrum emanating from an object [5,75]. An evanescent (or near-field) probe, in essence, operates by measuring the energy change in the surroundings of the probe tip. The objectives of this chapter are to take a different look at near field probes and to study the following aspects:

- To develop a model for near field probes based on multilayer structures.
- To develop a measure of sensitivity for the above model.
- To introduce the DNG and SNG layers to the model and to study the effect on the sensitivity.
- To verify the theoretical calculations with numerical simulations.

In Section 2.2, formulation of evanescent fields and comparison between propagating and evanescent fields are presented. In Section 2.3, independent of the probe media, a definition for sensitivity based on the electric and magnetic energy stored in the vicinity of the probe is introduced. In Section 2.4, theoretical calculations of the sensitivity applied to a theoretical probe acting on multi-layered media and targets are presented, and sensitivity enhancement is shown when using DNG and SNG lenses. In Sections 2.5 and 2.6, numerical simulation results for test cases are presented. Conclusions are presented in Section 2.7.

2.2 Formulation of Evanescent Fields

Electromagnetic fields have to satisfy Maxwell's Equations. Maxwell's Equations for a non-dispersive and isotropic medium are given as

$$\nabla \cdot \mathbf{E(t)} = \frac{\rho}{\epsilon} \tag{2.1}$$

$$\nabla \cdot \mathbf{H(t)} = 0 \tag{2.2}$$

$$\nabla \times \mathbf{E(t)} = -\mu \frac{\partial \mathbf{H(t)}}{\partial t} \tag{2.3}$$

$$\nabla \times \mathbf{H(t)} = \mathbf{J(t)} + \epsilon \frac{\partial \mathbf{E(t)}}{\partial t} \tag{2.4}$$

where, $\mathbf{E}$ is the electric field, $\mathbf{H}$ is the magnetic field, $\mathbf{J}$ is the current density, ρ is the electric charge density, ϵ is the permittivity of the medium and μ is the permeability of the medium. If $e^{j\omega t}$ is chosen as the time dependence, the phasor forms of Maxwell Equations become

$$\nabla \cdot \mathbf{E} = \frac{\rho}{\epsilon} \tag{2.5}$$

$$\nabla \cdot \mathbf{H} = 0 \tag{2.6}$$

$$\nabla \times \mathbf{E} = -j\omega\mu\mathbf{H} \tag{2.7}$$

$$\nabla \times \mathbf{H} = \mathbf{J} + j\omega\epsilon\mathbf{E} \tag{2.8}$$

where ω is the angular frequency. Throughout this thesis, field and current expressions refer to these phasor notations, unless otherwise stated. Using these equations, the vector Helmholtz Equations in a medium without any free current source can be found as

$$\nabla^2\mathbf{E} + k^2\mathbf{E} = 0 \tag{2.9}$$

$$\nabla^2\mathbf{H} + k^2\mathbf{H} = 0 \tag{2.10}$$

where k is given as

$$k = \omega\sqrt{\mu\epsilon}. \tag{2.11}$$

Evanescent fields propagate in one direction while decaying in another. In order to describe and analyze evanescent fields, the solutions of Eqs. 2.9 and 2.10 for E-waves and for H-waves are needed. The general solution for an H-wave with $\hat{y}$ polarized E-field can be found as

$$\mathbf{E} = \hat{y}E_0 e^{-j\mathbf{k}\cdot\mathbf{r}} \tag{2.12}$$

$$\mathbf{H} = (\hat{z}k_x - \hat{x}k_z)\frac{E_0}{\mu\omega}e^{-j\mathbf{k}\cdot\mathbf{r}} \tag{2.13}$$

and the solution for an E-wave with $\hat{y}$ polarized H-field is

$$\mathbf{H} = \hat{y}H_0 e^{-j\mathbf{k}\cdot\mathbf{r}} \tag{2.14}$$

$$\mathbf{E} = (\hat{x}k_z - \hat{z}k_x)\frac{H_0}{\epsilon\omega}e^{-j\mathbf{k}\cdot\mathbf{r}} \tag{2.15}$$

where E_0 and H_0 are the E-field and the H-field amplitudes, respectively. $\mathbf{k}$ and $\mathbf{r}$ vectors are given as

$$\mathbf{k} = \hat{x}k_x + \hat{z}k_z \tag{2.16}$$

$$\mathbf{r} = \hat{x}\mathrm{x} + \hat{y}\mathrm{y} + \hat{z}\mathrm{z} \tag{2.17}$$

and the dispersion relation is

$$|\mathbf{k}|^2 = k_x^2 + k_z^2 = \omega^2\mu\epsilon. \tag{2.18}$$

In a lossless medium, if the wave has real $\mathbf{k}$ components, which corresponds to having real k_x and k_z for the fields described above, then the wave is called a propagating wave. This type of waves have a constant field amplitude over a phase front. Furthermore, the field strength does not change from one phase front to another as shown in Fig. 2.1. Now assume that the wave has a k_x component greater than $|\mathbf{k}| = \omega\sqrt{\mu\epsilon}$, then using dispersion relation, Eq. 2.18,

$$k_z^2 = \omega^2\mu\epsilon - k_x^2 \tag{2.19}$$

$$\Rightarrow k_z = \pm j\sqrt{k_x^2 - \omega^2\mu\epsilon} \tag{2.20}$$

can be found. The waves that can be expressed in an arbitrary cartesian coordinate system with a $\mathbf{k}$ composed of a purely imaginary component and a purely real component are called evanescent fields. If the phase propagation is assumed in $\hat{x}$ and imaginary $\mathbf{k}$ component is assumed in the $\hat{z}$ direction, the E-field in Eq. 2.13 becomes

$$\mathbf{E} = \hat{y}E_0 e^{-jk_z z} e^{-jk_x x} \tag{2.21}$$

$$\mathbf{E} = \hat{y}E_0 e^{\pm\sqrt{k_x^2 - \omega^2\mu\epsilon}z} e^{-jk_x x}. \tag{2.22}$$

The sign of Eq. 2.20 is chosen according to boundary conditions of the structure. If the medium has positive permittivity and permeability, the field has a decaying amplitude

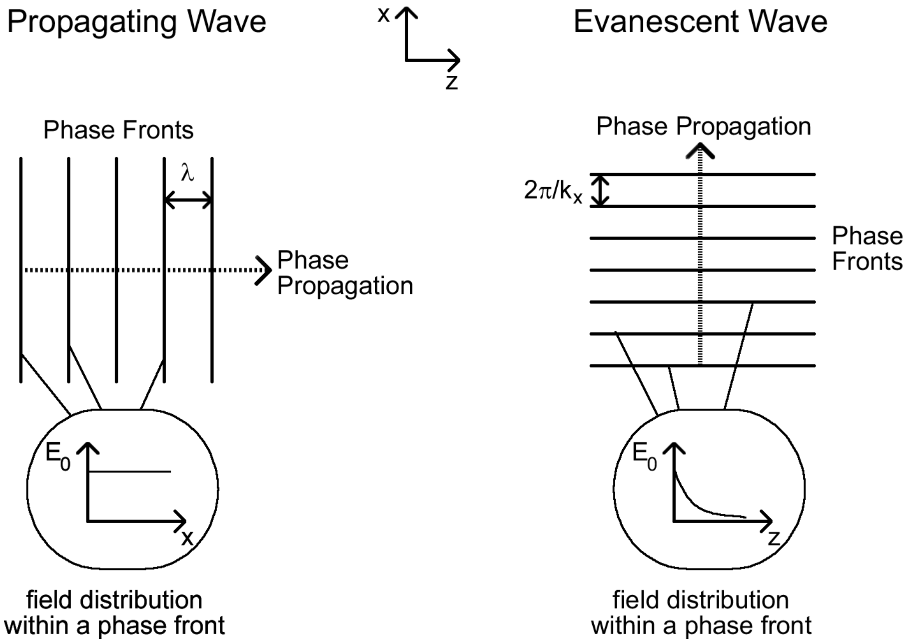

Figure 2.1: Comparison of a propagating wave in $\hat{z}$ direction and an evanescent field decaying in $\hat{z}$ direction.

as the observation point moves away from the source. Definitions of the evanescent and propagating waves are specific for time harmonic fields and they are defined for cartesian coordinates. On the other hand, spherical and cylindrical coordinates do not have the classification of evanescent and propagating fields. However, fields described in spherical and cylindrical coordinate systems can be transformed to the cartesian coordinates [76] and they can be expressed as a summation of propagating and evanescent plane waves.

Analyzing phase fronts of propagating and evanescent fields is helpful in order to understand the difference between these two types of fields. Fig. 2.1 shows the phase fronts of a propagating wave with $\mathbf{k} = \hat{z}k_z$ and an evanescent wave as described in Eq. 2.22. Counter to the propagating waves, the phase front of an evanescent field does not have a constant amplitude distribution. Within a phase front, the amplitude decays as the observation point moves away from the source. This is the major difference between a propagating and an evanescent wave. On the other hand, all phase fronts are identical for both evanescent and propagating waves.

Although evanescent waves have decaying amplitudes, these waves do not dissipate energy as long as the medium is lossless. This is because the amplitude distribution does not change from one phase front to another and the power flow is in the direction of phase propagation. Thus, the sign selection in Eq. 2.20 is not a result of energy conservation, but is a result of the fact that if evanescent fields do not decay, radiating systems cannot reach steady state.

The power flow for evanescent fields can be found using the Poynting vector, $\mathbf{S} = \mathbf{E} \times \mathbf{H}^*$. The time averaged power density is given by

$$I = \frac{1}{2}\mathtt{Re}\{S\}. \tag{2.23}$$

For a wave described in Eq. 2.22, the power flow becomes

$$I = \hat{x}\frac{k_x E_0^2}{\eta k} e^{\mp 2\sqrt{k_x^2 - k^2} z}, \tag{2.24}$$

where the wave impedance is defined as $\eta = \frac{\mu}{\epsilon}$. Eq. 2.24 shows that the power flow is in $\hat{x}$ direction and the amplitude decay is in $\hat{z}$ direction, so there is no power dissipation.

2.3 Quantification of Sensitivity

2.3.1 Sensitivity

Evanescent probe detectors measure the evanescent field energy stored in the surrounding of the radiator tip. Any antenna, or any radiating system, can be modeled by a simple lumped circuit with passive elements if the system is linear. A load connected to a transmission line can be modeled as an impedance, $Z = R + jX$. The real part of the impedance, R, corresponds to the radiated propagating power and the loss of the system. The reactance, X, is related to the stored energy. Fig. 2.2 shows a depiction of the probe (which is assumed here without loss of generalization as a cavity with a thin wire, or tip, extending out of it). Also shown in Fig. 2.2 a transmission line model of the probe. Placing a target in the proximity of the probe is analogous to altering the terminal load of the transmission line, say from $R + jX$ to $R' + jX'$. A change in the terminal load would then affect the reflection coefficient which is represented by the scattering parameter S_{11} (see Fig. 2.2(c)). The change in the reflection coefficient (frequency shift, magnitude shift, or both) reflects a change in the resonant frequency of the probe due to the presence of the target. Therefore a target can be detected easier if it leads to a higher change in the reactance.

Since the change in reactance that the probe reacts to is in essence a distributed load, the load is considered to be the entire volume surrounding the tip of the probe, or more precisely, the entire volume where the field distribution is nonzero. Next, the resistance and the reactance of the terminal load are expressed in terms of the total fields in the

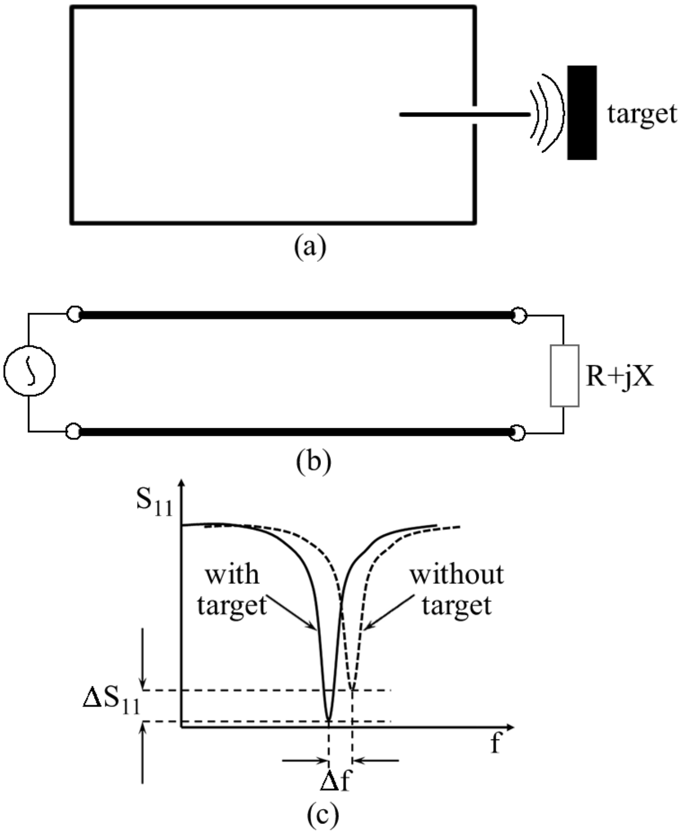

Figure 2.2: A generic probe is depicted by a cavity with a thin wire or tip coming out of it (a). The probe is modeled as a transmission line with a certain terminal impedance (b). A probe encountering a target is analogous to changing the terminal impedance of the transmission line, thus leading to a shift in S11 (c).

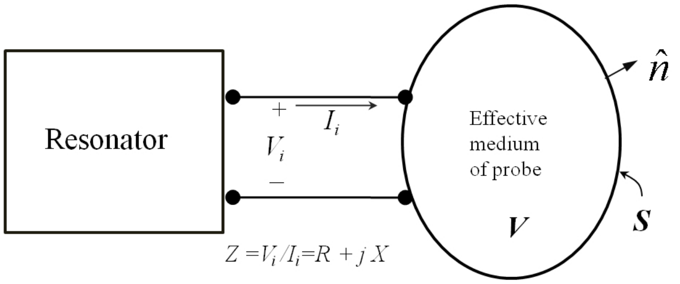

Figure 2.3: The three components representing a generic probe: The resonator, the interface with the material to be interrogated (the interface is represented here as a short transmission line) and the probe medium which is a volume containing all the electric and magnetic energies excited by the resonator in the presence of the target medium.

vicinity of the probe. The resistance and the reactance can be expressed as [77]

$$R = \frac{1}{|I_i|^2}\left[\mathrm{Re}\left\{\int_V (\mathbf{J}^* \cdot \mathbf{E})dv\right\} + 2\oint_A (\mathbf{S}\cdot\mathbf{n})da + 4\omega\mathrm{Im}\left\{\int_V (u_h - u_e)dv\right\}\right] \tag{2.25}$$

$$X = \frac{1}{|I_i|^2}\left[4\omega\mathrm{Re}\left\{\int_V (u_h - u_e)dv\right\} - \mathrm{Im}\left\{\int_V (\mathbf{J}^* \cdot \mathbf{E})dv\right\}\right] \tag{2.26}$$

where $\mathbf{J}$ is the current density, $\mathbf{E}$ is the electric field, and u_h and u_e are the energy densities due to the magnetic and electric fields, respectively, in the volume V. $\mathbf{S}$ is the Poynting vector on the surface that encloses V and n is the normal vector of the surface pointing out of V as shown in Fig. 2.3. I_i is the current passing through the load, Z.

The first term of Eq. (2.25) and the second term of Eq. (2.26) are due to the conductive losses and they are equal to zero for a lossless medium. The $(u_h - u_e)$ difference is equal to zero for a propagating plane wave and it is purely real for an evanescent plane wave in a lossless medium. The second term in Eq. (2.25) is the power radiated from the surface A and is negligible for near-field probes. For a propagating wave in a lossless medium Eq. (2.25) reduces to the second term and Eq. (2.26) is equal to zero. For an evanescent wave, however, the first term in Eq. (2.26) is the only parameter that contributes to the impedance.

Therefore the sensitivity can be defined as the deviation of the ratio of difference between total $\mathbf{H}$ and $\mathbf{E}$ field energies in the presence of the target to the total energy without the target:

$$Sensitivity = \left|1 - \frac{(U_h - U_e)_{with\ target}}{(U_h - U_e)_{without\ target}}\right|, \tag{2.27}$$

where

$$U_{h,e} = \int_V u_{h,e}dv. \tag{2.28}$$

According to the definition proposed in Eq. (2.27), the deviation from zero, which can only take place if a target is present, is a measure of higher sensitivity. From this sensitivity definition, it is not intuitive that the amplification of evanescent fields, as a consequence of using a superlens, would lead to increased probe sensitivity. This sensitivity definition (i.e., Eq. (2.27)), as will be shown below, is not intended to quantify the sensitivity for specific targets but rather to be used as a tool or a measure to investigate the potential of near-field probes when used in conjunction with DNG media, SNG media, or, in fact, with any media in general.

2.3.2 Probe-Target Model using Plane Waves

Unlike earlier works where the near-field (or evanescent field) probes were modeled using lumped elements, in this work, a novel field model for the probe-target interaction is presented. This model is developed by using multi-layer media to represent the target and its media. While, in theory, there is always small radiation coming out of the resonator used in near-field imaging, the magnitude of these propagating field components are small enough to warrant their exclusion from our model. Therefore, the energy coming from the resonator is represented as evanescent plane waves. Since all time-harmonic fields can be expressed as a superposition of plane waves [76], the evanescent spectrum can be analyzed using the following formulation and the over all response of a probe is a combination of the responses of plane waves present in its spectrum.

In general, the target to be detected is embedded inside some *target medium*. Usually the target is electrically-small and is of finite size. However, for the purpose of developing our probe-target model, a target which is a single layer, occupying the space $Z_3 < z < Z_4$, as shown in Fig. 2.4 will be considered. Furthermore, the target can be backed by a multi-layer medium. Therefore, in order to provide flexibility in the number of layers that correspond to the complexity of the structure, the fields are calculated for an arbitrary n number of boundaries. The coefficients are defined in a way that the solution can be calculated recursively.

In most practical applications, such as the examples presented later in this dissertation, the target is not an infinite layer but rather localized in space. However, irrespective of the nature of the target, when it is interrogated with an evanescent field, a spectrum of traveling and evanescent plane waves are generated. In either case, whether the target is localized or not, an evanescent spectrum is generated. Therefore, it is purely for the purpose of developing a succinct mathematical theory for sensitivity enhancement that the infinite layer target is considered.

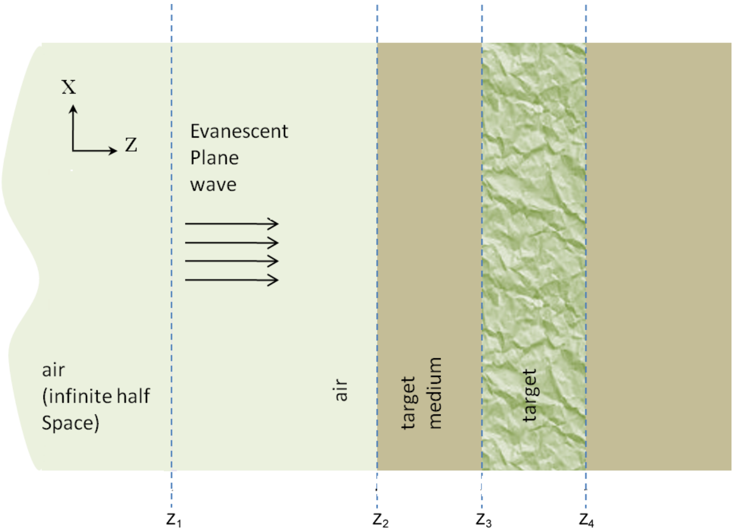

Figure 2.4: The probe and target interaction is modeled by a plane wave in a multilayered structure. The incident field is assumed to be excited at Z_1, which represents the probe location. The last region is assumed to be an infinite half space.

Assuming a time-harmonic incident field in the left-hand half space in the form of

$$\mathbf{E} = \hat{y} e^{j(k_x x + k_{z,1} z)}, \tag{2.29}$$

the field distribution can be found using the boundary conditions assuming that the first and last regions are infinite half spaces [78]. On the m^{th} boundary, the transmission and reflection coefficients are defined as t_m and r_m, respectively. Evanescent plane waves are defined using their **k** components parallel to the interfaces between the layers since this component does not change from one layer to another. When there is an incident wave with a parallel **k** component of k_x and an E-field in $\hat{y}$ direction, transmission and reflection coefficients defined in Fig. 2.5 can be found as

$$t_m = \frac{2k_{z,m}\mu_{m+1}e^{jk_{z,m}z_m}}{(k_{z,m}\mu_{m+1} + k_{z,m+1}\mu_m)e^{jk_{z,m+1}z_m} + r_{m+1}(k_{z,m}\mu_{m+1} - k_{z,m+1}\mu_m)e^{-jk_{z,m+1}z_m}} \tag{2.30}$$

$$r_m = t_m\left(\frac{e^{jk_{z,m+1}z_m} + r_{m+1}e^{-jk_{z,m+1}z_m}}{e^{-jk_{z,m}z_m}}\right) - e^{2jk_{z,m}z_m} \tag{2.31}$$

for $1 \leq m \leq n-1$, and

$$t_n = \frac{2k_{z,n}\mu_{n+1}e^{j(k_{z,n}-k_{z,n+1})z_n}}{(k_{z,n}\mu_{n+1} + k_{z,n+1}\mu_n)} \tag{2.32}$$

$$r_n = t_n e^{j(k_{z,n}+k_{z,n+1})z_n} - e^{2jk_{z,n}z_n} \tag{2.33}$$

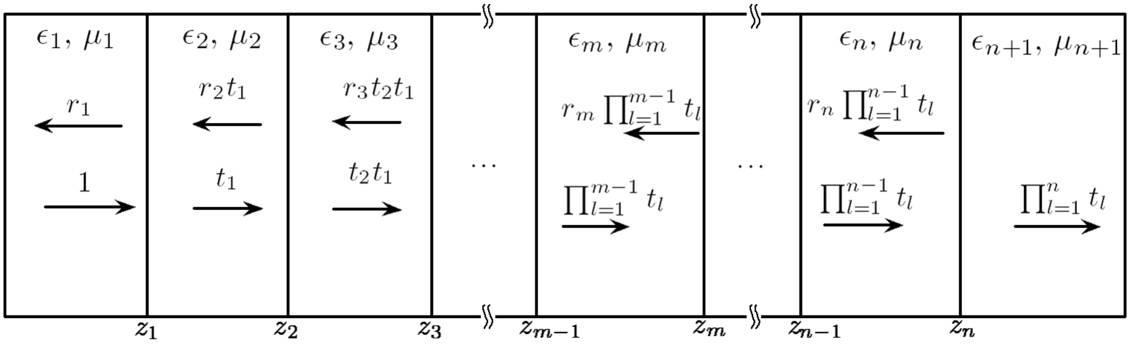

Figure 2.5: The general multilayer structure used for the field and energy calculations. The first and last regions are infinite half spaces.

where the dispersion relation is given as

$$k_{z,m}^2 = \omega^2 \epsilon_m \mu_m - k_x^2. \tag{2.34}$$

Consequently the **E** and **H** fields become

$$\mathbf{E}_m = \hat{y} \prod_{l=1}^{m-1} t_l (e^{jk_{z,m}z} + r_m e^{-jk_{z,m}z}) \tag{2.35}$$

$$\begin{aligned}\mathbf{H}_m =& \hat{z}\frac{k_x}{\omega\mu_m} \prod_{l=1}^{m-1} t_l (e^{jk_{z,m}z} + r_m e^{-jk_{z,m}z}) - \\ & \hat{x}\frac{k_{z,m}}{\omega\mu_m} \prod_{l=1}^{m-1} t_l (e^{jk_{z,m}z} - r_m e^{-jk_{z,m}z})\end{aligned} \tag{2.36}$$

for $1 \leq m \leq n$, and for the last half space

$$\mathbf{E}_{n+1} = \hat{y} \prod_{l=1}^{n} t_l e^{jk_{z,m}z} \tag{2.37}$$

$$\mathbf{H}_{n+1} = \frac{(\hat{z}k_x - \hat{x}k_{z,n})}{\omega\mu_n} \prod_{l=1}^{n} t_l e^{jk_{z,m}z} \tag{2.38}$$

2.3.3 Near-Field Probe Employing Double Negative Media

Double negative media (DNG) has two primary features: First, it allows for phase propagation in opposite direction to that of the direction of energy propagation (**k** vector and Poynting vector **S** are 180^o out of phase). The second important feature is the amplification of evanescent field magnitude. Both features have been used with much excitement in the past to reproduce the image of a source [30,31,74]. The second feature, namely the amplification of evanescent fields, is clearly relevant to the field of near-field microscopy.

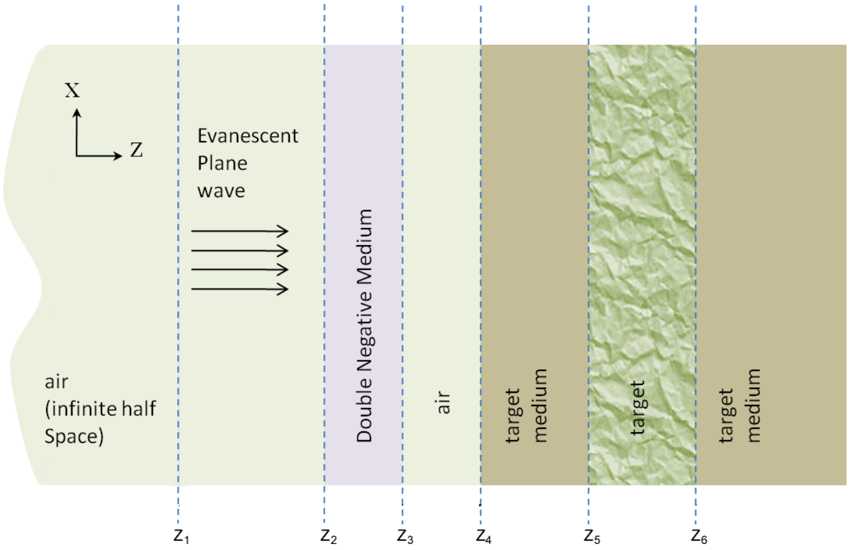

Figure 2.6: A DNG slab is inserted between the target medium and the field excitation

What remains uncertain, however, is whether evanescent field enhancement translates into increased probe sensitivity in the sense defined in Eq. (2.27).

To this end, the field solutions developed above which are valid for propagating and evanescent plane waves are considered. A DNG medium between the probe tip and the target medium, as shown in Fig. 2.6 is inserted. For a DNG layer, the sign of $k_{z,m}$ must be selected the opposite of the sign in the case of a positive medium (for a good discussion on the compatibility between the mathematics and physics of DNG media, the reader is referred to Refs. [62] and [63]).

The energy and sensitivity are calculated using field distributions. For the energy calculations, the DNG layer is represented as a dispersive medium. Thus, frequency dependence of permittivity of the DNG medium is assumed to be the same as the permittivity function of a metal around its plasma frequency, which is a commonly used model for DNG medium simulations. The frequency dependent permittivity and permeability are given as

$$\epsilon(\omega) = \epsilon_0 \left(1 - \frac{\omega_p^2}{\omega(\omega - j\Gamma_e)}\right) \tag{2.39}$$

$$\mu(\omega) = \mu_0 \left(1 - \frac{\omega_p^2}{\omega(\omega - j\Gamma_m)}\right), \tag{2.40}$$

where ω_p is the plasma frequency and Γ_e and Γ_m represent the loss of the DNG medium [79].

For the lossless case, energy densities of the **E** and **H** fields for a linear medium can be found as [77]

$$u_e = \frac{1}{2}\frac{\partial(\omega\epsilon(\omega))}{\partial\omega}|\mathbf{E}|^2 \tag{2.41}$$

$$u_h = \frac{1}{2}\frac{\partial(\omega\mu(\omega))}{\partial\omega}|\mathbf{H}|^2. \tag{2.42}$$

For a lossless plasma at $\omega = \frac{\omega_p}{\sqrt{2}}$ the effective relative permittivity is equal to -1. Therefore

$$\left.\frac{\partial(\omega\epsilon(\omega))}{\partial\omega}\right|_{\omega=\frac{\omega_p}{\sqrt{2}}} = 3\epsilon_0. \tag{2.43}$$

Similarly the derivative term in the **H** field energy density is equal to $3\mu_0$.

If there are n number of boundaries, the total **E** field energy in the m^{th} slab, defined by $z_{m-1} \leq z \leq z_m$, can be written as

$$U_{e,m} = \prod_{l=1}^{m-1} t_l^2 \frac{\partial(\omega\epsilon(\omega))}{\partial\omega} \times \left[r_m(z_m - z_{m-1}) + \frac{e^{2jk_{z,m}z_m} - e^{2jk_{z,m}z_{m-1}}}{4jk_{z,m}} + \frac{r_m^2(e^{-2jk_{z,m}z_{m-1}} - e^{-2jk_{z,m}z_m})}{4jk_{z,m}}\right]. \tag{2.44}$$

Eq. (2.44) is valid for $1 \leq m \leq n$. Finally for the last half space region, assuming a positive and non dispersive medium, the energy becomes

$$U_{e,n+1} = -\prod_{l=1}^{n} t_l^2 \frac{\epsilon_{(n+1)} e^{2jk_{z,(n+1)}z_n}}{4jk_{z,(n+1)}}. \tag{2.45}$$

The energy due to the $\hat{x}$ component of the **H** field is

$$U_{hx,m} = \prod_{l=1}^{m-1} t_l^2 \frac{\partial(\omega\mu(\omega))}{\partial\omega}\left(\frac{k_{z,m}}{\omega\mu_m}\right)^2 \times \left[-r_m(z_m - z_{m-1}) + \frac{e^{2jk_{z,m}z_m} - e^{2jk_{z,m}z_{m-1}}}{4jk_{z,m}} + \frac{r_m^2(e^{-2jk_{z,m}z_{m-1}} - e^{-2jk_{z,m}z_m})}{4jk_{z,m}}\right] \tag{2.46}$$

for $1 \leq m \leq n$ and

$$U_{hx,n+1} = -\prod_{l=1}^{n} t_l^2 \left(\frac{k_{z,(n+1)}}{\omega}\right)^2 \frac{e^{2jk_{z,(n+1)}z_n}}{4j\mu_{(n+1)}k_{z,(n+1)}}. \tag{2.47}$$

The energy due to the $\hat{z}$ component of the **H** field is

$$U_{hz,m} = \frac{\partial(\omega\mu(\omega))}{\partial\omega}\left(\frac{\partial(\omega\epsilon(\omega))}{\partial\omega}\right)^{-1}\left(\frac{k_x}{\omega\mu_m}\right)^2 U_{e,m}. \tag{2.48}$$

Energy Calculation in Dispersive and Lossy Media

For a lossy, dispersive medium, Eqs. (2.41) and (2.42) are not valid [80]. By simplifying the general solution presented in Ref. [80] for a time harmonic field in a Drude medium, the **E** field energy density can be found as [81]

$$u_e = \frac{1}{2}\epsilon_0 \left(1 + \frac{\omega_p^2}{\omega^2 + \Gamma_e^2}\right) |\mathbf{E}|^2. \tag{2.49}$$

Therefore replacing the $\frac{\partial(\omega\epsilon(\omega))}{\partial w}$ term in Eq. 2.44, by $\epsilon_0(1 + \frac{\omega_p^2}{\omega^2+\Gamma_e^2})$ yields the energy equations that is compatible with the lossy cases. Similarly the **H** field energy density can be found as

$$u_h = \frac{1}{2}\mu_0 \left(1 + \frac{\omega_p^2}{\omega^2 + \Gamma_m^2}\right) |\mathbf{H}|^2. \tag{2.50}$$

2.4 Theoretical Results

In this section, the sensitivity as defined in Eq. (3) for different media and target configurations is calculated. Differences in the transmission characteristics of DNG and SNG layers followed by the sensitivity improvement analysis are presented. The sensitivity discussion is focused on the changes in the sensitivity as a result of using lossless and lossy matched DNG lenses, and then the effects of using SNG and unmatched DNG lenses are discussed. The term *matched* refers to the case when the permittivity (ϵ') and permeability (μ') of the DNG lens is equal to the negative of permittivity (ϵ) and permeability (μ) of the next layer, respectively.

2.4.1 Comparison of Transmission Characteristics

Since the matched condition satisfies $\epsilon'\mu' = \epsilon\mu$, $k'_z = k_z$ is also satisfied. As a result the reflection coefficient reduces to 0 and the transmission coefficient reduces to $e^{jk_z a}$. Therefore the DNG layer amplifies the evanescent fields with an amplification constant equal k_z. As a result the DNG layer amplifies the whole evanescent spectrum with a well defined exponential function.

In the case of an unmatched DNG layer, the condition $k'_z = k_z$ is not satisfied anymore. Therefore the transmission coefficient is not reduced to a simple exponential function. Furthermore, the reflection and transmission coefficients have a singularity when the condition

$$e^{-jk'_z a} = \frac{(k_z\epsilon' + k'_z\epsilon)^2}{(k_z\epsilon' - k'_z\epsilon)^2} \tag{2.51}$$

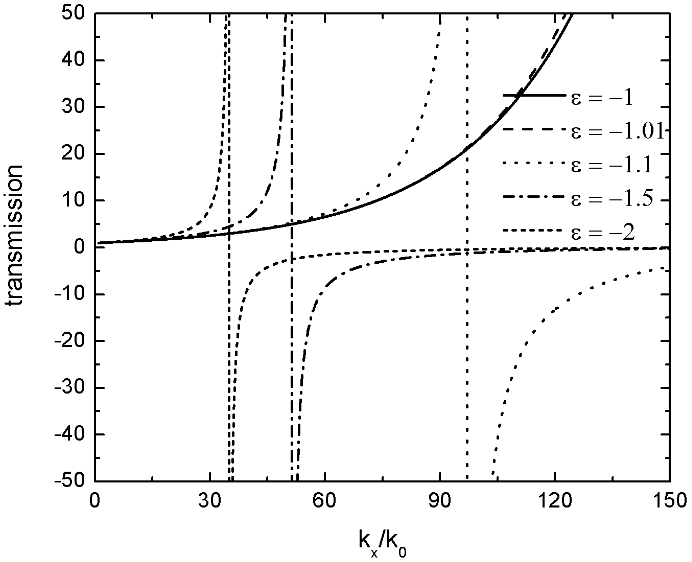

Figure 2.7: The transmission coefficient as a function of normalized parallel **k** component. The layer thickness is $\lambda/200$. $\epsilon = -1$ is the matched case with the exponential amplification is observed. When the layer is not matched, a singularity is observed in the transmission.

is satisfied. Note that this condition cannot be satisfied when the layer is a double positive material or when the incident field is not an evanescent field.

Fig. 2.7 shows the transmission coefficient as a function of the normalized parallel **k** component for different ϵ' values. The thickness of the layer is $\lambda/200$. When the layer is matched, the response is an exponential function. When the layer is not matched, the transmission singularities are observed. As the mismatch is increased the singularity location is shifted to lower k_x values. The amplification characteristic of unmatched layers can be analyzed in three regions. The first region is before the singularity location, where the amplification is very close to the matched case. In the second region, around the singularity, the amplification much higher compared to the matched case. And finally in the third region, far from the singularity, the amplification is not as high as the matched case. Therefore the unmatched layers do not amplify the entire evanescent spectrum. Amplification is limited by the singularity location.

Fig. 2.8 shows the case with a $\lambda/100$ thick DNG layer. The amplification of the matched layer is increased as expected. The singularity locations of the unmatched DNG layers are shifted towards lower k_x values. Therefore thicker unmatched DNG layers amplifies a smaller portion of the evanescent spectrum.

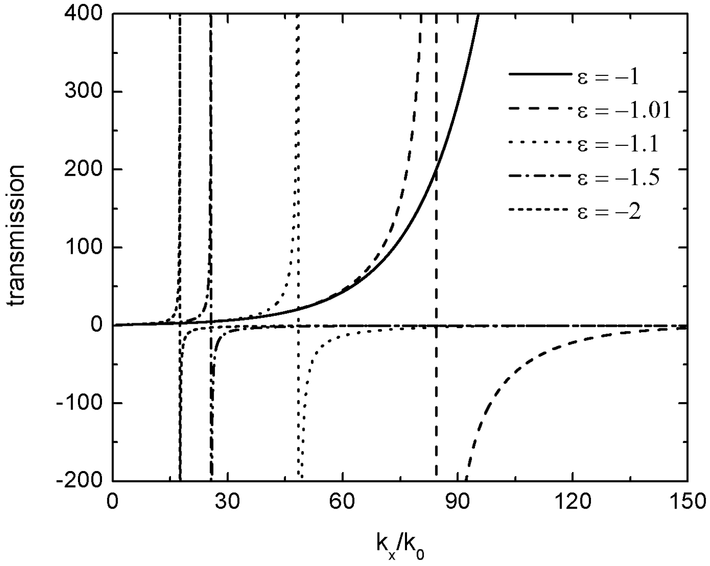

Figure 2.8: The transmission coefficient as a function of normalized parallel **k** component. The layer thickness is $\lambda/100$. Compared to Fig. 2.7, where the thickness is smaller, the amplification is increased and the singularities are shifted towards lower k_x values.

Eq. (4.2) shows that in order to have a singularity, a negative permeability is not essential for a TM wave. A TM wave incident on an SNG layer with a negative permittivity can experience the singularity. Therefore SNG layers can amplify the evanescent fields. The difference between an unmatched DNG layer and an SNG layer is that the unmatched DNG layers can amplify both TE and TM waves. On the other hand, SNG layers with a negative permittivity can only amplify the TM waves and SNG layers with a negative permeability can only amplify the TE waves. Fig. 2.9 shows the transmission through a $\lambda/50$ thick layer. An SNG layer with $\epsilon = -1$ follows a very similar amplification characteristics as a matched DNG layer up to a k_x value of $65k_0$. Similar to the unmatched DNG layer case, as the permittivity deviates from -1, the singularity location shifts to lower k_x values, and the amplified evanescent spectrum gets smaller.

2.4.2 Effect of Matched DNG Lens without Loss

In the first configuration to be analyzed, the target medium will be considered as vacuum. The angular wavenumber of the material with the largest $\epsilon\mu$ product is defined as k_{max}. In order for the field to have evanescent behavior in all regions, the incident wave must have $k_x > k_{max}$. Without loss of generality, a nonmagnetic target with a thickness of

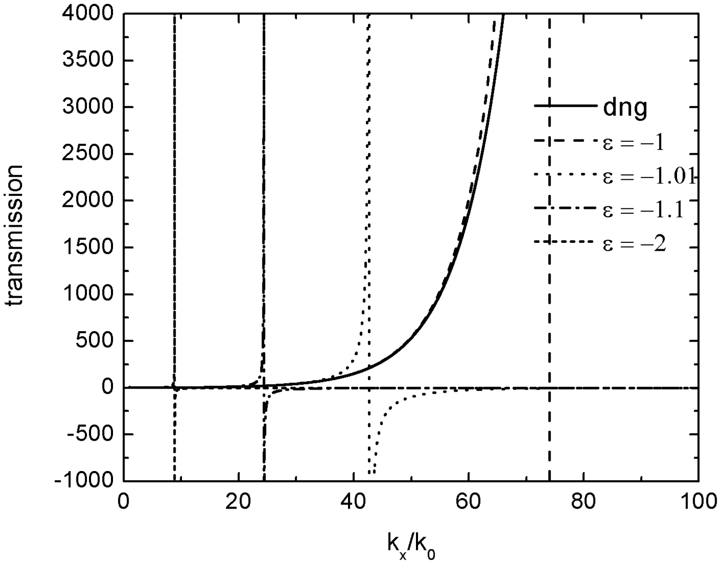

Figure 2.9: The transmission coefficient through a matched DNG layer and different SNG layers as a function of normalized parallel **k** component. The layer thickness is $\lambda/50$.

$t = \lambda_0/75$, where λ_0 is the wavelength in free space, and a relative permittivity of 6 is considered. The input is an evanescent plane wave with a $k_x = 1.5k_{max}$.

The DNG lens is matched to the free space with relative permittivity and permeability equal to -1 since this amplifies the whole evanescent spectrum with a well defined exponential function. The lens is assumed to be lossless. (There is no reflection at the boundary between a DNG lens and a positive medium if they are matched.)

Fig. 2.10 shows the sensitivity for different DNG thicknesses. The sensitivity is plotted as a function of the lens-to-target distance, which is represented in terms of t. Throughout this section, the lens-to-target distance is defined as the distance $|Z_3 - Z_5|$ (see Fig. 2.6). Clearly seen is that the thicker the DNG lens, the higher the sensitivity; however, what is interesting is that there is a minimum DNG thickness required to achieve a sensitivity improvement. For example, as can be seen from Fig. 2.10, a DNG lens with a thickness of t does not improve the sensitivity. In fact, it turns out that a DNG thickness greater than $1.4t$ is needed for this particular configuration (target thickness of $t = \lambda_0/75$ and ϵ_r=6).

The reason for the minimum DNG thickness requirement can be explained as follows. When a target interacts with the evanescent field, there are two mechanisms that affect the **E** and **H** field energies. The first mechanism is due to the permittivity and permeability

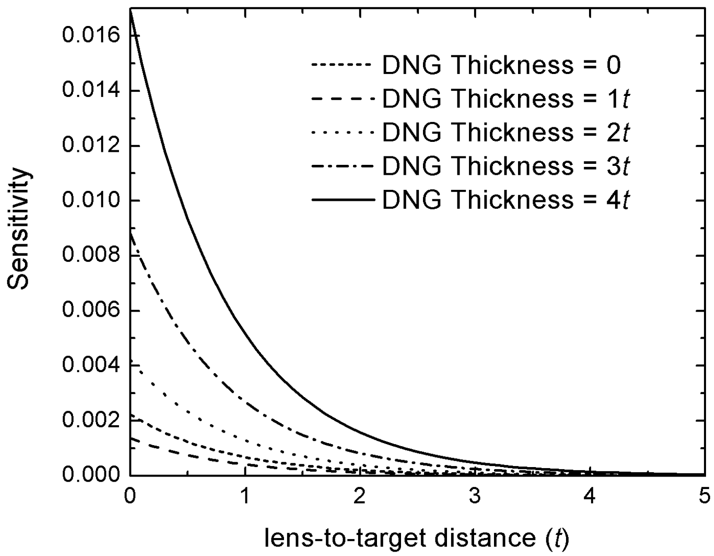

Figure 2.10: Sensitivity as a function of lens-to-target distance, for DNG thicknesses of t, $2t$, $3t$ and $4t$ ($t = \lambda_0/75$). As the DNG thickness is increased, the sensitivity increases. The nonmagnetic target is t thick with ϵ_r of 6.

changes of the probe medium as a consequence of the presence of the target. For an evanescent TE wave in a dielectric medium, the difference of the **E** and **H** field energy densities is calculated as

$$u_h - u_e = \frac{|k_z|^2}{\omega^2 \mu}|E|^2 \tag{2.52}$$

As the permittivity is increased, $|k_z|$ is reduced to maintain a constant k_x. From Eq. (2.52), the reduction in $|k_z|$ leads to a reduction in the energy difference when there is a target with a higher permittivity compared to the surrounding medium. As a consequence, the second term in the sensitivity definition (Eq. (2.27)) deviates further from unity. (Similar conclusion applies when the target has a permittivity lower than the target medium.)

The second mechanism is the energy change due to the reflection from the target. This mechanism increases the energy difference since it produces a reflected field with $|u_h - u_e|$ greater than zero. When there is no DNG layer, the reflected field energies are small since the field is decaying and the dominant mechanism is the first mechanism. On the other hand when there is a thick enough DNG layer, the reflected field is amplified and the second mechanism becomes more dominant. This behavior is presented in Fig. 2.11 where $\frac{(U_m - U_e)_{with\ target}}{(U_m - U_e)_{without\ target}}$ ratio is plotted as a function of the lens-to-target distance.

Next, the sensitivity behavior as a function of k_x is considered. The sensitivity be-

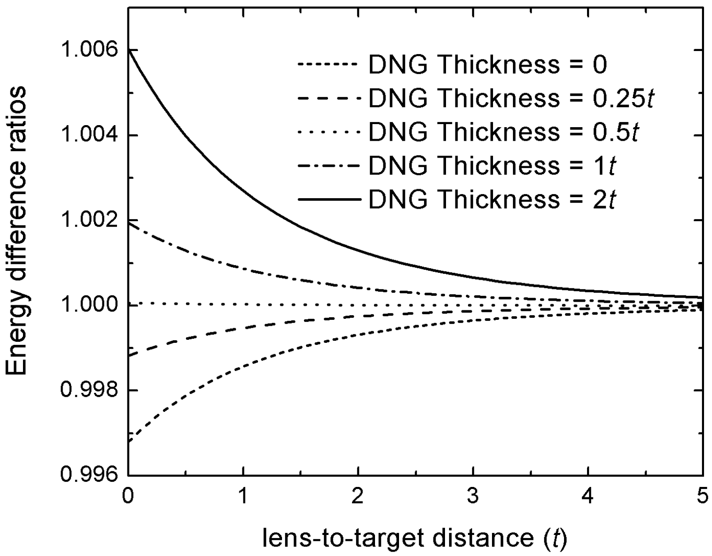

Figure 2.11: The **H** field and **E** field energy differences normalized by the difference without any target, $\frac{(U_m - U_e)_{with\ target}}{(U_m - U_e)_{without\ target}}$, plotted as a function of the lens-to-target distance t. When there is no DNG layer the target reduces the difference. On the other hand when there is a DNG layer the target increases the difference.

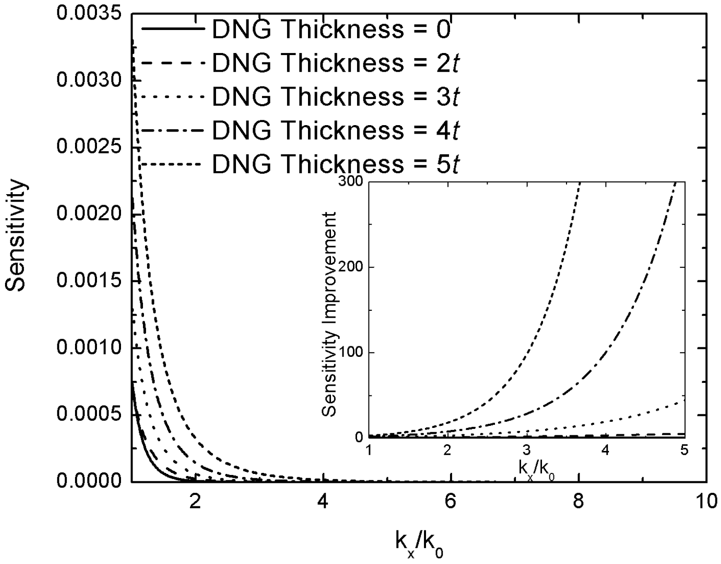

Figure 2.12: The sensitivity as a function of normalized k_x. The inset shows that sensitivities of the fields with higher k_x values experience better enhancements. Sensitivity improvement achieved by a DNG lens is defined as the sensitivity normalized by the sensitivity of the corresponding case without the DNG lens. The lens-to-target distance is $3t$ for all cases.

havior is presented in Fig. 2.12 for different matched DNG layer thicknesses. A t thick DNG does not improve the sensitivity as presented in Fig. 2.10, therefore excluded from the graph. As the parallel **k** component is increased, the sensitivity decreases. The inset shows the *sensitivity improvement* defined as sensitivity with DNG normalized by the sensitivity without the DNG. While the high k_x components have lower sensitivity, they have a better sensitivity improvement. Therefore the sensitivity is improved for all k_x values greater than unity, thus implying that the sensitivity improvement is valid for the entire evanescent spectrum. As a consequence, these results conclude that the sensitivity improvement is valid for any type of near-field probes.

Fig. 2.13 shows the sensitivity behavior for thick DNG layers. Note that the expression *thick* depends on the reflection coefficient from the target and the target distance ($Z_3 - Z_2$). For thick DNG layers, higher k_x components have higher sensitivities. This is because the field is mostly amplifying rather than decaying in the region where field energies are highly effective on the sensitivity.

For a subsurface detection scheme, a more realistic model would have a target medium other than vacuum. Here, the relative permittivity of the target medium and the target

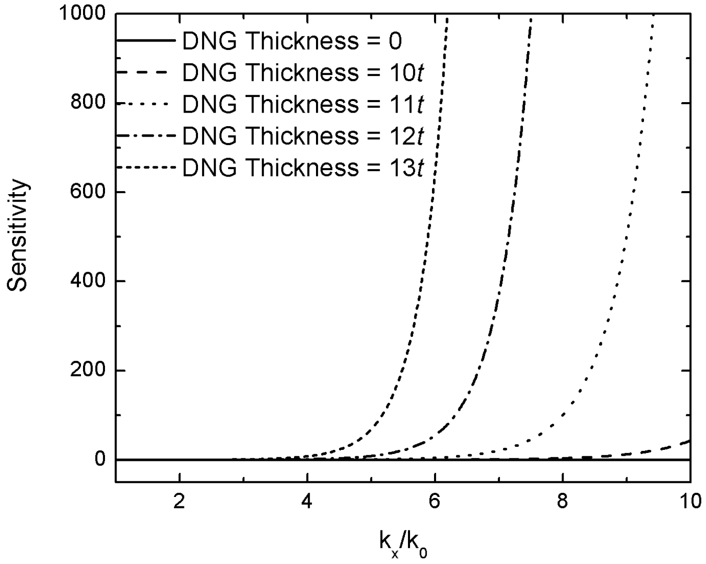

Figure 2.13: The sensitivity behavior for thick DNG layers. As k_x increases the sensitivity increases.

are set to 2 and 6, respectively. The incident field is kept as before. The tip to lens and lens to target medium distances are kept at zero. All media, except the lens, are assumed to be nonmagnetic.

In Fig. 2.14, the sensitivity versus the lens-to-target distance is plotted for different lens thicknesses, while keeping the thickness of the target constant at t. It is observed that, in a manner similar to the target in vacuum case, increasing the DNG thickness increases the sensitivity and a minimum DNG thickness is required to enhance the sensitivity. In addition, the sensitivity is seen to be higher than the case when the target medium was vacuum, since when the permittivity of the target medium is increased, the decay constant is reduced. Further analysis (the graphs are not presented here for brevity) shows that although increasing the permittivity of the target medium increases the sensitivity, as the target medium permittivity approaches the permittivity of the target, the sensitivity is reduced. This is because even though the field penetrates better, it does not experience any significant change when encountering the target.

An important behavior different than the case when the target medium is vacuum is the saturation of the sensitivity improvement as the DNG lens thickness increases. For the configuration considered here, the sensitivity improvement is saturated when the thickness of the DNG lens reaches $20t$, despite the lossless nature of the lens.

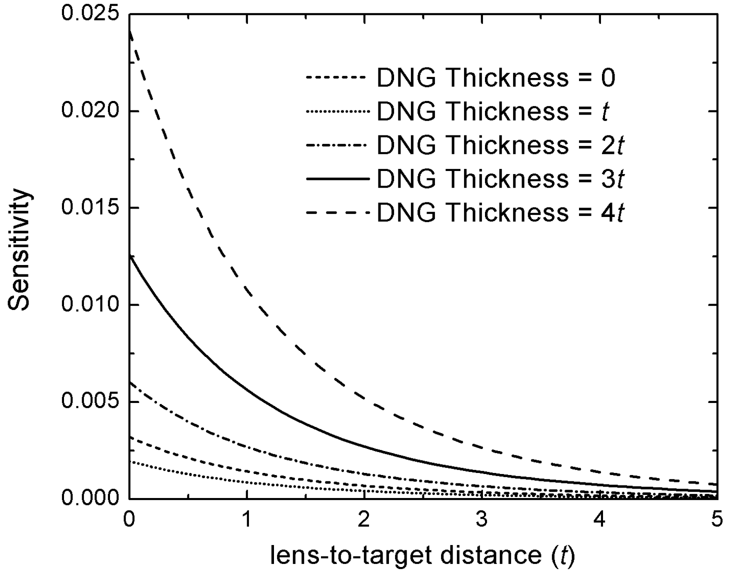

Figure 2.14: Sensitivity versus target depth for a buried target. The target medium has a relative permittivity of 2 and the target has a permittivity of 6 with a thickness of t. The sensitivity is plotted for 5 different lens thicknesses.

Similar to the previous case (target medium as vacuum), the lens enhances the sensitivity for any incident evanescent field. Fields with higher k_x has a higher enhancement potential when using a DNG lens, and increasing the target thickness or target to target medium mismatch increases the sensitivity.

2.4.3 Effect of DNG Lens with Loss

In practical applications, DNG materials are lossy. In the case of a lossy DNG lens, the sensitivity improvement is expected to be reduced and the loss will form an upper bound on the sensitivity enhancement whether the target medium is vacuum or not. The loss effect is expected to be more dominant for high k_x values. Since the amplification in the DNG lens is limited by the loss of the lens, and higher k_x components need more amplification, these components suffer from loss.

Fig. 2.15 shows the sensitivity in the case of a lossy DNG lens. The DNG lens parameters are $\omega_p = \omega\sqrt{2.02}$ and $\Gamma_e = 0.1\omega$, corresponding to a complex relative permittivity equal to -1+j0.2. It is observed that the sensitivity improvement is reduced compared to the case of a lossless DNG. In addition, there is an optimum DNG thickness needed to achieve maximum sensitivity. For instance, for the target and medium parameters con-

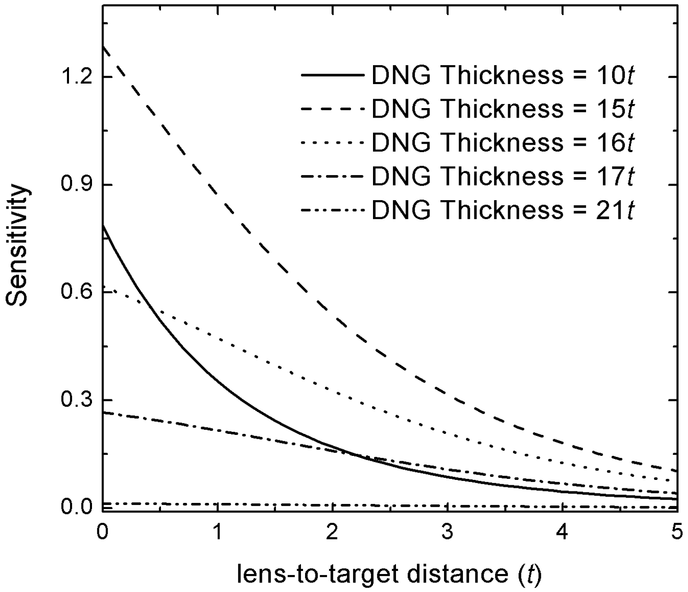

Figure 2.15: The sensitivity behavior for lossy DNG case. Sensitivity is plotted as a function of lens-to-target distance for DNG thicknesses of $10t$, $15t$, $16t$, $17t$, and $21t$. The target medium and the target has a relative permittivity of 2 and 6, respectively, and the target thickness is t. The DNG lens has an imaginary part of complex permittivity (loss tangent) equal to 0.2.

sidered here, the optimum thickness is around $15t$. As the thickness is increased further, the sensitivity is degraded to lower levels, even lower than the case without the DNG lens, a consequence that is expected since a relatively thick DNG lens with loss shields the target from the source.

2.4.4 Effect of Target Medium with Loss

In this part, the effect of having a lossy target medium is investigated. Since in most cases, such as biomedical applications and land mine detection, the target is buried in a lossy medium, the effect of $\tan\delta$ of the target medium is an important parameter.

Fig. 2.16 shows the effect of increasing $\tan\delta$ of the target medium. The permittivity of the target medium has a real part equal to 2. Other than the $\tan\delta$ values, the rest of the parameters are equal to the case presented in Fig. 2.14. As $\tan\delta$ increases the sensitivity reduces as expected. Using a DNG layer increases the sensitivity both in the case of lossless target medium and in the case of lossy target medium.

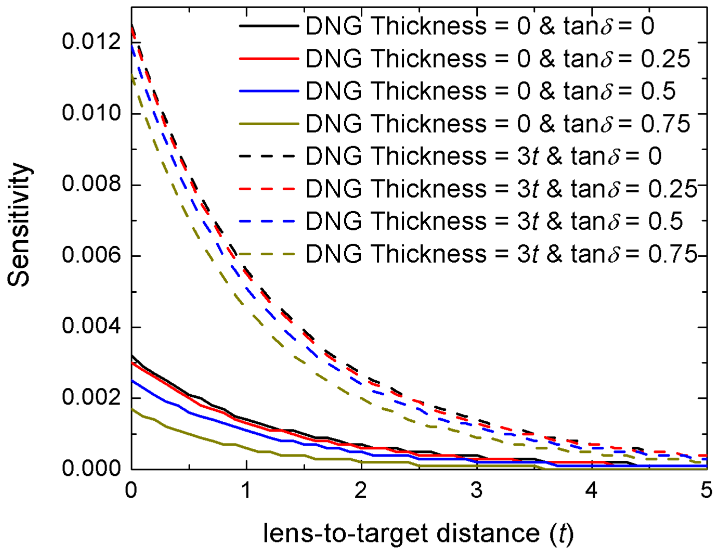

Figure 2.16: The sensitivity behavior for lossy target medium case. Sensitivity is plotted as a function of lens-to-target distance for different target medium $\tan\delta$ values. The DNG layer is lossless and the rest of the parameters are equal to the case presented in Fig. 2.14.

2.4.5 Effect of SNG and Unmatched DNG Metamaterials

As matched DNG metamaterials, SNG metamaterials and unmatched DNG metamaterials also amplify evanescent fields as discussed in Section 2.4.1. There are additional fundamental limitations for the use of SNG metamaterials as compared to DNG metamaterials since amplification characteristics of an SNG lens is different then a DNG matched lens.

Knowing that the transmission behaviors of unmatched DNG and SNG layers have the same characteristics, only the sensitivity behavior for SNG layers is presented. The difference between SNG and unmatched DNG layers is that SNG can improve only TE or only TM waves while the DNG can support sensitivity improvement for both waves.

In Fig 2.17, the sensitivity as a function of lens-to-target distance is plotted for different SNG lens thicknesses. The incident field is a TE wave with $k_x = 1.5k_{max}$. The SNG material has $\epsilon_r = 1$ and $\mu_r = -1$. The target medium and the target has a relative permittivity of 2 and 6, respectively, and the target thickness is t. For this configuration, the singularity is observed with an SNG lens of $9.22t$ thickness and a lens-to-target distance of $1.5t$, as shown in the inset of Fig. 2.17. When the SNG lens is thinner than the

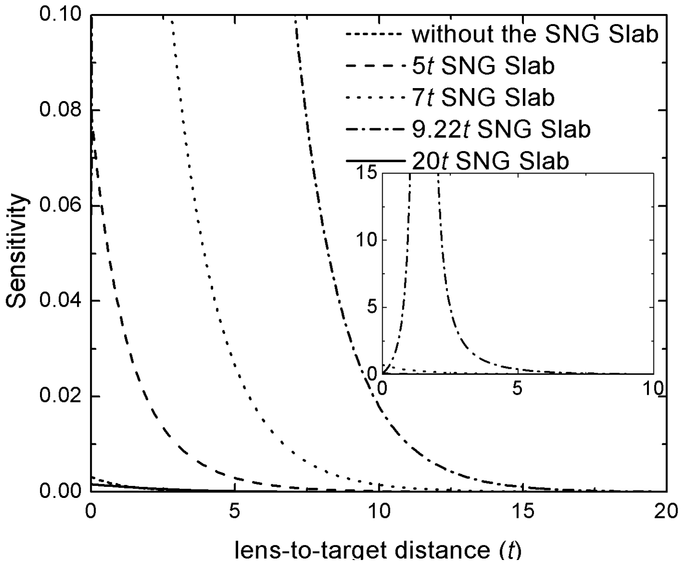

Figure 2.17: Sensitivity versus target distance for a target medium and target having relative permittivity of 2 and 6, respectively, and a target thickness of t. $5t$ The SNG lens results a sensitivity improvement similar to the DNG slabs. $9.22t$ slab has a singularity when the target is at $1.5t$. $20t$ slab reduces the sensitivity.

singularity condition, the sensitivity improvement is similar to the DNG lens case. If the lens is thicker, the sensitivity improvement is reduced and increasing the thickness further eventually results in no sensitivity improvement in comparison to the case without the SNG lens.

The SNG metamaterials have advantage over the DNG metamaterials due to fabrication considerations. The DNG metamaterials are produced by using periodic split ring resonators, for negative permeability, and periodic conductive rods, for negative permittivity, simultaneously in a dielectric matrix [26]. The SNG metamaterials, however, need only either split ring resonators [25] or conductive rods [24] which reduces the fabrication complexity and the metallic content of the overall material. The drawbacks of the SNG metamaterials are the limitations over the evanescent spectrum, slab thickness and its selectivity vis-a-vis TE and TM waves. On the other hand, the SNG metamaterial, due to the transmission singularity, has the potential for strong substantial improvement in the sensitivity.

2.5 Numerical Results

In this section, numerical experiments are presented where different configurations are considered in order to validate the theoretical findings of sensitivity enhancement discussed above. The simulations are conducted using finite difference time domain (FDTD) and finite element (FEM) methods.

2.5.1 Finite Difference Time Domain Simulations

An FDTD code is developed that simulates a parallel plate waveguide with perfectly conducting plates. The Yee Algorithm as described in Ref. [82] is used for the implementation. The field inside the waveguide is generated by using the current

$$\mathbf{J}(x,y,t) = \hat{z}\sin(\frac{n\pi}{W}y)\delta(x)\sin(2\pi f t) \tag{2.53}$$

as given in Ref. [83], where W is the width of the waveguide, f is the operating frequency. The current excites a $\mathrm{TE_{0n}}$ mode in the waveguide. The field decays in $\hat{x}$ direction (or propagates in $\hat{x}$ direction if it is not evanescent) and the E field is in the $\hat{z}$ direction. This structure is preferred since it provides a simple and well-defined evanescent wave generation. The resulting field is a superposition of two plane waves. These waves have same reflection and transmission coefficients at the target and DNG boundaries.

The resulted field has E_z, H_x, and H_y components. For DNG regions, the Drude model is used. The differential equations to be solved for the Drude Model are given as [62] [79]

$$\frac{\partial}{\partial t}E_z(t) = \frac{1}{\epsilon_0}(\frac{\partial}{\partial x}H_y(t) - \frac{\partial}{\partial y}H_x(t) - J_{z,Drude}(t)) \tag{2.54}$$

$$\frac{\partial}{\partial t}H_x(t) = -\frac{1}{\mu_0}(\frac{\partial}{\partial y}E_z(t) + K_{x,Drude}(t)) \tag{2.55}$$

$$\frac{\partial}{\partial t}H_y(t) = \frac{1}{\mu_0}(\frac{\partial}{\partial x}E_z(t) - K_{y,Drude}(t)) \tag{2.56}$$

$$\frac{\partial}{\partial t}J(t)_{i,Drude} + \Gamma_e J(t)_{i,Drude} = \epsilon_0\omega_p^2 E_i(t) \tag{2.57}$$

$$\frac{\partial}{\partial t}K(t)_{i,Drude} + \Gamma_m K(t)_{i,Drude} = \mu_0\omega_p^2 H_i(t) \tag{2.58}$$

where $K_{i,Drude}$ is the magnetic current in the i direction, $J_{i,Drude}$ is the electric current in the i direction and ω_p is the resonance frequency of the Drude medium. For the other regions, the field equations are basically same as Eqs. (2.54), (2.55) and (2.56) with the magnetic and electric current terms are equal to zero. Note that, there is no restriction over the sign selection of the $\mathbf{k}$, which means that the behavior of the DNG medium

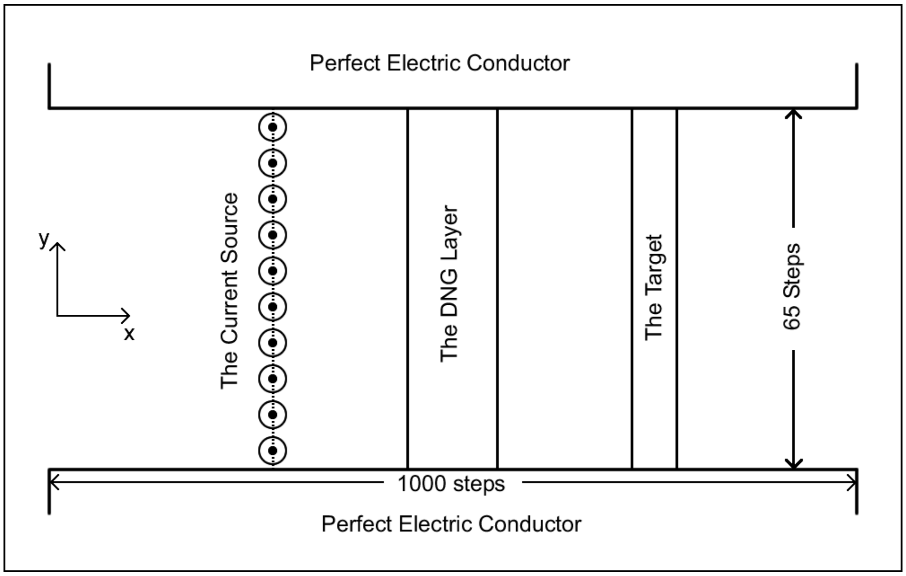

Figure 2.18: The simulated structure using FDTD. The waveguide represents the free space with target slab and DNG lens.

is not forced externally but it is a natural result of the governing differential equations. Therefore the simulation is also an important way for verifying the wave physics in the DNG materials.

Eqs. 2.53-2.58 are discretized for the simulation geometry shown in Fig. 2.18. A grid of 1000 by 65 with 0.5 mm intervals has been used for the simulation. The operation frequency is $f = 400$ MHz and the resonance frequency of the Drude medium is $\omega_p = 3.52 \times 10^9$ rad/s. The excitation is at the 333^{th} grid and n in Eq. 2.53 is assumed to be one. The DNG slab starts at the 335^{th} grid. The courant number is $c\Delta t/\Delta z = 0.6$. The simulator was run for 35000 time steps and then the current source was stabilized and the E field peaks at every point were taken in 5000 time steps. Using these peak values, the sensitivity is plotted as a function of target distance for different DNG thicknesses in Fig. 2.19. The FDTD results are in agreement with the theoretical results. Increasing DNG thickness increases the sensitivity.

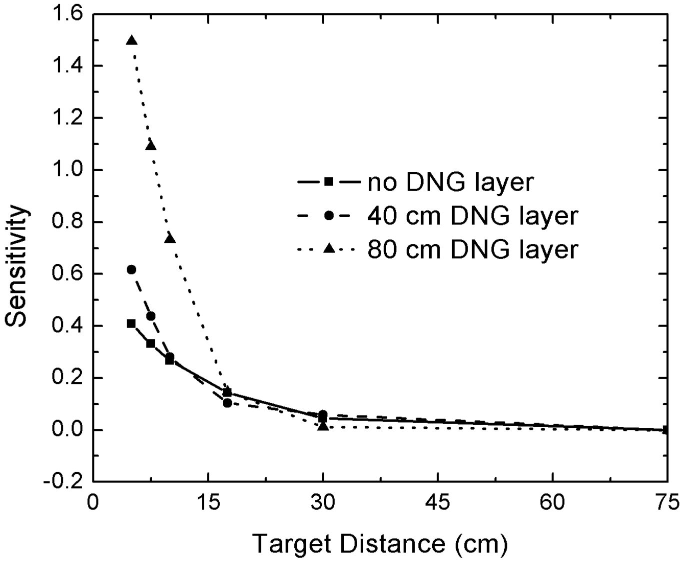

Figure 2.19: FDTD results for sensitivity versus target distance at DNG thicknesses of 0cm, 40cm and 80cm. The target is a dielectric slab with an $\epsilon_r = 1.2$ and a thickness of 25cm inside a parallel plate waveguide. The field inside the waveguide has an attenuation constant of 0.034874cm^{-1}

2.5.2 Finite Element Simulations

Finite element method (FEM) simulations are performed using HFSS, a three-dimensional finite element analysis tool by Ansoft corporation.

In the first numerical experiment, the field change due to the presence of a DNG lens is analyzed. A cutoff waveguide with rectangular cross section of dimensions $\lambda_0/5 \times \lambda_0/5$ is considered. The field is excited from the left end of the waveguide as shown in Fig. 2.20. The **E** field distributions, with and without the DNG layer, are plotted along the waveguide for two different target locations. The generated field has a decay constant of $2.29k_0$. The amplifying region is a DNG lens matched to the free space with a loss tangent of -0.45.

Fig. 2.20-(a) shows the **E** field distribution without any DNG layers. The target hardly changes the field distribution. The **E** field distribution with a DNG layer is shown in Fig. 2.20-(b) where the field change in the DNG layer due to the target is visible. Therefore, it can be observed that the main role of the DNG lens is to enlarge the active region in which the field distribution is changed by the target. When there is no DNG lens, the target changes the fields only in the proximity of itself. On the other hand, as a result of the evanescent field amplification, when there is a DNG lens, the target also changes the field distribution in the lens itself.

Next, the sensitivity behavior in a cutoff waveguide is investigated. A waveguide with a cross section of $\lambda_0/5 \times \lambda_0/5$ which generates an evanescent field with a parallel **k** component, k_x, equal to $2.5k_0$ is used. The sensitivity of a copper target with a thickness of $\lambda_0/25$ is studied in the case of different DNG lens thicknesses (Fig. 2.21). The simulations are performed at 300 MHz. The material properties of the lens are $\epsilon = -1 + j0.1$ and $\mu = -1 + j0.1$. The optimum DNG thickness is $0.11\lambda_0$. Increasing the thickness of the DNG layer reduces the sensitivity if the thickness is larger than the optimum thickness.

In order to analyze other evanescent field components, the sensitivity behavior is studied for waveguides with different cross sections. Figs. 2.22 and 2.23 present the sensitivity behaviors when the cross section is $\lambda_0/4 \times \lambda_0/4$ ($k_x = 2k_0$) and $\lambda_0/10 \times \lambda_0/10$ ($k_x = 5k_0$), respectively. Fig. 2.24 shows the sensitivity for a target at $0.01\lambda_0$ as a function of DNG layer thickness for different evanescent fields. When the parallel **k** component increases, the optimum DNG layer thickness reduces. As discussed in the Section 2.4.3, when the DNG layer is lossy, fields with higher k_x components suffer more.

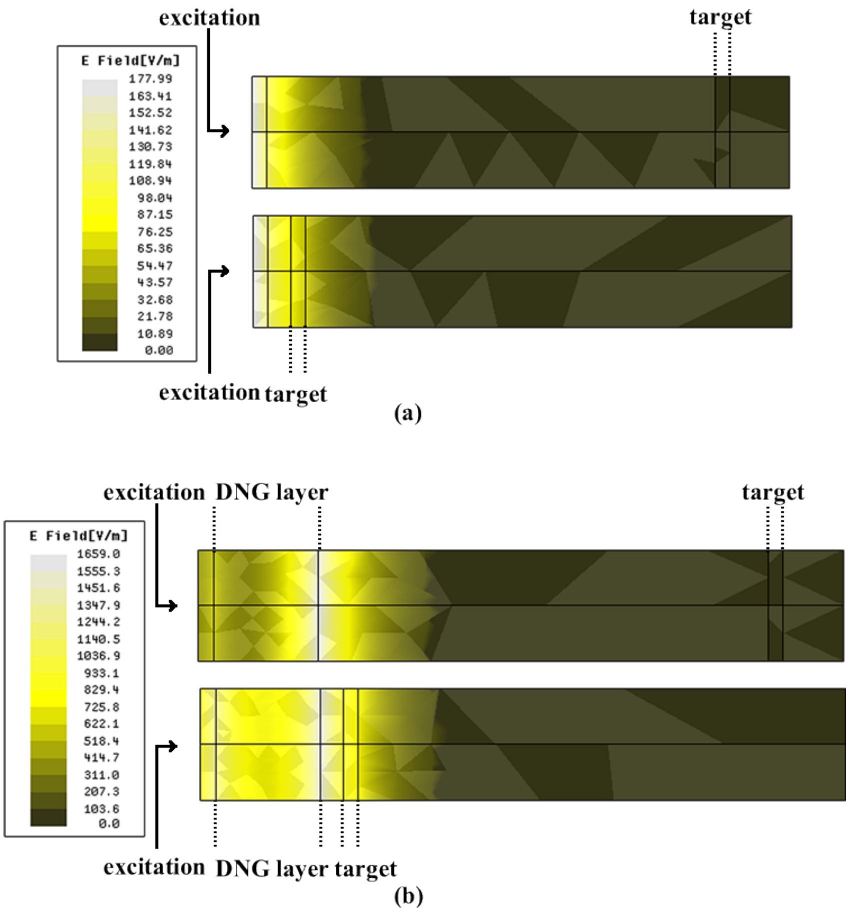

Figure 2.20: The effect of target on the **E** field distribution without (a) and with (b) a DNG layer. The upper panels show the field distributions when the lens-to-target distance is $4\lambda_0/5$. The lower panels show the field distributions when the lens-to-target distance is $\lambda_0/25$. The rectangular waveguide has a side length of $\lambda_0/5$. The target thickness is $\lambda_0/37.5$ and the lens thickness is $\lambda_0/5$.

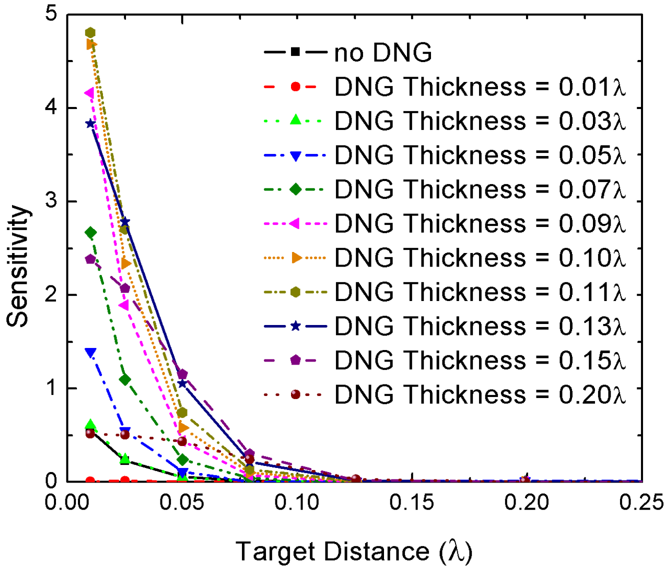

Figure 2.21: Sensitivity improvement for a conductive target as a function of target distance. The parallel **k** component, k_x, is equal to $2.5k_0$. The maximum sensitivity is achieved with a 0.11λ DNG lens thickness

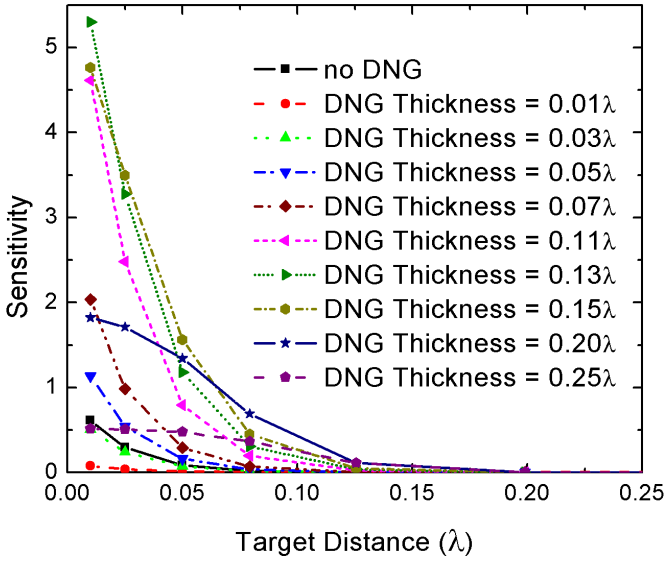

Figure 2.22: Sensitivity improvement for a conductive target as a function of target distance. The parallel **k** component, k_x, is equal to $2k_0$. The maximum sensitivity is achieved with a 0.13λ DNG lens thickness

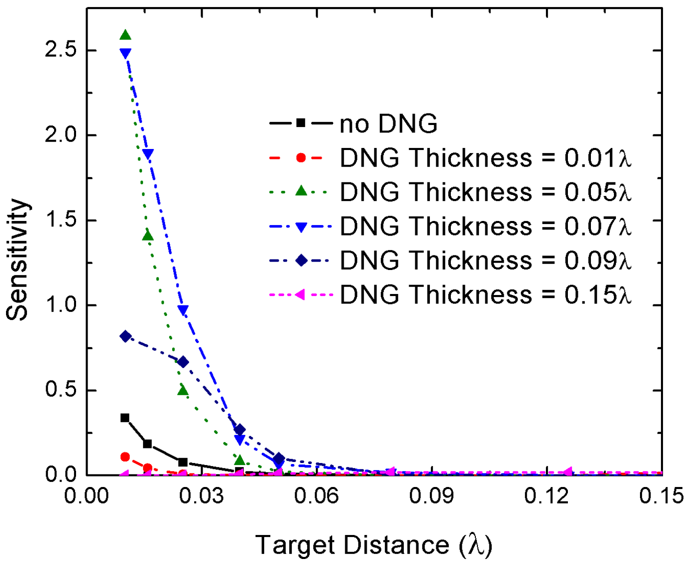

Figure 2.23: Sensitivity improvement for a conductive target as a function of target distance. The parallel **k** component, k_x, is equal to $5k_0$. The maximum sensitivity is achieved with a 0.05λ DNG lens thickness

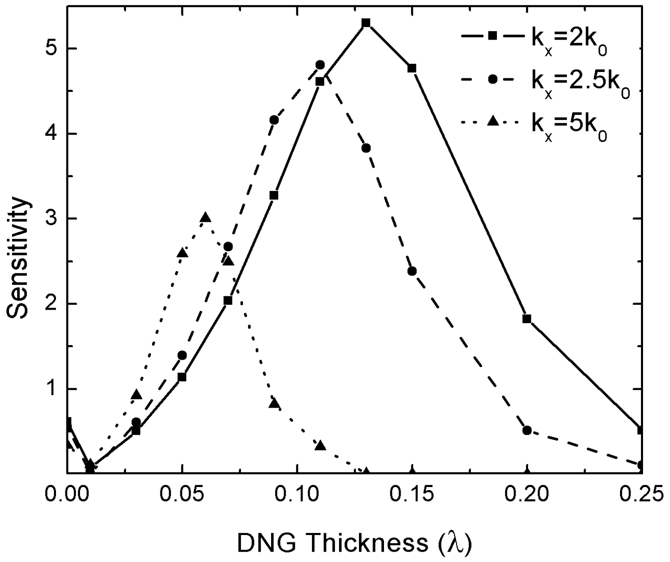

Figure 2.24: The sensitivity improvement as a function of DNG thickness for a target placed 0.01λ away from the DNG layer. Three incident fields with different parallel **k** components are used. As k_x is increased, the optimum DNG layer thickness is reduced.

2.6 Waveguide Resonators

A conventional evanescent field probe produces all polarizations of the E and H fields. Therefore the experimental verification of the theory is not easy since a low loss, three dimensional DNG metamaterial is required. In this section a structure (Fig. 2.25) that can be used for verification of the sensitivity enhancement using a two dimensional DNG metamaterial is studied. Theoretical results and numerical validation using the finite element method are presented [84].

2.6.1 Theory

An evanescent field detector is composed of a resonator and an electrically small probe that generates evanescent fields. The impedance of the probe is a function of the emanated field from the probe which depends on the electrical properties of the medium [77]. A variation in the electrical properties of the medium shifts the impedance, and this shift affects the resonance frequency of the resonator. Fig. 2.25 shows the model structure capable of representing the resonator and the evanescent field generation. The structure is a rectangular waveguide, partially filled with a high dielectric constant material. The field is propagating in the resonator region and it is evanescent in the other regions. When the TE_{10} mode is used, the E-field only has $\hat{x}$ component and the H-field has $\hat{y}$ and $\hat{z}$ components. Therefore the combination of a 2D negative μ material and a 1D negative ϵ material behaves as a negative refractive index material for the TE_{10} mode.

When the time dependence is assumed to be e^{jwt}, the resonance condition of a transmission line resonator as shown in Fig. 2.25 is

$$\Gamma_1 \Gamma_2 e^{-2j\beta l} = 1 \tag{2.59}$$

if Z_1 and Z_2 are purely imaginary. Since one side of the resonator is terminated by a metallic wall, Γ_2 is equal to -1 for the structure. When there is a target, the target changes Γ_1. Therefore for a higher sensitivity, the effect of the reflection due to the target on Γ_1 must be higher.

Assume that the field has a propagation constant β_r in the resonator and β in vacuum as shown in Fig. 2.26. Since the field is propagating in the resonator and evanescent in the vacuum region, β_r is purely real and β is purely imaginary. Evanescent fields decay in double positive materials, therefore β can be expressed as $\beta = -jk$ where k is a real positive number, $k = \sqrt{(\pi/d)^2 - \omega^2 \epsilon_0 \mu_0}$. In Fig. 2.26, a represents the thickness of the DNG layer and b represents the target distance. If the target has a reflection coefficient

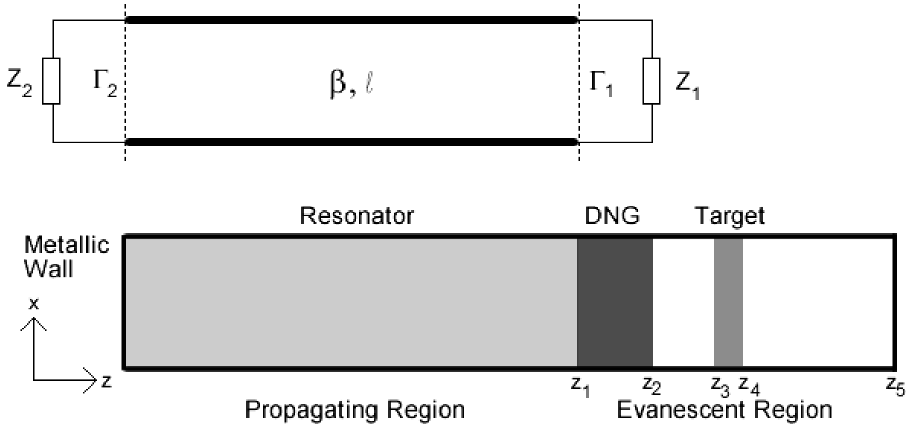

Figure 2.25: The evanescent field detector model for examining the effect of using DNG material. The dimensions of the waveguide forces the field to be propagating in the resonator region and to be evanescent in the other regions.

of Γ_t, the overall reflection coefficient, Γ becomes

$$\Gamma = r + \frac{t' t \Gamma_t e^{2j\beta(a-b)}}{1 - r' \Gamma_t e^{2j\beta(a-b)}} \tag{2.60}$$

where

$$t = \frac{2\beta_r}{\beta_r + \beta}, r = \frac{\beta_r - \beta}{\beta_r + \beta} \tag{2.61}$$

$$t' = \frac{2\beta}{\beta_r + \beta}, r' = \frac{\beta - \beta_r}{\beta_r + \beta}. \tag{2.62}$$

For the derivation of these equations, a similar method presented in Ref. [5] is used. Series of multiple reflections between z_1 and z_3 in Fig. 2.25 are added to achieve the total reflection coefficient. Note that the DNG region is assumed to be matched to free space which results no reflection from the boundary at z_2. t and r are the transmission and reflection coefficients for a wave passing from a medium with ϵ_r and μ_r to ϵ and μ. t' and r' are the transmission and reflection coefficients for a wave passing from a medium with ϵ and μ to ϵ_r and μ_r.

From Eq. (2.59), as the target distance, b, increases, the exponential term becomes smaller and Γ converges to r, making the resonance frequency independent of Γ_t, the target. The effect of increasing the DNG thickness, a, is the reverse of the effect of increasing b. As a result, using a DNG layer compensate the effect of increasing the target distance, hence the sensitivity and the range is increased.

The reflection coefficient for the structure shown in Fig. 2.25 is calculated using boundary conditions. Using a waveguide with $d = 10$ cm, and a target with $\epsilon_t = 6$, $\mu_t = 1$ and

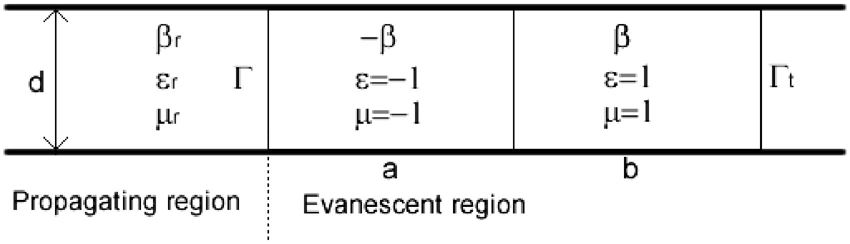

Figure 2.26: In order to sense a target with a reflection coefficient of Γ_t, variations in Γ_t should change Γ.

a target thickness of 1 cm, the resonance frequency is calculated as a function of target distance for different DNG thicknesses. The resonator region has a relative permittivity of 9, which results a cutoff frequency of 500 MHz, for the TE_{10} mode. The resonator length is 20 cm. For the vacuum region and for the target the cutoff frequencies are 1500 MHz and 612.37 MHz, respectively.

Fig. 2.27 shows the frequency shift as a function of the target distance. The percentage frequency shift is calculated using $100 \times (f - f_0)/f_0$ where f_0 is the resonance frequency without the target. Increasing the DNG thickness results a higher frequency shift for the same target distance. A 4 cm DNG slab increases the frequency shift by 12.7 times for a target distance equal to 0. Note that for all data points, the resonance frequencies are between 510 MHz and 600 MHz. Therefore the condition of having propagating field in the resonator and evanescent field in the other regions is satisfied.

2.6.2 Numerical Verification

The full-wave simulation tool HFSS is used to verify the enhancement in the sensitivity. Eigenmode solution is used to calculate the resonance frequency and the mode of the resonance is verified by visually inspecting the field distribution. The DNG material has ϵ and μ equal to -1 and $\sigma = 0.001$ S/m. Fig. 2.28 shows the frequency shift improvement obtained by using DNG slabs. Using 4 cm DNG slab enhanced the frequency shift by 12.4 times.

2.7 Conclusion

In previous works, DNG and SNG media were found to amplify evanescent fields. The purpose of this work is to answer the question whether these media can be used to enhance the effectiveness of near-field probes which work by detecting the change in the energy

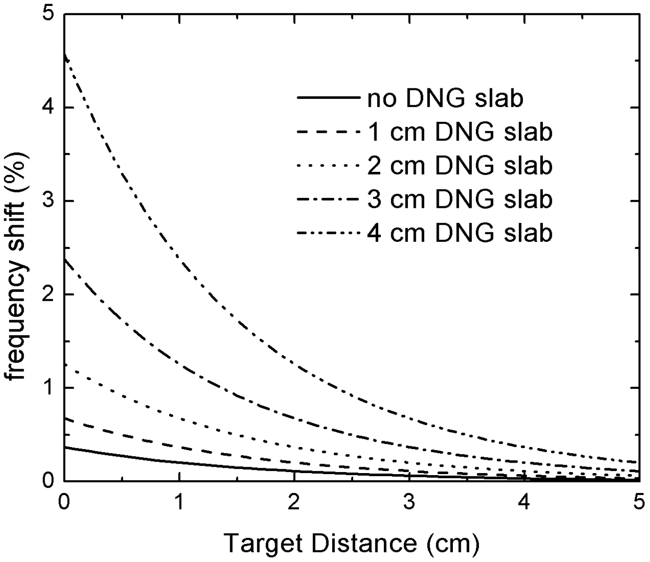

Figure 2.27: Theoretical results show the improvement in the sensitivity with the use of a DNG layer. As the DNG thickness increases the frequency shift increases

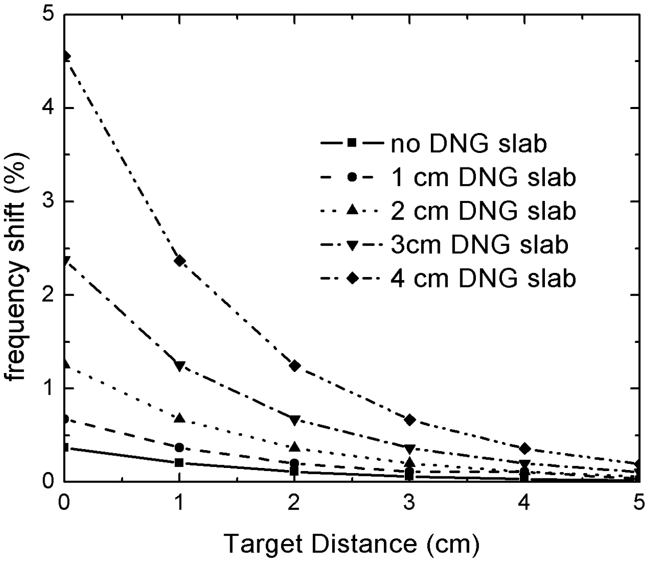

Figure 2.28: The frequency shift as a function of target distance, generated by HFSS.

stored in the close proximity of the probe. In this chapter, for the first time a sensitivity definition was presented which can be used to study the effectiveness of DNG and SNG lenses in enhancing the sensitivity of near-field probes. A novel model using multi layers for the probe-target interaction was introduced which allowed for the excitation of a single evanescent plane wave.

It was found that by using DNG lenses, the sensitivity for buried and non-buried objects can be increased; however, the increase in sensitivity is not a monotonic function of the DNG lens thickness. In fact, it was found that the DNG thickness needed for increased sensitivity has a lower and upper bounds, irrespective of losses in the lens itself.

The effectiveness of SNG lenses was also discussed. The advantage of SNG media is its relatively easier fabrication in comparison to DNG media and the potential for substantial increase in the sensitivity. The tradeoff is additional constraints on the sensitivity improvement.

Finally, the theoretical findings presented in this work were validated using numerical experiments involving waveguide structures.

Chapter 3

Application to Open-ended Rectangular Waveguide Structures

3.1 Introduction

In this chapter, a numerical validation of the theoretical development reported in Chapter 2 [23, 85] is presented. By using numerical experiments, it is shown that when a layer of SNG medium is added to the opening of a rectangular waveguide, used as a near-field probe, a significant enhancement of the probe sensitivity is achieved while at the same time increasing the resolution. As a practical example, the study is focused on detecting precursor pitting in aluminium plates using a WR-28 Ka-band waveguide probe. However, the technique presented here can be applied to all types of probes that are based on near-field detection modalities.

3.2 Theoretical Background

A μ-negative SNG layer amplifies TE evanescent modes while an ϵ-negative SNG layer amplifies TM evanescent modes [5]. Without loss of generality, in this chapter, μ-negative media will be considered. In Chapter 2 [23, 85], using plane wave analysis, it was shown that when an SNG slab is placed between the source of evanescent energy and a target, the evanescent field amplification increases the *sensitivity* which is defined in terms of the reactive energy stored in the target medium. Furthermore, it was also shown that when using an SNG medium a singularity is observed in the transmission coefficient leading to a significant increase in the sensitivity at a specific SNG layer thickness. Assuming that the SNG medium is infinite in the x-y plane and having a uniform thickness of a in the z-direction, the singularity in the transmission occurs when the following condition is satisfied:

$$e^{-jk'_z a} = \frac{(k_z \mu' + k'_z \mu)^2}{(k_z \mu' - k'_z \mu)^2}, \tag{3.1}$$

where k_z and k'_z are the $\hat{z}$ components of the wave vectors outside and inside the SNG layer respectively. μ' and μ are the permeability of the SNG layer and the source region, respectively.

If the SNG layer is not lossless, a singularity in the transmission coefficient is no longer present but a transmission maximum is observed. As the loss tangent of the SNG medium is increased, the transmission maximum and the corresponding SNG medium thickness decrease.

3.3 Waveguide Structures with SNG Layers Placed Outside

The structure described in Ref. [11] is used here as the probe to analyze the improvement provided by the SNG layers. An open ended waveguide is used as the detector operating at a frequency of 30 GHz (Fig. 3.1). The target to be detected is a crack (0.1λ sided cube) on an aluminum plate which is identical to the target described in Ref. [11]. A schematic showing a side view of the position of the target (crack) in the aluminium plate is shown in Fig. 3.1. The waveguide probe is positioned as shown in Fig. 3.1 and is moved laterally in the x-y plane. An SNG layer is placed at the opening of the waveguide as shown in Fig. 3.1. As the waveguide probe is moved, the change in the phase of the reflected field is recorded and compared to a baseline value which is defined as that corresponding to the case without a crack. Since the crack is electrically small, it is not a strong scatterer [11]. As a result the change in the magnitude of the reflection coefficient is expected to be small and consequently the phase of the reflection coefficient is analyzed. The numerical modeling is performed using the finite-element based commercial software HFSS.

An open ended rectangular waveguide system is geometrically described by three parameters. The first one is the cross section of the waveguide. For this particular problem, a WR-28 type waveguide is used as the probe since it has been used for crack detection on aluminum plates [11]. The waveguide has a cross section of 7.11 mm × 3.56 mm and is operated at 30 GHz.

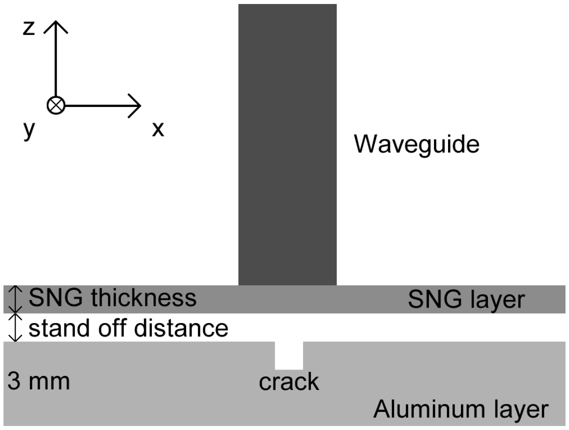

Figure 3.1: Schematic showing side view of the waveguide probe positioned on top of the aluminum plate having a crack. The SNG layer is positioned immediately at the opening of the waveguide.

The second parameter is the thickness of the SNG layer. Since the sensitivity improvement has a singularity, the SNG thickness has to be chosen such that the maximum amplification is achieved. The third parameter of the system is the standoff distance, which is defined as the distance between the end of the probe and the aluminum plate. Note that the SNG layer is assumed to be a part of the probe. In a conventional probe, without any SNG layer, as the stand off distance increases, the sensitivity decreases. As a result, as long as the standoff distance is small enough, it is not a very crucial parameter when there is no SNG layer. On the other hand, when an SNG layer is employed, the standoff distance plays an important role in the optimization process.

To eliminate errors in the phase that arise from numerical meshing, the phase shift is analyzed in the case of a *ghost target* which is defined with same geometry as the original one but filled with aluminum. The phase shift due to the ghost target is the meshing error. The resultant image is recorded as the *base image*. This base image is then subtracted from the image generated by the real target.

Since a μ-negative SNG layer is being used, the TE_{10} mode is excited in the waveguide. The relative permittivity of the SNG layers is 1.

3.3.1 Effect of SNG Layer Thickness

In this part, the standoff distance is kept constant and it is 1 mm (0.1λ). Therefore, other than the SNG layer, the structure is same as the case described in Ref. [11].

In order to compare the sensitivity of the probe with and without the SNG layer, the phase shift due to the target is analyzed. Taking the baseline case as the reference for the

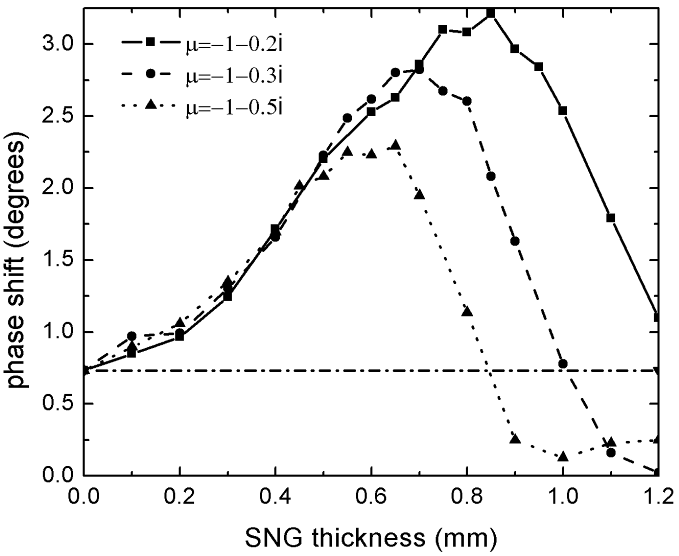

Figure 3.2: The phase shift as a function of the SNG layer thickness.

phase (no target), Fig. 3.2 gives the phase shift in the presence of the target as a function of the SNG layer thickness and for different cases of varying loss tangent. Fig. 3.2 shows that as the SNG thickness is increased, the phase shift increases. The data in Fig. 3.2 was obtained by centering the waveguide above the crack. The phase shift due to the target peaks at a specific SNG thickness as predicted by the theory. Furthermore, Fig. 3.2 shows that as the loss tangent is increased, the phase shift maximum occurs at smaller SNG layer thickness than the case with smaller loss tangent.

More specifically, for the crack size considered here, when there is no SNG layer, the phase shift is 0.7°. Using an 0.85 mm (0.085λ) SNG layer with a loss tangent of 0.2, the phase shift can be improved up to 3.2° .

Images

In order to visualize the sensitivity improvement and compare the image qualities, 2D images are generated by moving the probe along the $\hat{x}$ and $\hat{y}$ axes. At each probe position, the reflection phase is recorded and the resulted matrix is converted to a colormap. The mapping is performed by using MATLAB where the maximum value in the matrix is mapped to white and the minimum value in the matrix is mapped to black. The other values are linearly mapped from black through shades of red, orange, and yellow, to white.

In Fig. 3.3, two-dimensional images generated with a 0.85 mm SNG layer (Fig. 3.3(a))

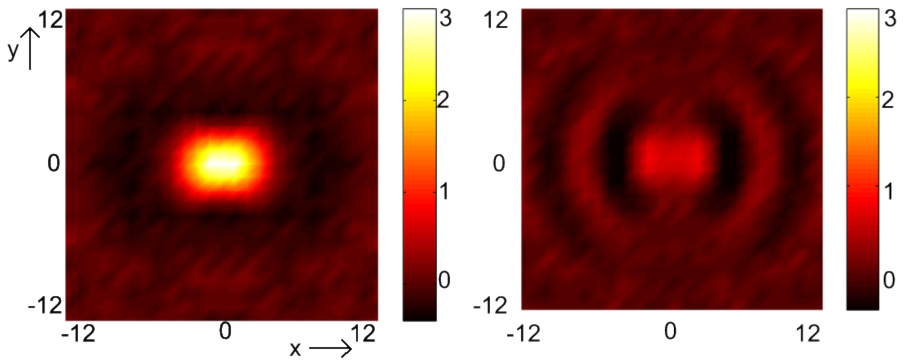

(a) (b)

Figure 3.3: The image of the 1 mm crack generated by scanning the waveguide in the x-y plane. (a) With an 0.85 mm SNG layer having 0.2 loss tangent. (b) Without an SNG layer.

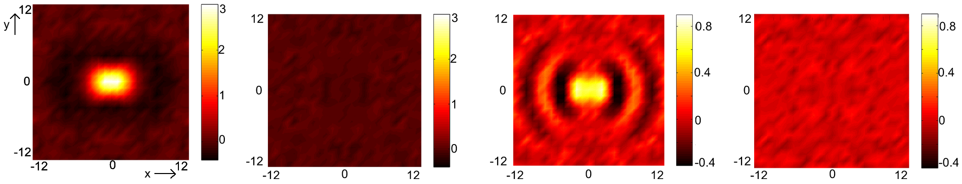

(a) (b) (c) (d)

Figure 3.4: Images of 1 mm ($\lambda/10$) real and ghost targets. (a) and (b) are the images generated with the SNG layer. (c) and (d) are the images generated without the SNG layer

and without an SNG layer (Fig. 3.3(b)) are presented. The image without the SNG layer is in good agreement with the experimental images reported in Ref [11]. When there is no SNG layer, side lobes are noticeable. The magnitude of the side lobes are close to the half of the magnitude of the main lobe. On the other hand when the SNG layer is present, the side lobes are 10 times smaller compared to the main lobe. Therefore a sharper and a more distinct image of the crack is generated using the SNG layer, implying higher resolution and higher focusing.

To show the numerical error due to the meshing, the 2D images are plotted using different colormaps with the ghost target images in Fig 3.4. The ghost target images generated with and without the SNG layer present phase fluctuations of 0.2936° and 0.2239°, respectively. To quantify the meshing error, the meshing error ratio is defined as the maximum fluctuation due to the ghost target divided by the maxima obtained by the real target. The meshing error ratios become 0.0917 and 0.2731 for the with and without SNG cases, respectively.

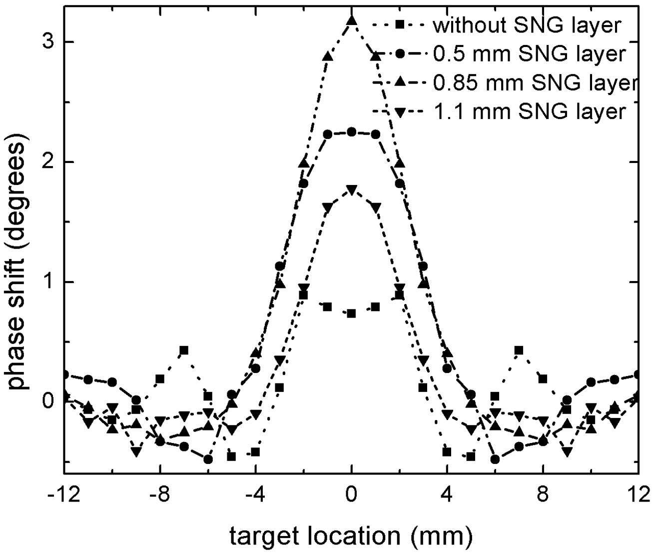

Figure 3.5: Phase shift as a function of the target relative location with respect to the center of the waveguide. As the thickness of the SNG layer is increased the side lobes decrease. The best image is observed at 0.85 mm

The computational cost can be significantly reduced by generating one-dimensional images instead of two-dimensional images. Fig. 3.5 shows the phase variation as the probe moves along the x-axis for different SNG-layer thickness values. (The smaller dimension of the waveguide is along the x-direction.) As the SNG thickness is increased, the image becomes sharper until a maximum is reached beyond which the sharpness of the images starts to decrease. The images shown in In Fig. 3.6 correspond to the cases shown in Fig. 3.5. The same color map is used for each image to express the improvement on the image quality and the sensitivity obtained by the SNG layers. The sensitivity improvement of the proposed method is also tested for smaller target of 0.05λ cubic crack. The image for the 0.05λ crack with and without an 0.85 mm (0.085λ) SNG layer is shown in Fig. 3.7. The phase shift is observed to increase from 0.098° to 0.38°.

3.3.2 Standoff Distance and SNG Thickness Optimization

Another important probe parameter is the standoff distance. In this section, the study of changing standoff distance and the SNG layer thickness simultaneously in order to achieve higher sensitivity is presented. First, the phase of the reflection coefficient is analyzed as a function of the standoff distance with different SNG thicknesses. An aluminum plate

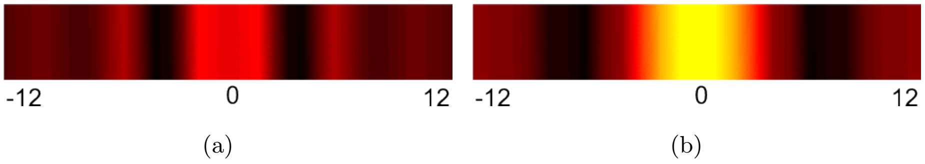

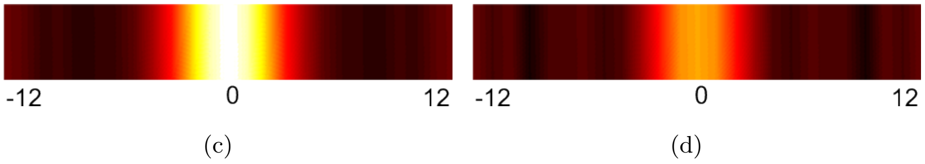

Figure 3.6: One-dimensional images obtained by scanning along an axis that cuts through a 1 mm (0.1λ) crack for different SNG-layer thickness. (a) no SNG layer (b) 0.5 mm (0.05λ) SNG layer, (c) 0.85 mm (0.085λ) SNG layer, (d) 1.1 mm (0.11λ) SNG layer.

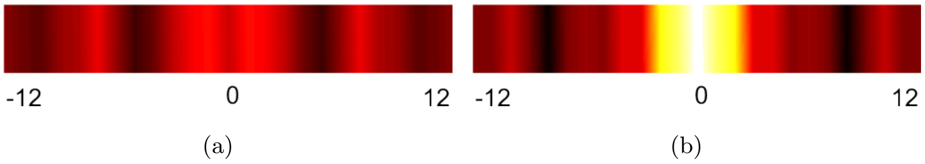

Figure 3.7: One-dimensional images obtained by scanning along an axis that cuts through an 0.5 mm (0.05λ) crack. (a) no SNG layer (b) 0.85 mm (0.085λ) SNG layer.

without any crack is placed as shown in Fig. 3.1. Fig. 3.8 shows the phase change as a function of the standoff distance. When there is no SNG layer, the reflection phase is changed with a constant slope. When an SNG layer is inserted, the plot has a high slope region between 1 mm (0.1λ) to 1.2 mm (0.12λ) standoff distance. The highest slope is achieved with a 0.9 mm (0.09λ) SNG thickness. From this behavior, it can be concluded that, the reflection coefficient is very sensitive to changes on the aluminum plate when the slope is very high.

In Fig. 3.9, the phase shift due to a 1 mm sided cubic crack is plotted as a function of the standoff distance for different SNG thicknesses. The phase shift due to the crack is defined as the difference in reflection phases when there is a crack at the center of the plate and when there is a *ghost target*. The ghost target is defined as mentioned in the previous section to extract the meshing error.

When there is no SNG layer, the maximum phase shift due to the target is 0.73°. The phase shift changes between 0.7° to 0.73° until 1.3 mm (0.13λ) standoff distance. For standoff distances larger than 1.3 mm (0.13λ), the phase shift reduces. When there is an SNG layer, the phase shift has a maximum value between 1 to 1.2 mm (0.12λ) standoff distance as predicted in Fig. 3.8. A maximum phase shift of 27.56° is achieved with a 0.9

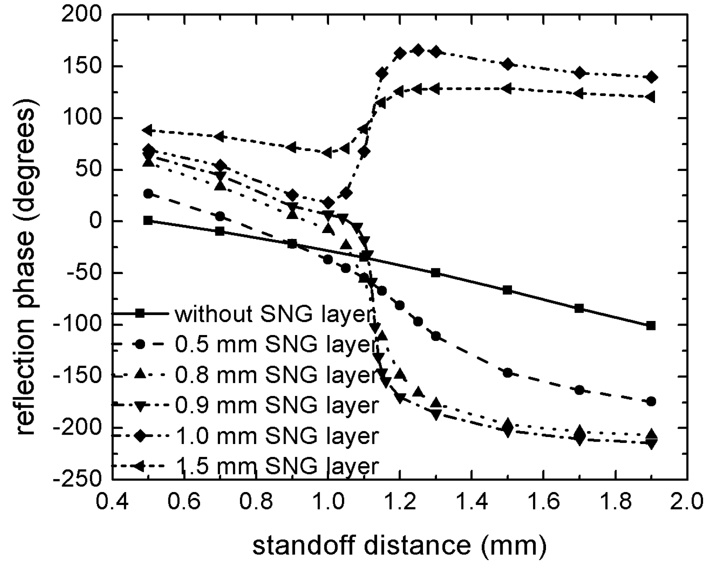

Figure 3.8: The phase of the reflection coefficient as a function of standoff distance. When the SNG thickness is increased, a region with a very high slope is encountered. The high slope indicates that, in this region the probe is very sensitive to changes on the plate.

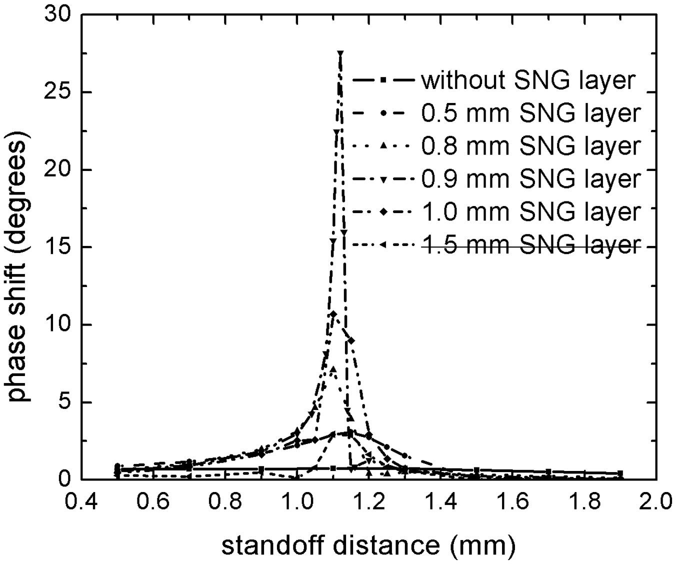

Figure 3.9: Phase shift due to the target as a function of the standoff distance. Sensitivity reaches the highest value within the region where Fig. 3.8 has maximum slope.

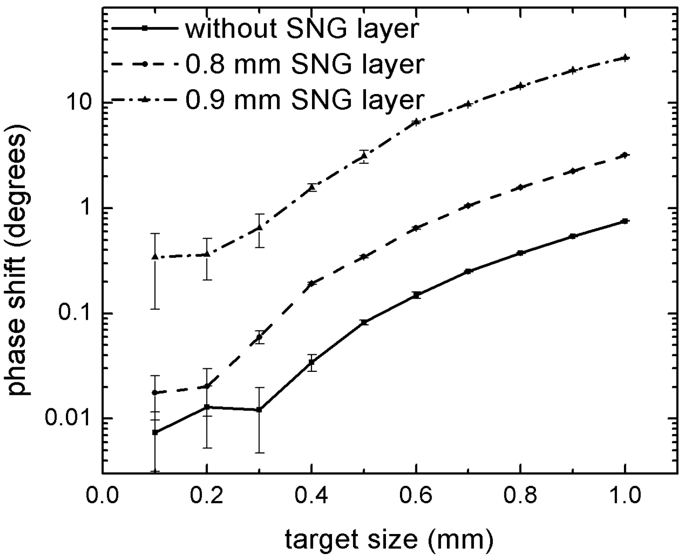

Figure 3.10: Phase shift as a function of the target size. The behavior of the probe configurations are similar. The standoff distance is 1.12 mm (0.112λ) for 0.9 mm (0.09λ) SNG thickness case and 1.1 mm (0.11λ) for the others.

mm (0.09λ) SNG thickness and a 1.12 mm (0.112λ) standoff distance.

The sensitivity improvement is also valid for smaller targets. In Fig. 3.10, phase shifts generated as a function of target size are presented. Three probe cases are analyzed. All cases have similar behavior as the target size increases. When the optimum SNG thickness and standoff distance is used, a 0.3 mm (0.03λ) sided cubic crack gives the same phase shift as a 1 mm (0.1λ) sided cubic crack when there is no SNG layer. The error bars presented in Fig. 3.10 are generated by calculating the standard deviation of the last five adaptive passes in the solution process.

2D Images

In order to visualize the sensitivity improvement and compare the image qualities, 2D images are generated by moving the probe along the $\hat{x}$ and $\hat{y}$ axes. The minimum reflection phase is subtracted from the other values to set the minimum reflection phase level to zero. Fig. 3.3 shows four images generated by four different probe systems. All images are scaled with the same colormap to show the power of using the SNG layer and optimizing the standoff distance.

In addition to the sensitivity improvement, the image quality is also analyzed. Fig. 3.12

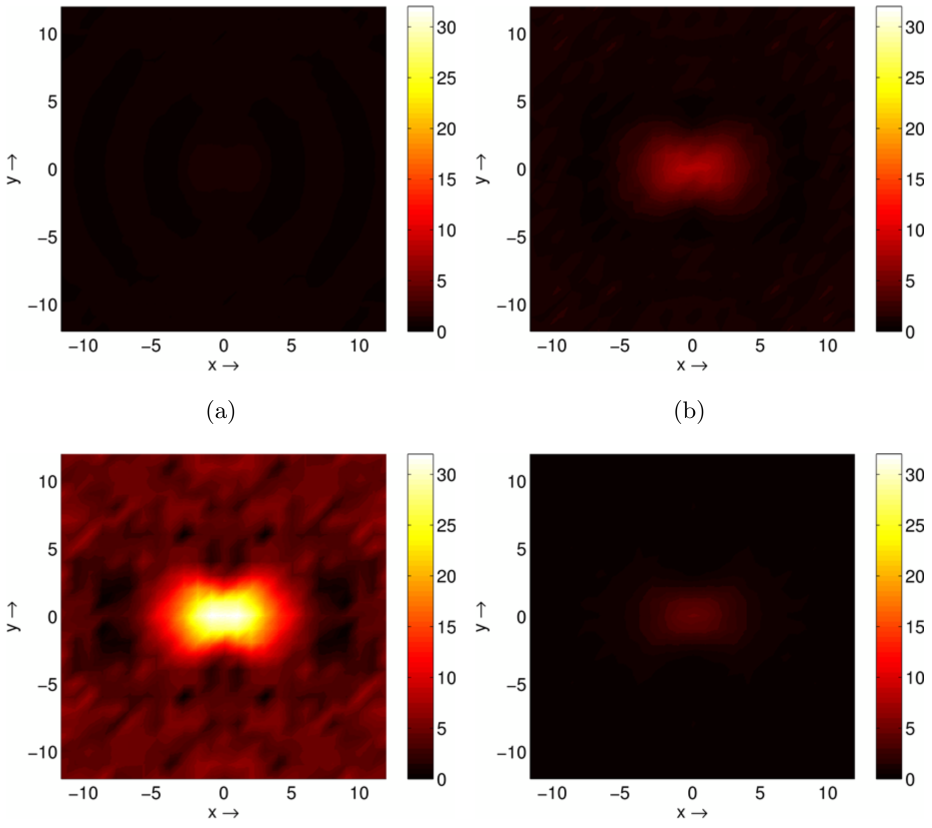

(a) (b)

(c) (d)

Figure 3.11: The image of the 1 mm (0.1λ) crack generated by scanning the waveguide in the x-y plane, (a) without SNG layer (b) with 0.8 mm (0.08λ) SNG layer (c) with 0.9 mm (0.09λ) SNG layer and (d) 1.5 mm (0.15λ) SNG layer. The standoff distance is 1.12 mm (0.112λ) for (c) and 1.1 mm (0.11λ) for the other images. The unit of the axes labels is mm and the unit of the colormap is degree.

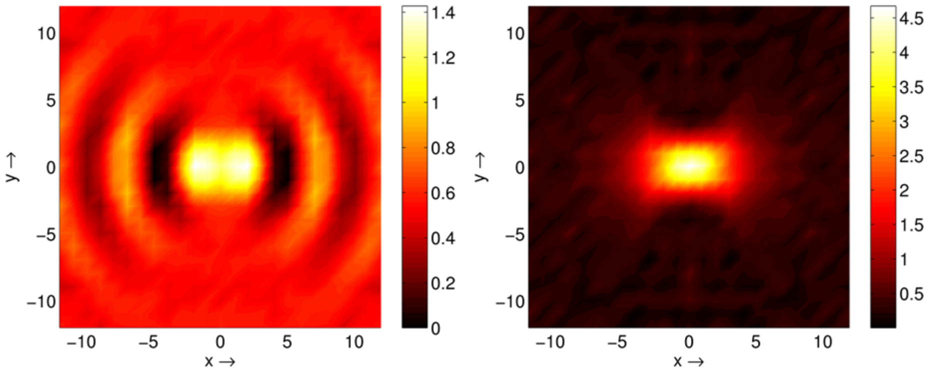

(a) (b)

Figure 3.12: The image qualities (a) without (b) with a 1.5 mm (0.15λ) SNG layer. The unit of the axes labels is mm and the unit of the colormap is degree.

shows images generated by a probe without SNG layer and a probe with 1.5 mm (0.15λ) SNG layer. Note that each image is scaled with a different colormap to indicate the image qualities. When there is no SNG layer, the image has side lobes with a magnitude close to half of the center lobe. On the other hand, the SNG layer produces a clear image without side lobes. Therefore the SNG layer improves both the sensitivity and the image quality.

The sensitivity enhancement and the image quality improvement is related to the field distribution generated by the probe. In Fig. 3.13, the field distributions at the surface of the aluminum plate are shown with and without the SNG layer. The SNG layer both amplifies the near field and concentrates the field at the opening of the waveguide. On the other hand, without the SNG layer, the field is distributed to a larger area and the field concentration at the center is not very high. Therefore side lobes with high amplitudes (compared to the center lobe) are observed.

3.4 Waveguide Structures with SNG Layers Placed Inside

Another way of using waveguide probes with SNG layers is using loaded waveguides in a similar manner described in Section 2.6. In this case the aim is to realize the amplifying region within the waveguide which reduces the required SNG material and to have a more compact overall probe design. In addition, since the waveguide forces the wave to propagate with the dominant mode, 2 dimensional SNG layers can be employed in such a structure. A μ negative SNG layer is used since the dominant mode is a TE wave.

The proposed structure is shown in Fig 3.14. The crack is a cube with a side length of

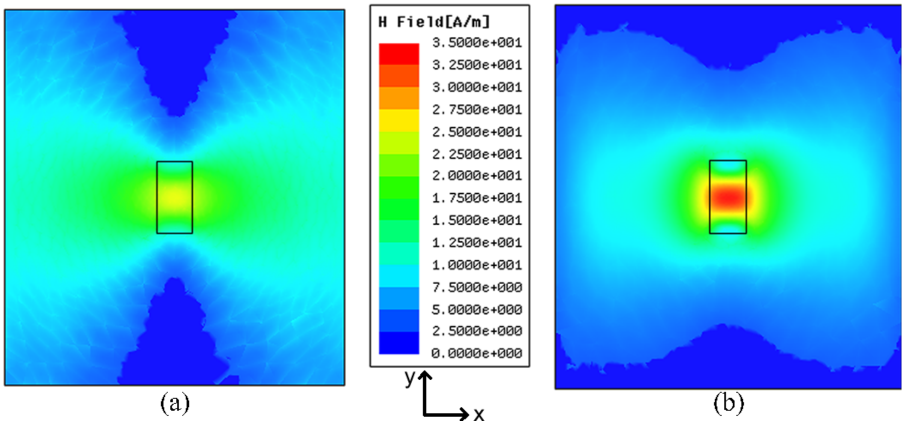

Figure 3.13: The **H** field distribution on the surface of the aluminum plate, (a) without, (b) with the SNG layer. The SNG layer produces a more confined field distribution with a higher field amplitude at the center. Rectangles at the center of images show the orientation and location of the waveguide.

1.5 mm and it is filled with air. The material properties and the frequency are selected to maintain a propagating field in the dielectric region and an evanescent field in the other regions. The waveguide is same as the previous section, i.e. WR-28. It is loaded with a lossless dielectric material with a relative permittivity of $\epsilon_r = 8.8$. The cutoff frequency of a dielectric loaded waveguide is given by [47]

$$f_c = \frac{1}{2}\frac{c_0}{a\sqrt{\epsilon_r}}, \tag{3.2}$$

where c_0 is the speed of light in the free space, a is the smaller side length of the waveguide cross section. The cutoff frequency of the WR-28 waveguide loaded with $\epsilon_r = 8.8$ becomes 7.11 GHz. Therefore an operation frequency of 10 GHz is selected for the numerical experiments. Note that at 10 GHz the size of the crack becomes 0.05λ where λ is given as the free space wavelength of the operating frequency.

Similar to the Section 3.3.2, the phase of reflection coefficient is analyzed while changing the standoff distance (Fig. 3.15). A steep change in the reflection phase is observed around a standoff distance of 0.9 mm (0.03λ). The slope is maximized by using a 1.5 mm (0.05λ) SNG layer thickness.

Fig. 3.16 shows the sensitivity improvement achieved by different SNG layer thicknesses. As expected, the maximum sensitivity is achieved with a 1.5 mm (0.05λ) SNG layer thickness and a 0.9 mm (0.03λ) standoff distance. The phase shift due to a target at 0.9 mm (0.03λ) is increased by 43 times. Further increasing the SNG layer thickness results the degradation of the sensitivity improvement.

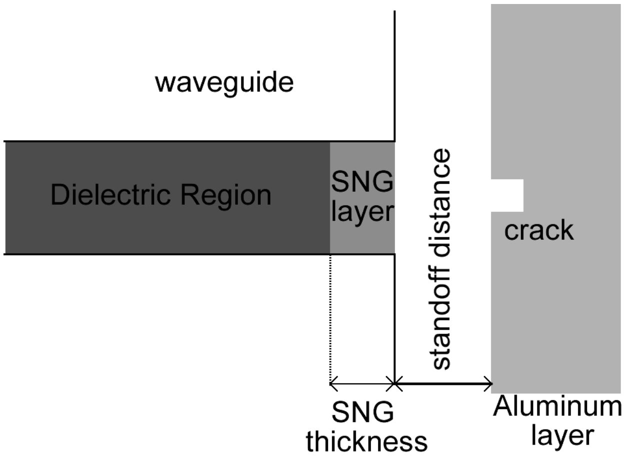

Figure 3.14: The loaded waveguide structure. The waveguide has a cross section of 7.11 mm × 3.56 mm. The crack size is 1.5 mm (0.05λ).

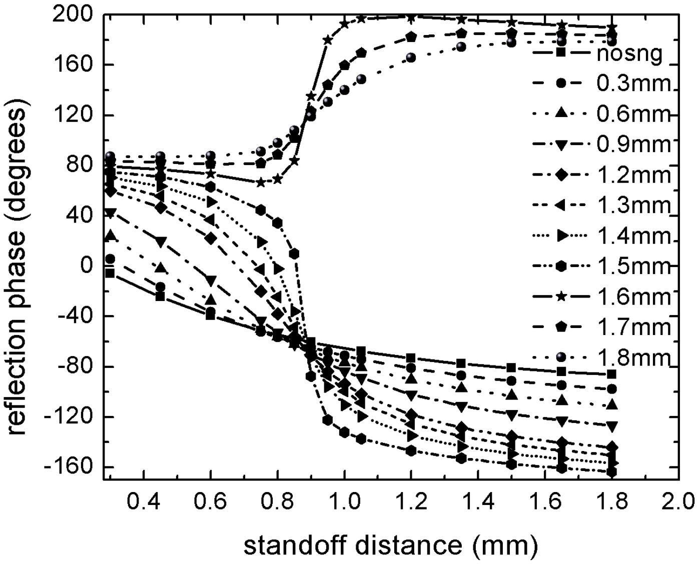

Figure 3.15: Reflection coefficient as a function of standoff distance. The maximum sensitivity is expected with a 1.5 mm (0.05λ) SNG layer thickness and a standoff distance between 0.8 mm (0.0267λ) and 1 mm (0.033λ).

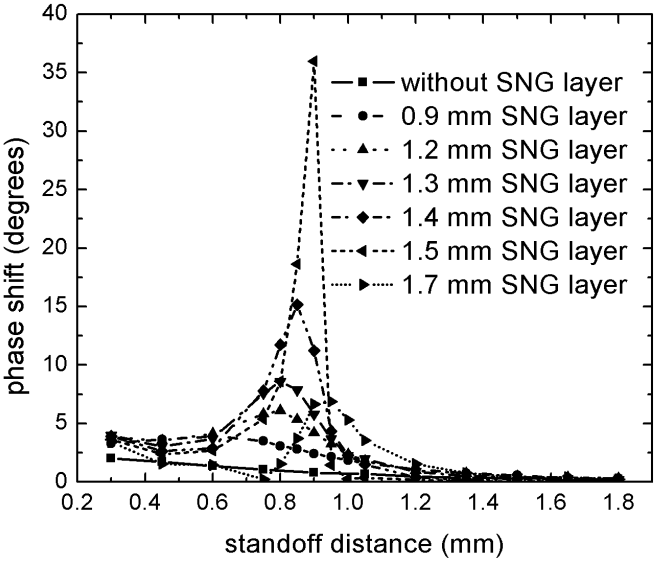

Figure 3.16: Phase shift due to the target as a function of standoff distance. The maximum improvement is achieved with a 1.5 mm (0.05λ) SNG layer thickness. The waveguide is loaded with material with $\epsilon_r = 8.8$.

The effect of the target size is analyzed in Fig. 3.17. The phase shift as a function of target size is plotted for two cases. The first case has a standoff distance of 0.6 mm (0.02λ) and does not have any SNG layer. The second case has a standoff distance of 0.9 mm (0.03λ) and an SNG layer thickness of 1.5 mm (0.05λ). For all target sizes, the phase shift improvement is between 25 to 35 times.

3.4.1 Effect of changing ϵ_r

In addition to the probe parameters described in Section 3.3, the permittivity of the dielectric material used in the waveguide is a new variable for the loaded waveguide structure. In this section, the effect of changing the permittivity of the dielectric is studied. The dimensions of the waveguide is kept constant and the operation frequency is 10 GHz for all cases.

While choosing ϵ_r, there are two constraints. The operation frequency, 10 GHz, must be above the cutoff frequency of the dominant mode and it must be smaller than the cutoff frequency of the next mode. So that a single mode is excited in the waveguide.

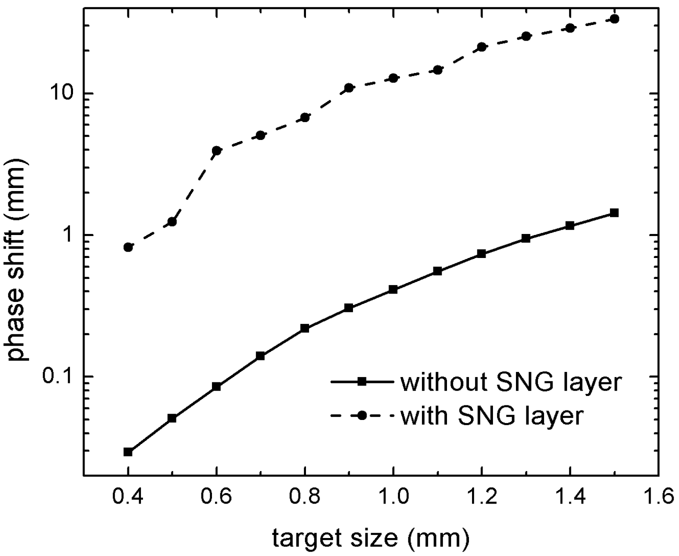

Figure 3.17: The sensitivity as a function of target size. A constant sensitivity improvement is maintained over target sizes from $\lambda/75$ to $\lambda/20$.

The cutoff frequency of a TE_{mn} or TM_{mn} mode in a rectangular waveguide is given by [47]

$$f_{c_{mn}} = \frac{1}{2}\frac{c_0}{\sqrt{\mu_r \epsilon_r}}\sqrt{\left(\frac{m}{a}\right)^2 + \left(\frac{n}{b}\right)^2}, \tag{3.3}$$

where c_0 is the speed of light in the free space, a and b are the side lengths of the waveguide cross section. In order the TE_{10} mode at 10 GHz to propagate in a WR-28 waveguide, the waveguide must be loaded with an $\epsilon_r = 4.451$. Similarly the cutoff condition for the next mode, TE_{20} or TE_{01} is $\epsilon_r = 17.7$. Therefore the sensitivity behavior with ϵ_r values of 7, 6, and 5 are analyzed.

Figs 3.18-3.20 show the phase shifts due to a 1.5 mm (0.05λ) sided cubic target. All relative permittivity values exhibits similar improvement behaviors. As ϵ_r gets smaller the optimum standoff distance increases. Therefore application specific standoff distances can be adjusted by changing the loading material.

3.5 Conclusion

In this chapter, it was demonstrated that the sensitivity of waveguide probes can be enhanced by using SNG media. The sensitivity enhancement is a direct consequence of the evanescent field amplification property of SNG media. The amplification becomes highly

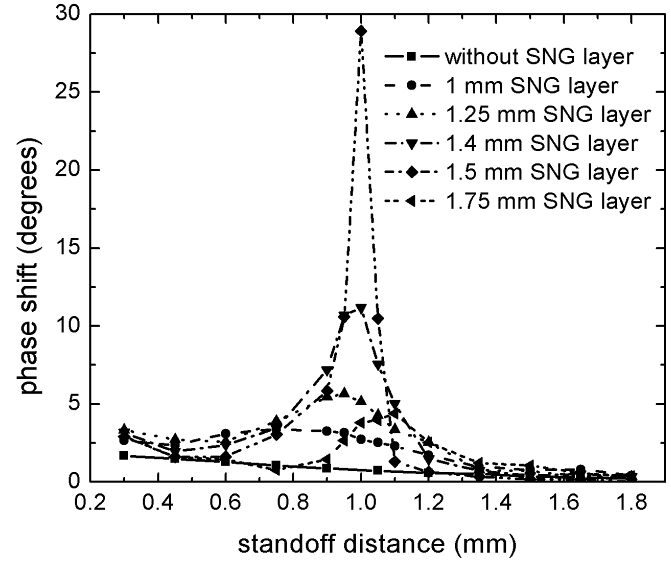

Figure 3.18: Phase shift due to the target as a function of standoff distance. The maximum improvement is achieved with a 1.5 mm (0.05λ) SNG layer thickness. The waveguide is loaded with material with $\epsilon_r = 7$

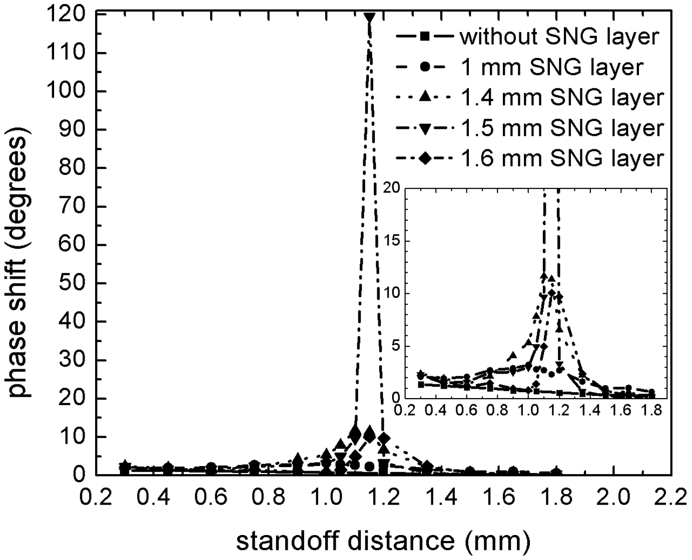

Figure 3.19: Phase shift due to the target as a function of standoff distance. The maximum improvement is achieved with a 1.5 mm (0.05λ) SNG layer thickness. The waveguide is loaded with material with $\epsilon_r = 6$

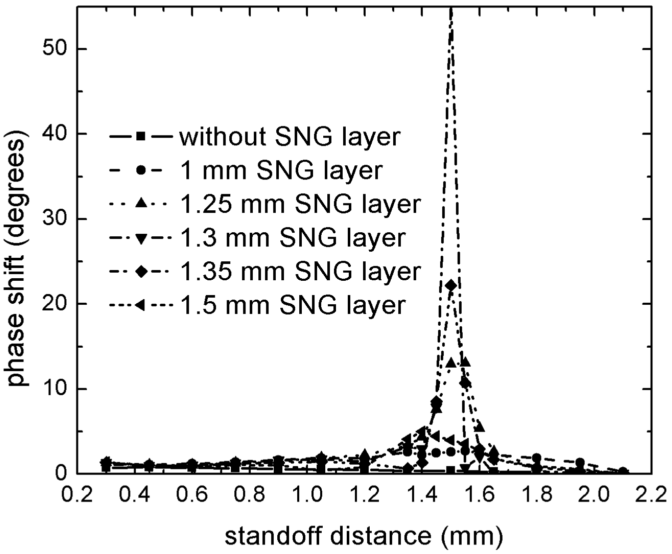

Figure 3.20: Phase shift due to the target as a function of standoff distance. The maximum improvement is achieved with a 1.3 mm (0.0433λ) SNG layer thickness. The waveguide is loaded with material with $\epsilon_r = 5$. The optimum standoff distance is shifted to 1.5 mm (0.05λ).

pronounced when maximum transmission through the SNG medium is achieved. To demonstrate the effectiveness of the new SNG-enhanced waveguide probe, the detection of precursor pitting in aluminum plates is studied. It is shown that by adding an SNG layer without changing any other probe parameter, sharper images are produced and the phase shift due to a 1 mm $(0.\lambda)$ cubic crack is enhanced by 4 to 5 times by using a μ-negative SNG layer with a magnetic loss tangent of 0.2 in comparison to the case of a probe without an SNG medium. The method presented here can be applied to other types of probes based on near-field detection modalities.

Furthermore by optimizing the standoff distance, the phase shift due to the target is improved by 35 times compared to the case without SNG layer.

Loaded rectangular waveguides are also studied. Loaded waveguides present a more compact probe design and requires less SNG material compared to the air filled waveguides.

Chapter 4

Application to Open-ended Coaxial Line Structures

4.1 Introduction

Open-ended coaxial line probes have been successfully implemented to near field characterization schemes such as detecting delamination in IC packages [14, 15, 86], fatigue cracks in stainless steel [16], and characterization of layered dielectrics [17, 87]. Since the coaxial line structures does not have any cutoff frequency, the frequency and cross section size selection is more flexible compared to the open-ended waveguide structures.

In this chapter, the sensitivity improvement of coaxial line probes using an ϵ-negative material is presented. Detection of an electrically small crack on an aluminum plate is studied.

4.2 Theory and Setup

When an open-ended coaxial line is placed next to a multilayer dielectric medium backed with a conducting sheet, the evanescent field generated by the coaxial line is dominated by the TM modes [88, 89]. Therefore the field emanated by a coaxial line can be amplified by using an ϵ-negative SNG layer. An evanescent TM wave incident on an ϵ-negative SNG layer experiences a transmission singularity when the condition [22]

$$e^{-jk'_z a_c} = \frac{(k_z\epsilon' + k'_z\epsilon)^2}{(k_z\epsilon' - k'_z\epsilon)^2}, \tag{4.1}$$

is satisfied. In equation 4.1, ϵ' and ϵ represent permittivities of the SNG layer and the surrounding, respectively. a_c is the thickness of the SNG layer. k'_z and k_z are the decay

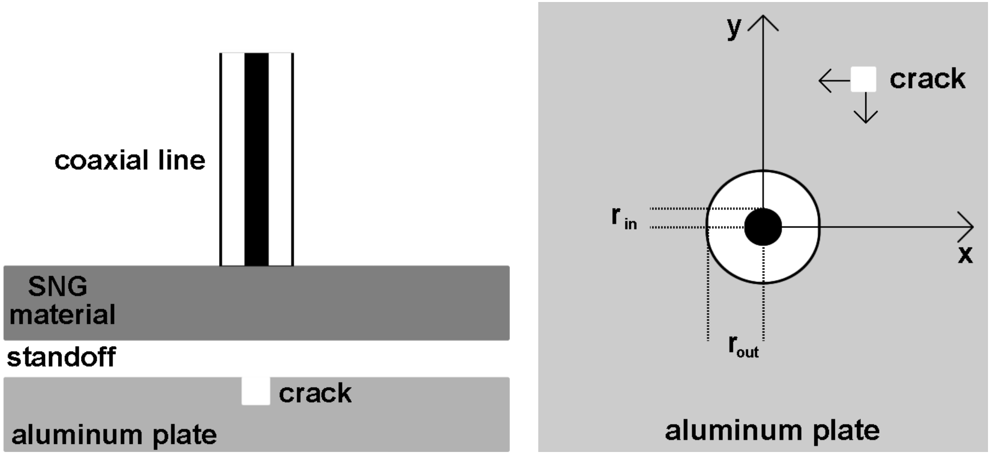

(a) (b)

Figure 4.1: (a) Side view of the setup. An SNG layer is placed immediately at the opening of the coaxial line. (b) The crack is moved on the xy plane to generate 2D images. This is same as having a crack at the origin and scanning the probe.

constants inside and outside the SNG layer, respectively. In order to obtain the maximum enhancement, the thickness of the SNG layer must be close to a_c.

The setup consists of an open ended coaxial line, an ϵ-negative layer and an aluminum plate with a $\lambda/20$ sided cubic crack at the center as shown in Figure 4.1(a). λ is the free space wavelength (10 mm) of the operation frequency, 30 GHz. The dielectric of the coaxial line is assumed to be vacuum. The inner radius and outer radius of the coaxial line satisfy [47]

$$\frac{r_{out}}{r_{in}} = e^{2\pi Z_0\sqrt{\epsilon/\mu}} = 2.3, \tag{4.2}$$

to obtain a 50 Ω characteristic impedance. The electrical properties of the SNG material are $\epsilon = -1$, $\mu = 1$, and $\tan\delta = -0.2$. The phase shift due to the crack is calculated by subtracting the reflection phase when there is a crack from the reflection phase without the crack.

4.3 Sensitivity Improvement

In Figure 4.2, the phase shift due to the target is plotted as a function of standoff distance for different SNG layer thicknesses. r_{in} is equal to $\lambda/20$ and the crack is placed at the origin, facing the inner conductor of the coaxial line (see Figure 4.1(b)). The phase shift without any SNG layer is 5.5° at $\lambda/100$ standoff distance. As the standoff distance increases, the phase shift reduces. When an SNG layer is employed, the phase shift is

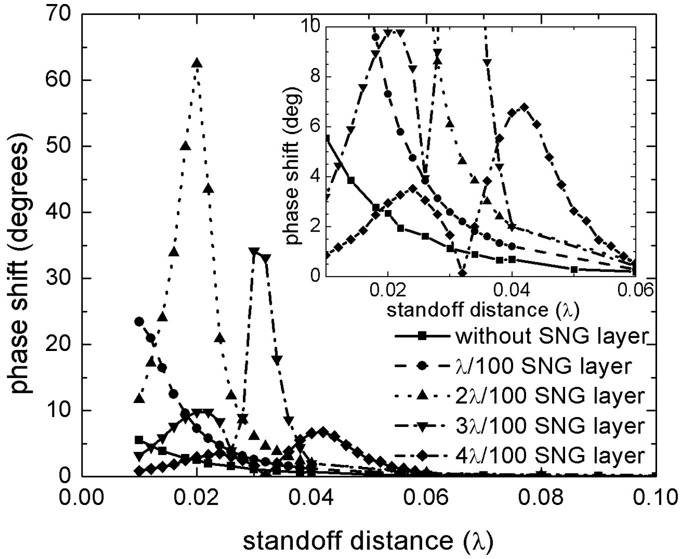

Figure 4.2: The phase shift as a function of standoff distance for different SNG thicknesses. The coaxial line parameters are $r_{in} = \lambda/20$ and $r_{out} = 2.3\lambda/20$.

increased. For each SNG thickness, there is an optimum standoff distance at which the sensitivity due to the crack is maximized. The optimum standoff distance increases as the SNG thickness increases. Maximum sensitivity is achieved with a $\lambda/50$ SNG layer and $\lambda/50$ standoff distance. The phase shift is improved to 62.5°.

In Figure 4.3, a bigger coaxial line is used. r_{in} is equal to $1.5\lambda/20$. Since fields generated by probes with larger aperture sizes usually have smaller spatial frequencies, a bigger probe is expected to generate evanescent fields with smaller decay constants. Therefore the singularity condition is expected at larger thicknesses. The optimum structure is a $\lambda/25$ SNG layer with a $3\lambda/50$ standoff distance. A 6.1 times improvement in the phase shift is achieved compared to the case without SNG layer and a $\lambda/100$ standoff distance.

In Figure 4.4 and Figure 4.5, 2D images generated by moving the target in the xy plane are presented (see Figure 4.1(b)). Smaller coaxial line produces better images since the image size is closer to the original crack size ($\lambda/20 = 0.5$ mm) compared to the bigger probe. This is a result of having a smaller aperture size which gives a more confined near field. When the optimum SNG thickness and standoff distance are used (Figure 4.4(b) and Figure 4.5(b)), both the width of the center peak is reduced and the side lobes are eliminated. As a result the image quality is improved. Note that in each image, a different colormap is used to emphasize image qualities.

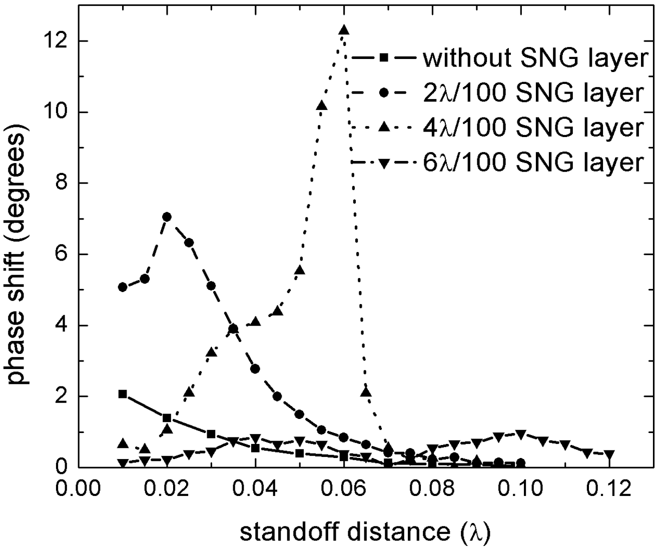

Figure 4.3: Sensitivity improvement for a coaxial line with $r_{in} = 1.5\lambda/20$. When the coaxial line size is increased, the maximum sensitivity shifts to the higher standoff distances. But the maximum sensitivity value reduces.

4.4 Effect of Changing the Dielectric Insulator

In real world applications, coaxial lines have dielectric materials different than vacuum. Therefore the effect of using materials with different permittivities on the sensitivity is studied. In order to keep the aperture size constant the outer radius of the probe is fixed to $r_{out} = 2.3\lambda/20$ which is equal to the outer radius of the probe used for generating the results shown in Figure 4.2. Therefore the inner radius of the probe is selected so that the aperture size is constant and the characteristic impedance is 50 Ω:

$$r_{in} = \frac{2.3\lambda e^{-0.833\sqrt{\epsilon_r}}}{20}. \tag{4.3}$$

Figures 4.6-4.9 show the sensitivity results for ϵ_r ranging from 2 to 5. The sensitivity behavior of the cases without SNG layer are close to each other. Phase shifts due to a crack with a standoff distance of 0.01λ, without the SNG layer are between 6.7° and 7.7° for all ϵ_r values. The sensitivity improvement is valid for all dielectric materials studied here. Increasing the permittivity of the dielectric material increases the maximum sensitivity obtained by the optimum SNG thickness and standoff distance.

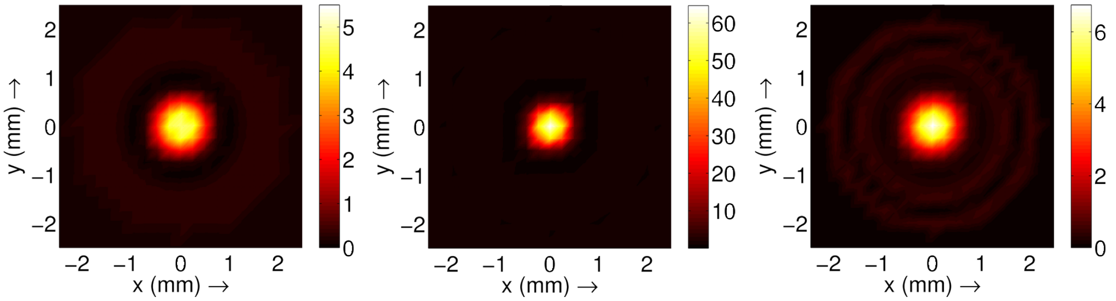

(a) (b) (c)

Figure 4.4: 2D images generated by coaxial line with $r_{in} = \lambda/20$ (a) without SNG layer and $\lambda/100$ standoff distance (b) $\lambda/50$ SNG layer and $\lambda/50$ standoff distance, and (c) $\lambda/25$ SNG layer and $\lambda/25$ standoff distance

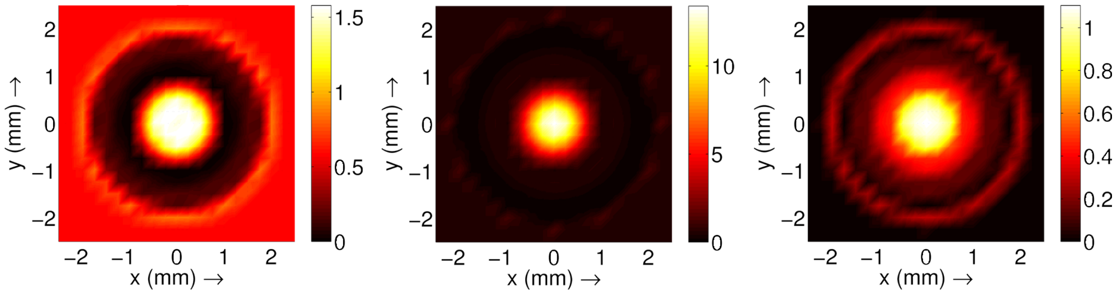

(a) (b) (c)

Figure 4.5: 2D images generated by coaxial line with $r_{in} = 1.5\lambda/20$ (a) without SNG layer and $\lambda/100$ standoff distance (b) $\lambda/25$ SNG layer and $3\lambda/50$ standoff distance, and (c) $3\lambda/50$ SNG layer and $\lambda/10$ standoff distance

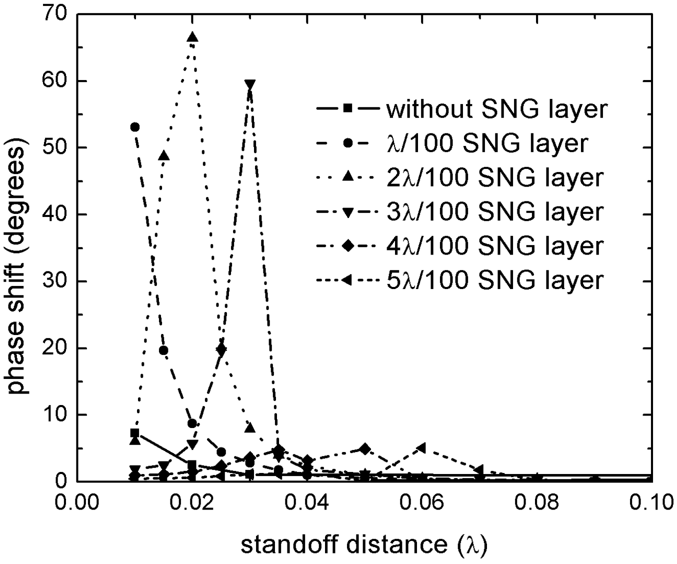

Figure 4.6: Sensitivity improvement for a coaxial line with $r_{out} = 2.3\lambda/20$ and a dielectric material with $\epsilon_r = 2$

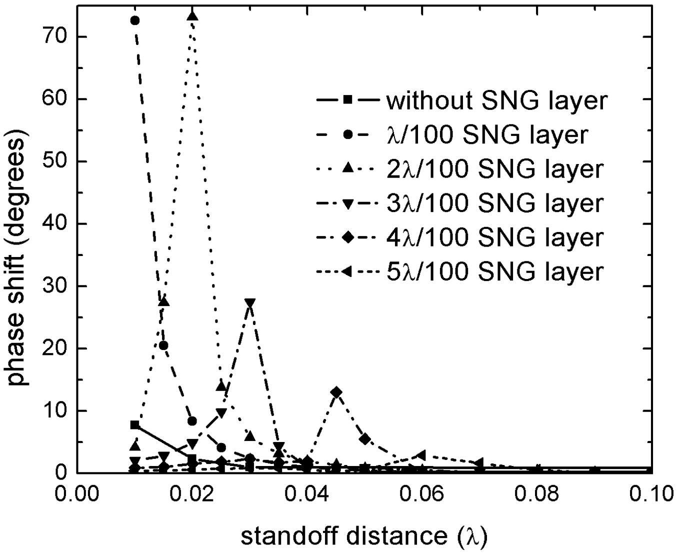

Figure 4.7: Sensitivity improvement for a coaxial line with $r_{out} = 2.3\lambda/20$ and a dielectric material with $\epsilon_r = 3$

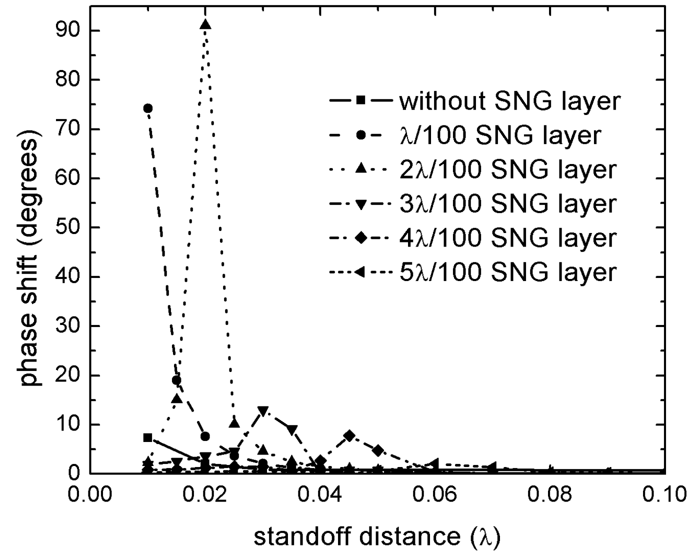

Figure 4.8: Sensitivity improvement for a coaxial line with $r_{out} = 2.3\lambda/20$ and a dielectric material with $\epsilon_r = 4$

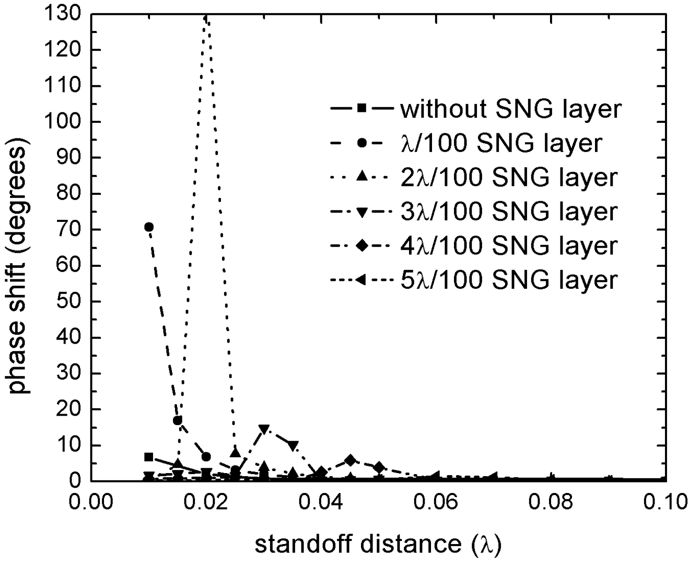

Figure 4.9: Sensitivity improvement for a coaxial line with $r_{out} = 2.3\lambda/20$ and a dielectric material with $\epsilon_r = 5$

4.5 Conclusion

The sensitivity of coaxial line probes is improved using ϵ-negative materials. Phase shift is improved by 11 times with the optimum SNG thickness and standoff distance combination. When the coaxial line size is increased, evanescent fields with smaller decay constants are emanated. Therefore the optimum SNG thickness is increased when the coaxial line radius is increased. The SNG layer also increases the image quality. Smaller probes produces better images. When the permittivity of the dielectric material used in the coaxial line is increased, the sensitivity improvement increases.

Chapter 5

Application to Electrically Small Dipoles

5.1 Introduction

Electrical dipoles are well known radiators consisting of two pieces of conductive wires or rods. When the dipole length is much smaller than the operation wavelength, the structure is known to generate a near field distribution dominated by electric field. The response of the small dipole is highly capacitive and as a result the structure is hardly radiating. Therefore an electrically small dipole is a well known TM mode near field generator.

In this Chapter, the sensitivity improvement of electrically small dipoles are presented. A dipole placed in the center of concentric spherical shells is theoretically studied. Numerical results showing the sensitivity improvement achieved by metmaterial layers inserted between a small dipole probe and target are presented. In Chapters 3 and 4, μ-negative and ϵ-negative SNG layers are used for sensitivity improvement of near field probes. In this chapter, DNG materials are used to improve the sensitivity of electrically small dipoles. Therefore all types of negative materials are proved to be effective for sensitivity enhancement.

5.2 Theory

5.2.1 Fields due to a Small Dipole

An electrically small dipole is assumed to have a length of l much smaller than λ. Therefore a dipole oriented in $\hat{z}$ direction has a constant current distribution as [90]

$$I(z) = \hat{z} I_0 \tag{5.1}$$

for $-l/2 \leq z \leq l/2$. Therefore the vector potential, $\mathbf{A}$, becomes

$$\mathbf{A} = \hat{z} \frac{\mu I_0 l}{4\pi r} e^{-jkr} \tag{5.2}$$

where r is the distance from the origin, k is the wave number at the operating frequency. By transforming the coordinate system to the spherical coordinates and using the relation between $\mathbf{A}$ and $\mathbf{H}$, the $\mathbf{H}$ field components can be found as

$$\mathbf{H} = \frac{1}{\mu} \nabla \times \mathbf{A} \tag{5.3}$$

$$\Rightarrow \quad H_\phi = \frac{jkI_0 l \sin\theta}{4\pi r} \left[1 + \frac{1}{jkr} \right] e^{-jkr}, \quad H_\theta = 0, \quad H_r = 0. \tag{5.4}$$

By using $\nabla \times \mathbf{H} = j\omega\epsilon\mathbf{E}$, $\mathbf{E}$ field components become

$$E_r = \frac{\eta I_0 l \cos\theta}{2\pi r^2} \left[1 + \frac{1}{jkr} \right] e^{-jkr} \tag{5.5}$$

$$E_\theta = \frac{j\eta I_0 l \sin\theta}{4\pi r} \left[1 + \frac{1}{jkr} - \frac{1}{(kr)^2} \right] e^{-jkr} \tag{5.6}$$

$$E_\phi = 0, \tag{5.7}$$

where η is the wave impedance of the medium, $\sqrt{\mu / \epsilon}$.

5.2.2 Sensitivity Analysis of a Dipole in a Spherical Metamaterial Shell

As shown in Eqs. 5.4-5.7, a small dipole generates spherically symmetric fields. In order to maintain the spherical symmetry, the DNG and target regions are defined as spherical shells. Therefore the probe-target system becomes a multilayered spherical structure as shown in Fig. 5.1.

The problem of a small dipole placed in a spherical DNG shell is studied in Ref. [91], where the radiation properties of the dipole is analyzed. In Ref. [91], the investigated structure consists of three regions. In this section the number of shells is increased to introduce the target region and effects of the radius of target region on the radiation properties are analyzed.

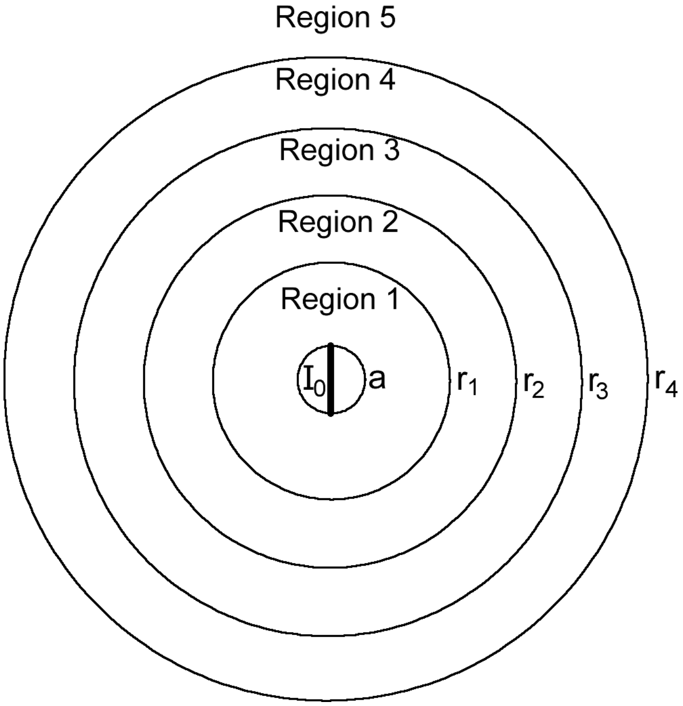

Figure 5.1: Multilayer structure in spherical coordinates. Each region has associated permittivity and permeability.

In Fig. 5.1, Region 2 and Region 4 represent the DNG and the target regions, respectively. Region 1 and Region 4 are the probe-to-DNG and DNG-to-target regions, respectively. Each region assumed to have a corresponding permittivity of ϵ_n and permeability of μ_n. The inner sphere with the radius of a is assumed to be the probe and the field inside this sphere is not solved. It is assumed that the probe generates an incident field as given in Eq. 5.4 and fields in the other regions are formed according to the Helmholtz equation and the boundary conditions.

In spherical coordinates, the Helmholtz Equation becomes [76]

$$\frac{1}{r^2}\frac{\partial}{\partial r}\left(r^2\frac{\partial\psi}{\partial r}\right)+\frac{1}{r^2\sin\theta}\frac{\partial}{\partial\theta}\left(\sin\theta\frac{\partial\psi}{\partial\theta}\right)+\frac{1}{r^2\sin^2\theta}\frac{\partial^2\psi}{\partial\phi^2}+k^2\psi=0. \tag{5.8}$$

By using separation of variables, the r, ϕ and θ dependencies of ψ can be expressed by three separate functions. Considering the field generated by a small dipole, the fields are not expected to change by ϕ. In order to satisfy the boundary conditions, the θ dependency of the $\mathbf{H}$ field must be in the form of $\sin\theta$. Since the solution of Eq. 5.8 is a function of r in the form of spherical Bessel functions the fields associated by the regions shown in Fig. 5.1 can be written as follows:

Region 1

$$H_\phi = \frac{jk_1 I_0 l \sin\theta}{4\pi r}\left[1 + \frac{1}{jk_1 r}\right] e^{-jk_1 r} + C_1 \sin\theta j_1(k_1 r) \tag{5.9}$$

$$\begin{aligned} E_\theta = {} & \frac{j\eta_1 k_1 I_0 l \sin\theta}{4\pi r}\left[1 + \frac{1}{jk_1 r} - \frac{1}{(k_1 r)^2}\right] e^{-jk_1 r} \\ & + \frac{C_1 \sin\theta}{j\omega\epsilon_1 r}\left[k_1 r j_1'(k_1 r) + j_1(k_1 r)\right] \end{aligned} \tag{5.10}$$

$$E_r = \frac{\eta_1 I_0 l \cos\theta}{2\pi r^2}\left[1 + \frac{1}{jk_1 r}\right] e^{-jk_1 r} + \frac{2C_1 \cos\theta}{j\omega\epsilon_1 r} j_1(k_1 r) \tag{5.11}$$

Region 5

$$H_\phi = C_8 \sin\theta h_1^{(2)}(k_5 r) \tag{5.12}$$

$$E_\theta = \left(-\frac{C_8 \sin\theta}{j\omega\epsilon_m r}\right)\left(k_5 r h_1^{(2)'}(k_5 r) + h_1^{(2)}(k_5 r)\right) \tag{5.13}$$

$$E_r = \frac{2C_8 \cos\theta}{j\omega\epsilon_m r} h_1^{(2)}(k_5 r) \tag{5.14}$$

Region m, $2 \leq m \leq 4$

$$H_\phi = C_{2m-2} \sin\theta j_1(k_m r) + C_{2m-1} \sin\theta n_1(k_m r) \tag{5.15}$$

$$\begin{aligned} E_\theta = {} & \left(-\frac{\sin\theta}{j\omega\epsilon_m r}\right) \\ & \times \left(C_{2m-2}\left[k_m r j_1'(k_m r) + j_1(k_m r)\right] + C_{2m-1}\left[k_m r n_1'(k_m r) + n_1(k_m r)\right]\right) \end{aligned} \tag{5.16}$$

$$E_r = \frac{2\cos\theta}{j\omega\epsilon_m r}\left[C_{2m-2} j_1(k_m r) + C_{2m-1} n_1(k_m r)\right] \tag{5.17}$$

where j_1 and n_1 represent the first order spherical bessel functions of first and second kind, respectively. $h_1^{(2)}$ is the first order spherical hankel function of second kind. j_1', n_1' and $h_1^{(2)'}$ are the derivatives of the corresponding functions.

At the boundaries, H_ϕ and E_θ must be continuous. Therefore eight boundary conditions can be written using four boundaries and C_n values can be calculated. A MATLAB code written for calculating the coefficients is presented in Appendix D.

5.2.3 Theoretical Results

Verification of the Theory

In order to verify the calculations, the code and the functions used from MATLAB's library, the following conditions presented in Table 5.1 are studied. The variable d_n is defined as $d_n = r_n - r_{n-1}$ for $2 \leq n \leq 4$ and $d_1 = r_1 - a$.

	Condition 1	Condition 2	Condition 3	Condition 4	Condition 5
ϵ_1, μ_1	1,1	1,1	1,1	1,1	1,1
ϵ_2, μ_2	1,1	1,1	-1,-1	1,1	1,1
ϵ_3, μ_3	1,1	1,1	1,1	-1,-1	1,1
ϵ_4, μ_4	1,1	1,1	1,1	1,1	-1,-1
ϵ_5, μ_5	1,1	1,1	1,1	1,1	1,1
a	$\lambda/1000$	$\lambda/500$	$\lambda/1000$	$\lambda/1000$	$\lambda/1000$
d_1	$\lambda/500$	$\lambda/500$	$\lambda/300$	$\lambda/600$	$\lambda/900$
d_2	$\lambda/500$	$\lambda/500$	variable	$\lambda/600$	$\lambda/900$
d_3	$\lambda/500$	$\lambda/500$	$\lambda/300$	variable	$\lambda/900$
d_4	$\lambda/500$	$\lambda/500$	$\lambda/300$	$\lambda/300$	variable

Table 5.1: The five conditions used for the verification of the boundary condition solutions and the coding.

First and second conditions correspond to a small dipole in free space with a length of $\lambda/500$ and $\lambda/250$, respectively. The **H**-field strength are compared with the theoretical results generated by Eq. 5.4. Fig. 5.2 shows a good agreement between the two calculations. The error between the two theoretical calculations is 0.0235%.

Structures defined by conditions 3, 4 and 5 are identical to the case studied in Ref. [91]. Fig. 2-(a) and (b) in Ref. [91] are reproduced to validate the Poynting vector and negative material calculations. The real and reactive powers generated by the dipole can be found by using the Poynting vector

$$P_{real} + jP_{reacive} = \frac{1}{2}\oint_S (\mathbf{E} \times \mathbf{H}^*) \cdot d\mathbf{s}. \tag{5.18}$$

The effect of the DNG layer over the properties of the dipole is analyzed by two parameters [91]. First one is the radiated power gain which is defined as the ratio of the radiated real power (expressed by P_{real} in Eq. 5.18) with the DNG shell to the radiated real power without the DNG shell. The second parameter is the ratio of the normalized reactance with the DNG shell to the normalized reactance without the DNG shell. The normalized reactance is defined as

$$X_{norm} = \frac{P_{reactive}}{P_{real}}. \tag{5.19}$$

Fig. 5.3 shows the radiated power gain and reactance ratio plots generated by using the parameters given for Conditions 3, 4 and 5 in Table 5.1. All conditions generates the same plot with an average error of 0.0013%. The plot is consistent with the results presented in Ref. [91]. Note that λ used in Ref. [91] is equal to 3 cm. Therefore the

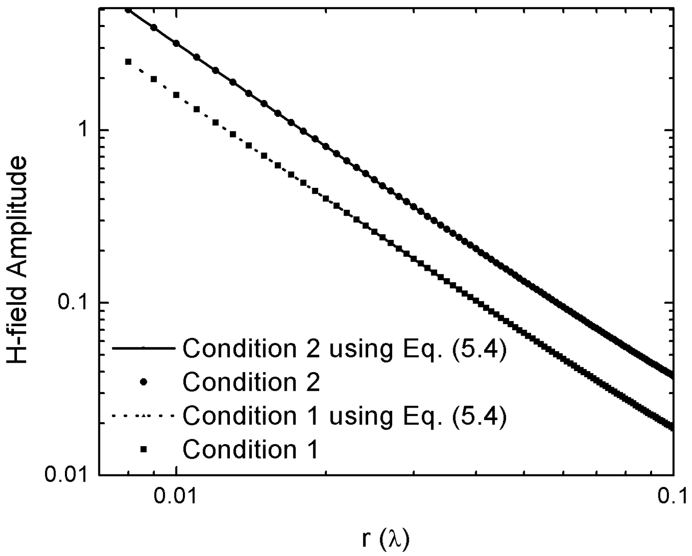

Figure 5.2: The H_ϕ amplitude due to two small dipoles, one with a length of $\lambda/250$ and the other with $\lambda/500$ are plotted by using the formulation presented in Eqs 5.9-5.17.

calculation procedure for the multi shell structure presented in Fig. 5.1 and the Poynting vector analysis are verified.

Results

In order to analyze the effect of the DNG shell on the sensitivity of the dipole, X_{norm} is analyzed as a function of the inner radius of Region 4 shown in Fig. 5.1. Region 2 is selected as the DNG layer. Region 4 is the target with material properties of $\epsilon_{target} = 6$ and $\mu_{target} = 1$. The inner radius of the DNG shell is equal to $\lambda/300$ and the length of the dipole is equal to $\lambda/500$. The target thickness, d_4, is equal to $\lambda/50$.

The change in the antenna parameters is studied as an indication of the sensitivity. The change in X_{norm} normalized by its value when $d_3 = 10\lambda$ is analyzed. The effect of DNG layer thickness is analyzed in three intervals. In the first interval the DNG layer thickness is less than $\lambda/100$. In Fig. 5.4, the change in the antenna parameter is plotted as a function of the target distance, d_3. Increasing the DNG layer thickness increases the sensitivity since the target changes the antenna parameters more. The improvement is more effective when the target distance is small. A 6.67 times improvement is achieved by using a $\lambda/100$ DNG layer.

The second interval is when the DNG shell thickness is between $\lambda/100$ and $\lambda/10$. In

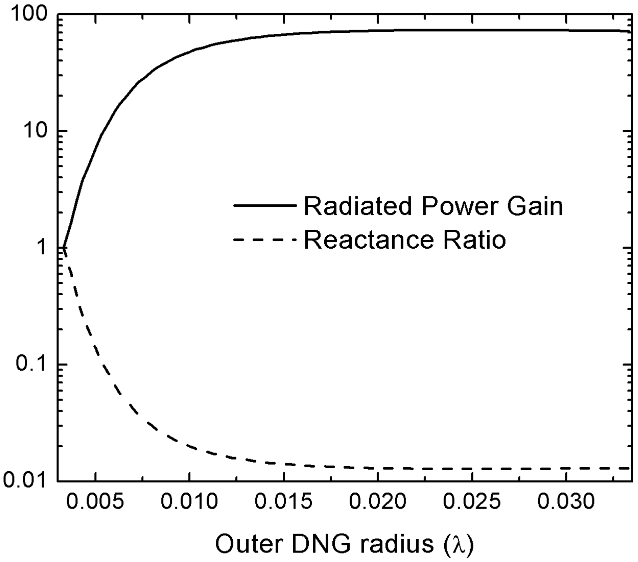

Figure 5.3: The radiated power gain and reactance ratio plots presented in Ref. [91] are generated using the formulation presented in Section 5.2.2

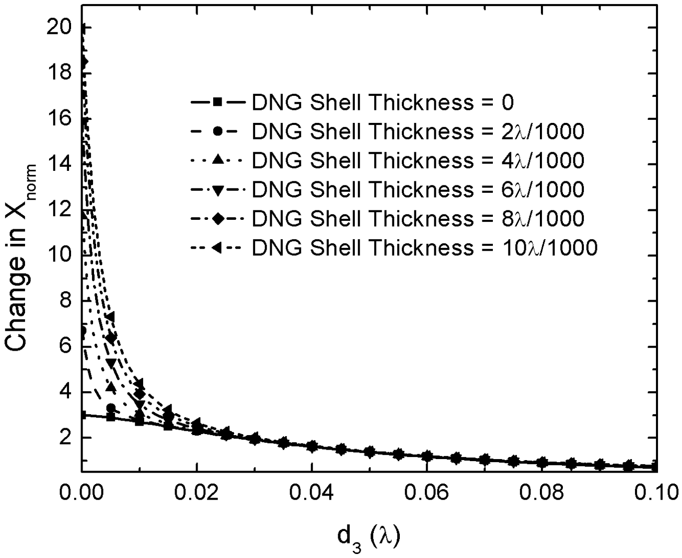

Figure 5.4: The effect of the DNG shell thickness on the sensitivity of a small dipole. When the DNG shell thickness is below $\lambda/100$, increasing DNG shell thickness increases the sensitivity. The improvement is more effective for target thicknesses smaller than 0.02λ

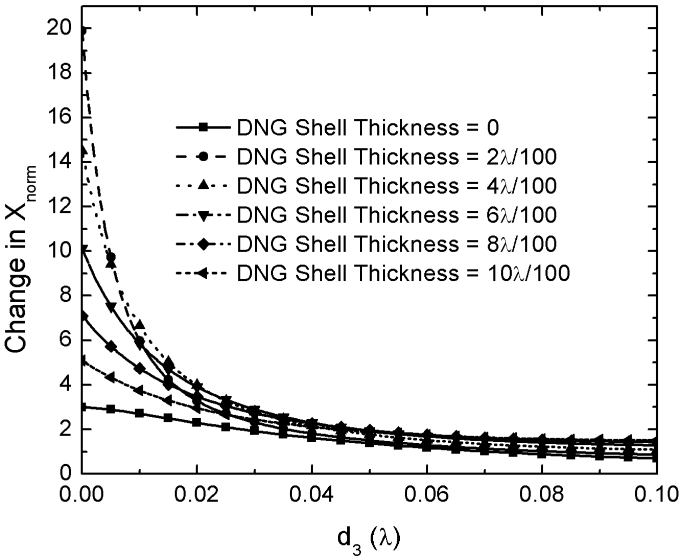

Figure 5.5: When the DNG shell thickness is between $\lambda/100$ and $\lambda/10$, the sensitivity decays slower as the target distance increases, compared to smaller DNG shell thicknesses. Therefore although as the DNG shell thickness increases the sensitivity for a target at 0 target distance decreases, the sensitivity for target distances larger than 0.01λ increases

this region the maximum sensitivity gets smaller as the d_2 increases. Nevertheless, the overall sensitivity is still larger than the case without the DNG shell. In addition, the improvement is still increased when d_3 is larger than 0.01λ.

The third interval is when the DNG shell thickness is greater than $\lambda/10$. In this case the sensitivity is reduced compared to the case without the DNG layer.

5.3 Numerical Results

The effect of a DNG slab placed next to a small dipole is studied numerically. Two small dipoles, one with total lengths of 3.1 cm and 2.1 cm are used as a near field probe. The radius of the wires used for the dipoles is 1 mm. The S_{11} of the two probes are shown in Fig. 5.6. The dipoles are radiative around 4.1 GHz and 5.6 GHz. At lower frequencies, the dipoles do not radiate and exhibit a highly capacitive input impedance, consistent with the fact that a small dipole is a source of TM mode evanescent fields. The input reactances at 1 GHz of the 3.1 cm (0.103λ) dipole and 2.1 cm (0.07λ) dipole are -619 Ω (0.257 pF) and -778 Ω (0.205 pF), respectively.

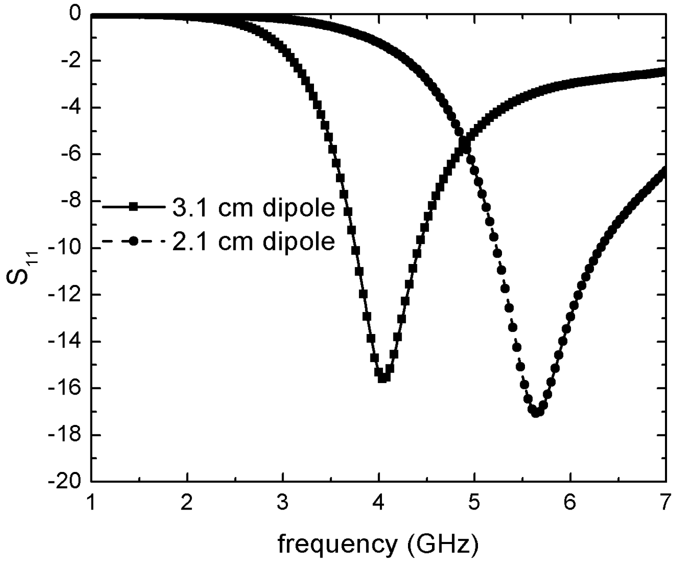

Figure 5.6: Reflection coefficients as a function of frequency. Both of the probes does not produce any significant radiation at 1 GHz. Probes are radiating at higher frequencies as expected.

The probes are placed next to a thin DNG slab as shown in Fig. 5.7. The DNG layer has an area of 15 cm × 15 cm. The operation frequency is 1 GHz, where both dipoles are capacitive and the reflection coefficients are -0.008 dB and -0.002 dB for the 3.1 cm and 2.1 cm dipoles, respectively, indicating that they are electrically small, non-radiating evanescent field sources. The phase shift due to a metallic target is analyzed. The target has a cubic shape with a side length of 1 cm ($\lambda/30$). The position of the target corresponds to the excitation location of the dipoles since the field concentration at this point is the maximum.

Fig. 5.8 shows the phase shift in the reflection coefficient of the 3.1 cm dipole as a function of the target distance. A 1 mm ($\lambda/300$) DNG layer improves the phase shift of a target located at 1 mm ($\lambda/300$) by 5.439 times. DNG layers thinner than 1 mm ($\lambda/300$) gives a smaller improvement compared to the 1 mm ($\lambda/300$) layer. DNG layers thicker than 1 mm ($\lambda/300$) gives a better sensitivity improvement for target distances larger than 2 mm ($\lambda/150$). Fig. 5.9 shows the phase shift improvement compared to the case without the DNG layer. To evaluate the improvement, phase shift values are normalized by the values generated by corresponding cases without the DNG layer. Thicker DNG results a better improvement for larger target distances.

Fig. 5.10 shows the phase shift plots in the case of a 2.1 cm dipole. The behavior is

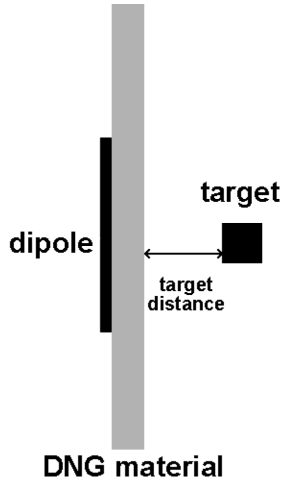

Figure 5.7: A small dipole placed next to a DNG layer is simulated. The dipole is excited with a lumped port. The target is an electrically small metallic cube.

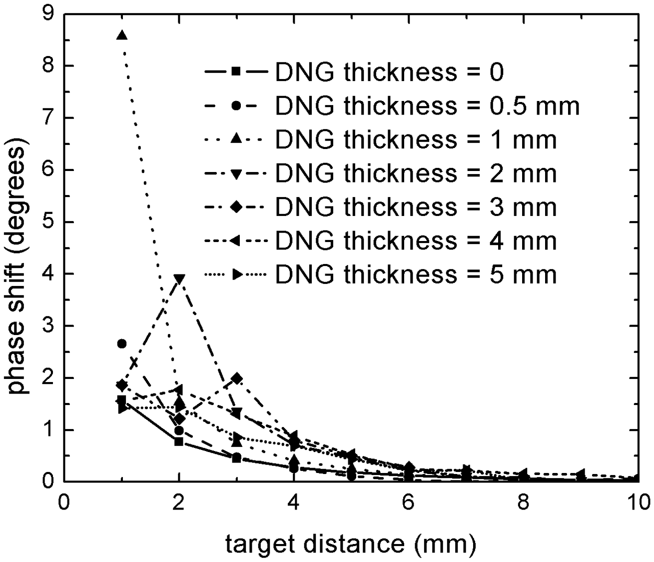

Figure 5.8: Phase shift due to the target as a function of target distance for 3.1 cm dipole, fir different DNG thicknesses. The phase shift is improved by 5.4 times compared to the case without DNG layer.

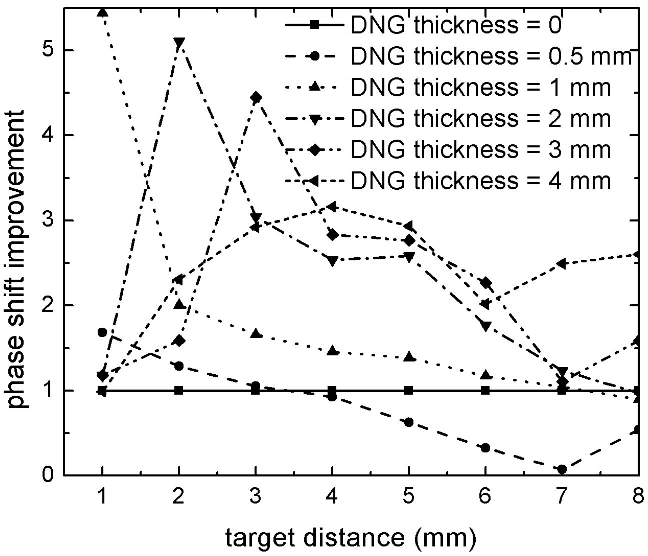

Figure 5.9: Sensitivity improvement for 3.1 cm dipole, obtained by DNG layers. Bigger DNG thicknesses gives a better improvement for target distances larger than 2 mm.

similar to behavior of the 3.1 cm dipole probe. The 2.1 cm probe has slightly smaller sensitivity compared to the 3.1 cm probe (has a 7% smaller phase shift for a 1 mm target distance, for no DNG case). Since in the small dipoles, the current is concentrated around the excitation location, a small change in the size of the dipole does not produce a big sensitivity change.

5.4 Conclusion

The effect of using DNG materials on the sensitivity of electrically small dipoles is studied theoretically and numerically. The theoretical study is extended to spherical coordinates by solving the field distribution due to a small dipole placed at the center of concentric spherical shells. It is theoretically shown that placing a spherical DNG shell improves the sensitivity of electrically small dipoles.

Numerical analysis are conducted for a small dipole placed next to a DNG layer. Phase shift in the reflection coefficient of the dipole due to an electrically small metallic target is analyzed. By using DNG layers, the phase shift is improved more than 5 times, compared to the case without DNG layer.

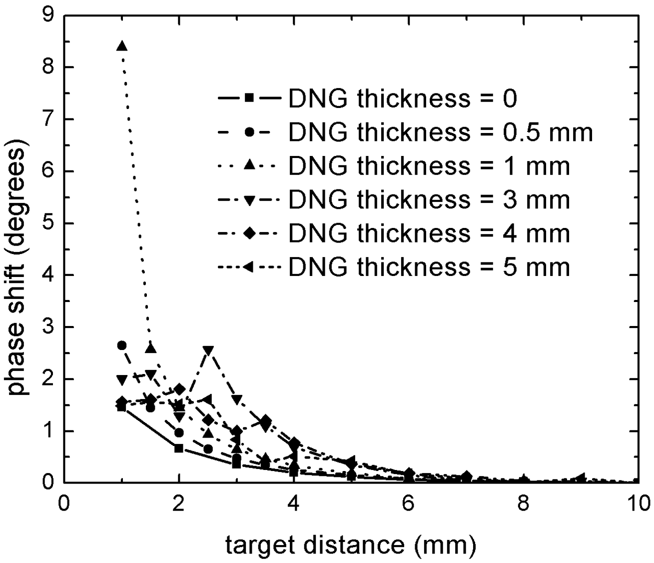

Figure 5.10: The sensitivity improvement is also valid for the smaller dipole. The phase shift levels and the dependencies on the target distance and DNG thickness are similar to the behavior of the other dipole.

Chapter 6

Experimental Verification and Application to Electrically Small Loops

Experimental results showing the sensitivity improvement in near field probes using negative materials are presented in this chapter. The amplifying medium is selectrd to be a μ-negative SNG material. The sensitivity of an electrically small loop is studied experimentally and numerically.

6.1 Introduction

Since the method of designing ϵ [24] and μ [25] negative metamaterials, and the theory of evanescent field amplification [5] were published, experimental studies have been conducted to realize such materials and support the theory. Designs based on metallic inclusions and transmission line structures were proposed and successfully experimented in the literature.

The realization of double negative materials using metallic inclusions can be considered in two parts. The first part is the production of engineered materials with negative permittivity. The second part is the fabrication of magnetic materials with negative permeability by using split ring resonators (SRRs). Therefore ϵ-negative and μ-negative SNG materials can be realized. DNG metamaterials are realized by employing the inclusions designed for μ-negative and ϵ-negative SNG responses in the same medium simultaneously.

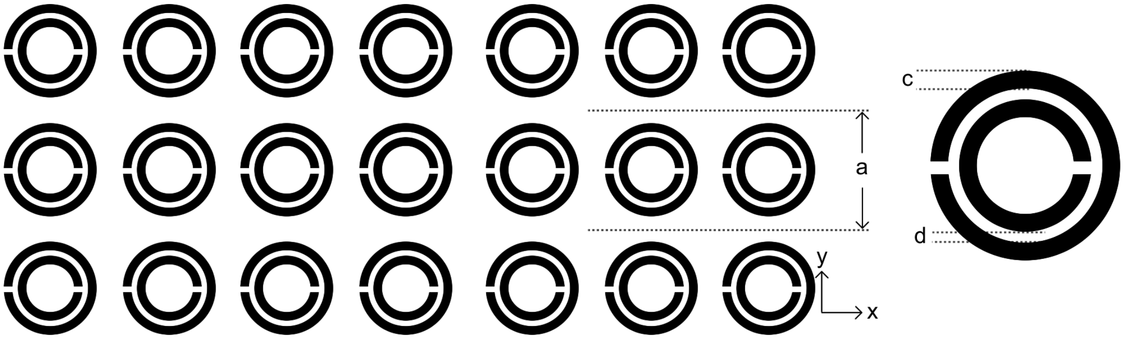

Figure 6.1: Periodic split ring resonators. Note that the structure is also periodic in the $\hat{z}$-direction. Around the resonance frequency, a magnetic field oriented along $\hat{z}$-direction experiences the magnetic effect.

Negative permittivity was an observable phenomenon before the metamaterials. Some metals, such as silver, have a negative permittivity at optical frequencies, but there is no natural material that exhibits negative permittivity at lower frequencies. In 1996, Pendry proposed a method that can support plasmon excitations at fairly low frequencies [24]. It was shown that when very thin wires of conductors are periodically placed into a dielectric medium, the structure results a well defined plasmonic behavior at very low frequencies. In his example, by placing 1 μm radius aluminum wires with a period of 5 mm, a plasma frequency of 8.2 GHz was achieved. The effective permittivity of such a structure is given as

$$\epsilon_{eff} = 1 - \frac{\omega_p^2}{\omega(\omega + i\epsilon_0 a^2 \omega_p^2/\pi r^2 \sigma)} \tag{6.1}$$

where σ is the conductivity of the wires, r is the radius of the wires and a is the spacing between the wires. Calculation of ω_p, the plasma frequency, using effective mass and electron density can be found in Ref. [24]. This structure was tested experimentally in Ref. [92].

The second part is producing magnetically active materials in the microwave frequencies. In Ref. [25], split ring resonators were proposed to achieve magnetic materials in the microwave range. Since there is no magnetic current in the nature, it is not possible to design an analogy of low frequency electrical plasma for the magnetic case. Instead, a resonant structure as shown in Fig. 6.1 was used to obtain negative permeability. The lattice constant, a, is smaller than the wavelength, and the ring radius must be in the order of lattice constant in order to achieve the desired characteristics. The effective permeability of such a structure is given by

$$\mu_{eff} = 1 - \frac{\pi r^2/a^2}{1 + j\frac{2l\rho}{\omega r \mu_0} - \frac{3lc_0^2}{\pi\omega^2 r^3 \ln 2c/d}}, \tag{6.2}$$

where r is the inner radius of the smaller ring, l is the periodicity along $\hat{z}$-direction, ρ is the resistance per unit length, and other parameters are defined in Fig. 6.1. In addition to the split ring resonator structure, different geometries were proposed in order to reduce the loss or dimensions of the inclusions [93–95]. All structures share the same fundamental idea of creating an electrically small resonant structure that is activated by the magnetic field.

In addition to the metallic inclusion based designs, transmission line based DNG materials were proposed in Refs. [96, 97]. Different than the metallic inclusion based materials, L-C loaded transmission lines does not use the resonance, instead, appropriate phase differences are added to achieve a negative propagation. The advantage of this method is the opportunity of producing low loss materials, since the idea behind is not based on resonance.

Regular transmission lines are modeled by a series inductor and a parallel capacitor, if the line is lossless. This structure provides a positive phase propagation. On the other hand, if there were a transmission line such that there is a series capacitor and parallel inductor, the wave solution would lead to a negative phase propagation. Since it is not possible to change the characteristics of transmission lines, Eleftheriades and his group proposed adding lumped series capacitors and parallel inductors periodically to the transmission line.

Using the material design methods described above, number of experiments were reported to explore the extraordinary properties of negative materials. Evanescent field amplification have been experimentally observed by placing SNG and DNG materials in a waveguide operating in the cutoff regime [28, 29]. In addition, experimental studies for exploring the perfect lens phenomenon, which is a consequence of evanescent field amplification, were presented using split ring resonators [30, 98] and transmission line structures [31].

Although images of sources with subwavelength resolution have been obtained experimentally, experimental study of the sensitivity improvement of near field probes has not been reported. In this chapter experimental and numerical results showing the improvement in the sensitivity of an electrically small loop are presented. A μ-negative SNG medium is used as the amplifying medium. An artificial magnetic material composed of split ring resonators is designed and fabricated to realize the SNG medium.

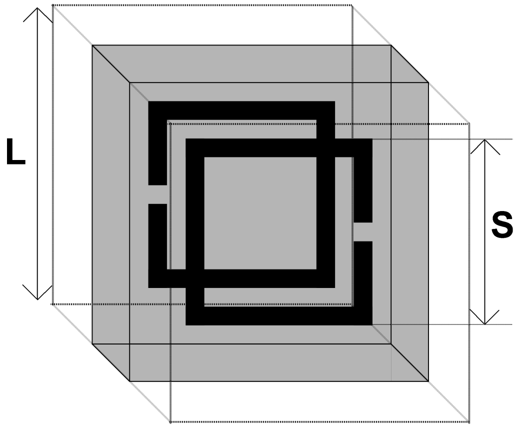

Figure 6.2: The unit cell of a single MSRR.

6.2 SNG Material Design and Fabrication

6.2.1 Design

Modified split ring resonators (MSRRs) as proposed in Ref. [27] are designed to realize μ-negative medium. The structure is composed of two split rings located at the two side of the substrate as shown in Fig. 6.2. The analytical relations between the dimensions of the unit cell and the effective medium parameters can be found in Ref. [99].

Fig. 6.3(a) shows the dimensions of the designed structure. Note that the analytical relations given in Ref. [99] assumes that the space is filled with the same material as the substrate material. However, in our design the space is vacuum, whereas the substrate is a low loss dielectric material. The unit cell is 16 mm with a trace width of 1 mm. A substrate thickness of 0.762 mm is used. The substrate material is Rogers 4350 with a relative permittivity of 3.48 ± 0.05 and a loss tangent of $\tan\delta = 0.0031$. The fabricated strips are shown in Fig. 6.3(b). Printed circuit board manufacturing techniques are used for the fabrication.

6.2.2 Numerical Characterization

The effective parameters of the designed structure are extracted using Ansoft HFSS. The unit cell is placed in an artificial parallel plate waveguide. The boundary conditions of the waveguide are selected to achieve an incident TEM wave with a magnetic field perpendicular to the MSRR plane. The sides parallel to the MSRR plane are assigned as perfect electric conductor and the sides perpendicular to the MSRR plane are assigned as perfect electric conductor. Therefore a structure that mimics a TEM wave normally

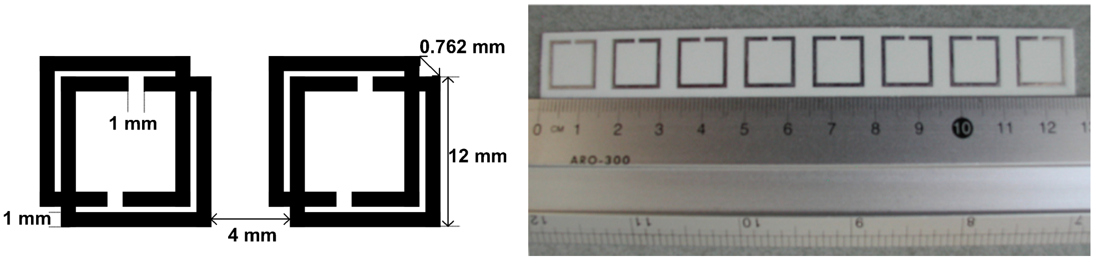

(a) (b)

Figure 6.3: (a) Dimensions of the designed MSRR inclusions. (b) Picture of the fabricated MSRR structure. Each strip includes 8 MSRR pairs.

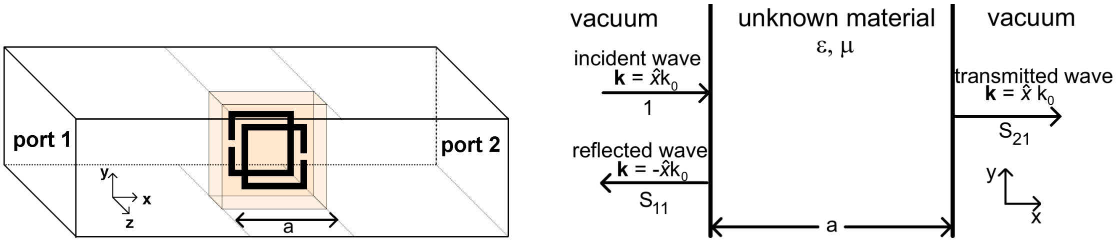

(a) (b)

Figure 6.4: (a) The simulated waveguide structures with a single unit cell at the center. The boundaries in the xy plane are assigned as perfect magnetic conductor and boundaries in the xz plane are perfect electric conductor. (b) The equivalent effective medium model of the waveguide structure. The unknown material is assumed to be infinite in $\hat{y}$ and $\hat{z}$ directions.

incident on an infinite metamaterial layer with a thickness equal to a single unit cell is simulated (see Fig. 6.4(a)). By measuring the reflection and transmission coefficients, the effective parameters are extracted using the method presented in Ref. [100].

When there is a normally incident plane wave on a dielectric layer with a thickness of a, the measured reflection and transmission coefficients can be used to calculate the characteristic impedance, Z, and refractive index, n [100–102]. Considering the structure in Fig. 6.4(b)

$$Z = \pm\sqrt{\frac{(1+S_{11})^2 - S_{21}^2}{(1-S_{11})^2 - S_{21}^2}} \tag{6.3}$$

$$e^{jnk_0a} = \frac{1}{2S_{21}(1-S_{11}^2+S_{21}^2)} \pm j\sqrt{1-\left[\frac{1}{2S_{21}(1-S_{11}^2+S_{21}^2)}\right]^2}, \tag{6.4}$$

can be found, where $Z = \sqrt{\frac{\mu}{\epsilon}}$ and $n = \sqrt{\mu\epsilon}$.

Fig. 6.6 shows the extracted material properties as a function of frequency. The

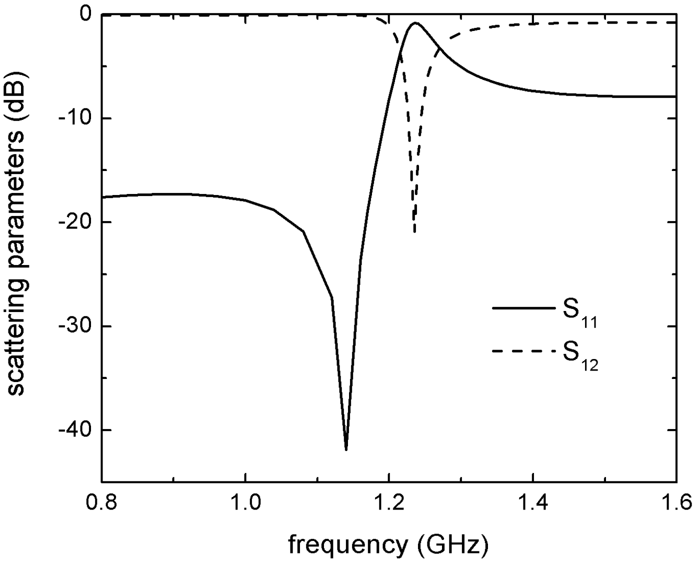

Figure 6.5: The scattering parameters of the structure described in Fig. 6.4(a), computed by HFSS.

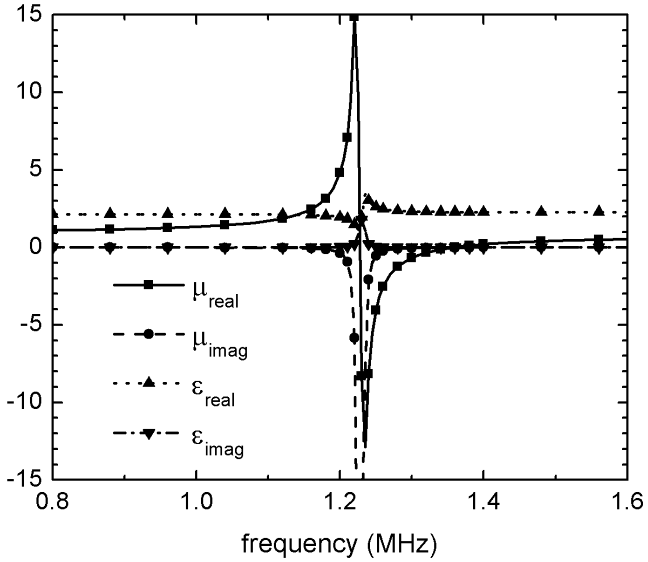

Figure 6.6: Effective medium parameters generated by HFSS. Reflection and transmission coefficients from an infinite layer composed of periodic MSRR structures are used to extract the parameters.

structure resonates at 1225 MHz. The medium behaves as a μ-negative medium from the resonance frequency to 1360 MHz. In this frequency interval, the effective ϵ changes between 3 and 2.3. Since the imaginary part of the effective μ is very high around the resonance frequency, the sensitivity improvement is expected at higher frequencies. The size of the MSRR loops corresponds to 0.048λ, where λ is the free space wavelength at 1.2 GHz.

6.2.3 Experimental Verification

The structure shown in Fig. 6.7 is fabricated to verify the effective parameters. The structure is a shorted microstripline, with a substrate made of the fabricated materials. A holder made of PVC is used to maintain a constant separation of 16 mm between the strips. The structure is excited with an SMA connector. The same structure is simulated using HFSS, as shown in Fig. 6.7, by employing the effective medium parameters presented in Fig. 6.6. The amplitude and phase of the reflection coefficient as a function of frequency are compared in Figs. 6.8 and 6.9, respectively. Experimental and numerical results give very similar results, confirming the effective medium parameters.

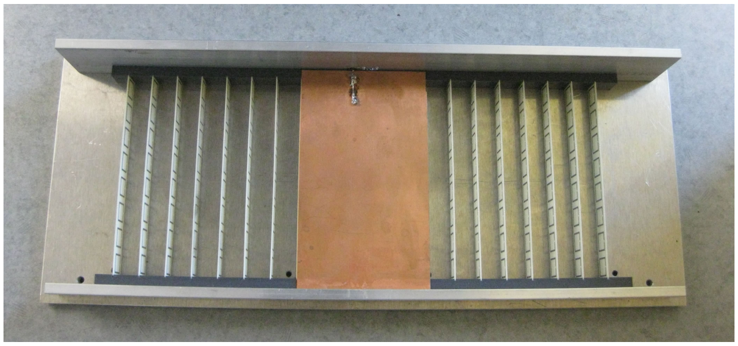

(a)

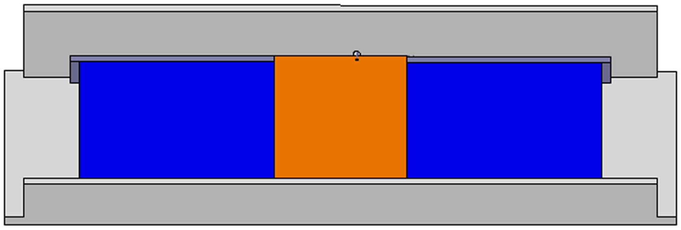

(b)

Figure 6.7: (a) Photograph of the characterization setup. The fabricated strips are placed under a shorted microstripline and the reflection coefficient is measured using a VNA. (b) The structure simulated by using HFSS. Effective medium parameters are used for the substrate.

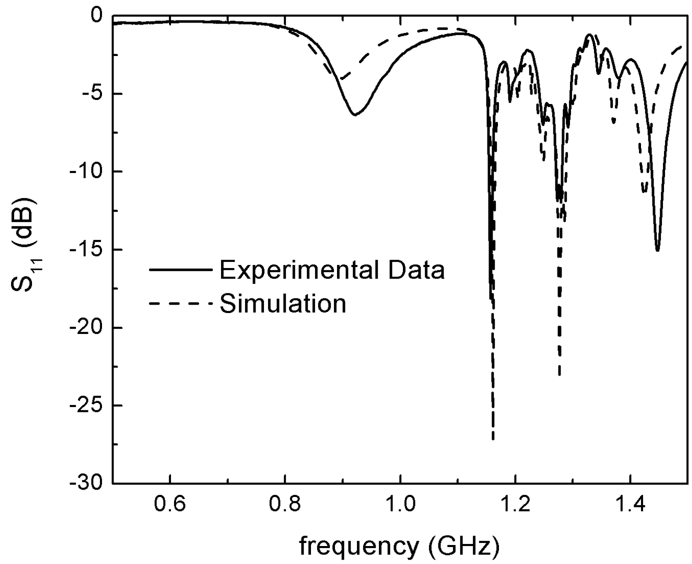

Figure 6.8: Magnitude of the reflection coefficient obtained by the experiment and the simulation. The structure is presented in Fig. 6.7

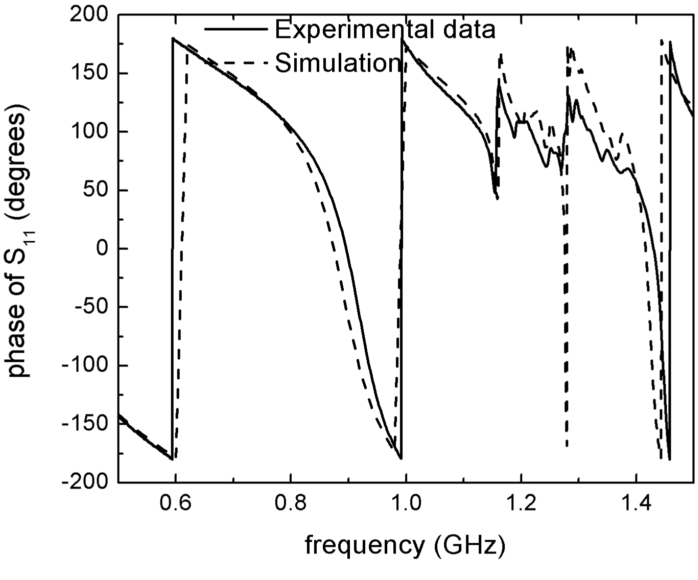

Figure 6.9: Phase of the reflection coefficient obtained by the experiment and the simulation. The structure is presented in Fig. 6.7

6.3 Numerical Results

An electrically small loop made of copper with a radius of 15 mm and a thickness of 1 mm is simulated to study the effect of SNG material. The frequency response of the loop is shown in Fig. 6.10. The loop is an efficient radiator around 3.4 GHz, which is close to the resonance frequency of the loop of 3.18 GHz. Around 1.2 GHz, the frequency at which the designed material has negative permeability, the reflection coefficient is larger than -0.1 dB and the input impedance of the loop is highly inductive. Therefore, at the frequency of 1.2 GHz, the loop behaves as an electrically small, non-radiating TE mode evanescent field generator.

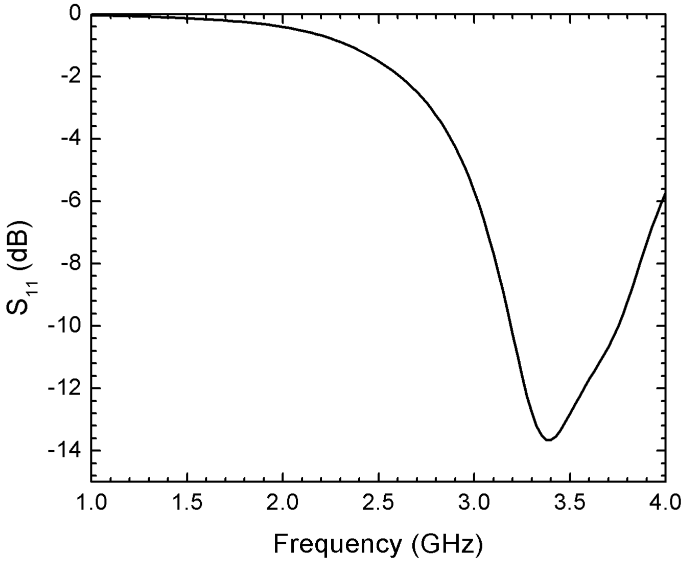

Figure 6.10: The reflection coefficient of the probe as a function of frequency. Around the resonance frequency of the inclusions, the loop does not generate any significant electromagnetic radiation. The input impedance is inductive, meaning that the near field is dominated by the H field.

The reflection coefficient of the probe is studied for the cases shown in Fig. 6.11. The frequency dependent material properties shown in Fig. 6.6 are used for the simulation of the SNG medium. Simulations are conducted for target distances, d, of 1 mm (0.004λ, where λ is the free space wavelength at 1.2 GHz), 10 mm (0.04λ) and 20 mm (0.08λ).

Fig. 6.12 shows the phase of the reflection coefficients for the structures shown in Figs. 6.11 (a) and (b). The SNG layer thickness is 10 mm and the target size is 40 mm. When there is no SNG layer, the phase of the S_{11} is monotonically decreasing. On the

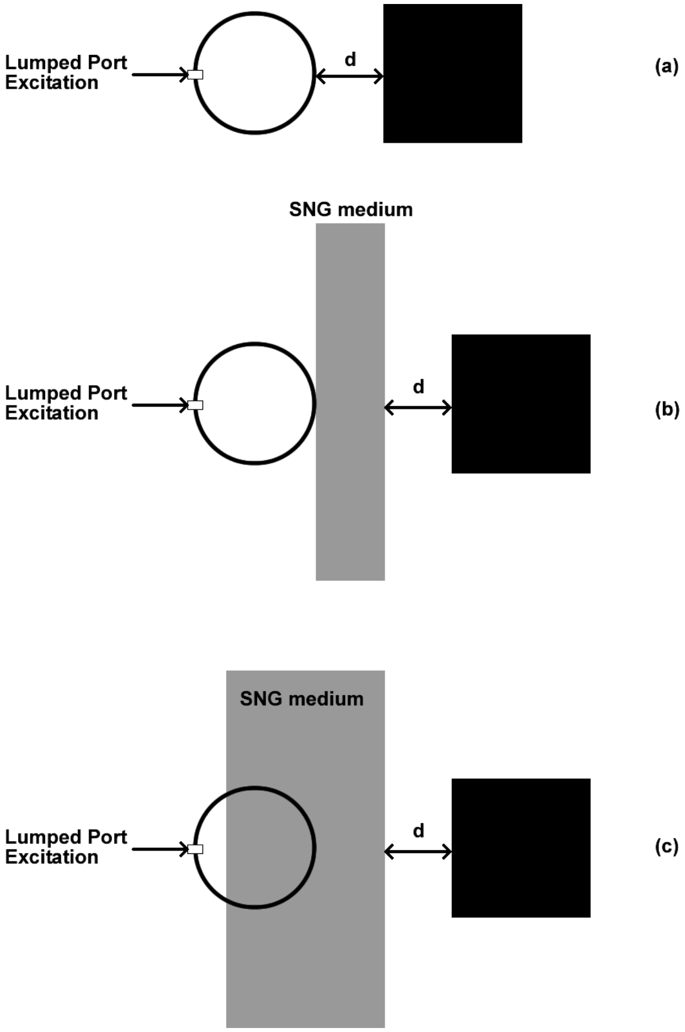

Figure 6.11: The sensitivity characteristics of three probe configuration are studied. (a) shows the conventional use of a probe. (b) and (c) are two configurations employing the SNG material. When the physical structure of the SNG medium is considered, i.e. the MSRR structures, configuration in (c) can couple the electromagnetic field to the SNG medium easier compared to the configuration in (b). The thickness of the SNG mediums are 10 mm and 48 mm in (b) and (c), respectively. The area of the SNG layers is 128 mm × 128 mm.

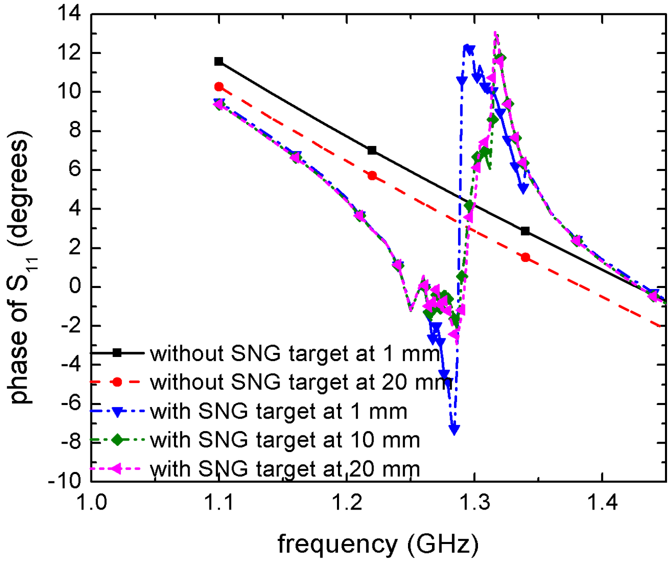

Figure 6.12: The phase of the reflection coefficient for the cases shown in Figs. 6.11 (a) and (b). The magnetic material is active between 1.2 GHz and 1.35 GHz. Since the material does not have any magnetic response around 1.1 GHz, the reflection phases with and without the SNG layer are close to each other at 1.1 GHz.

other hand, with the SNG layer, the effect of the magnetic material leads to a dramatic change in the phase from 1.2 GHz to 1.4 GHz. When the frequency is not close to the resonance frequency, the reflection phase approaches that of the case of no SNG layer with a target distance of 10 mm. The difference observed between the two cases at 1.1 GHz is attributed to the fact that the effective relative permittivity of the artificial medium is not equal to 1.

Fig. 6.13 shows the phase shift due to the target when the target is 1 mm away, for the cases presented in Figs. 6.12 (a) and (b). The phase shift due to the target is calculated by subtracting the reflection phase when $d = 1$ mm from the reflection phase when $d = 20$ mm. When there is no SNG layer, the phase shift slightly increases as the frequency increases. The phase shift changes from 1.29° to 1.53°. This is expected since the wavelength reduces as the frequency increases. As a consequence, the target and the probe become electrically larger, resulting in a higher sensitivity.

When the metamaterial slab is introduced, the phase shift is improved in the frequency range of 1.267 GHz - 1.328 GHz. In this interval, the real part of the relative permeability of the slab changes between -2.5 to -0.25. As expected, at the frequencies where the material is double positive and around the resonance frequency where the imaginary part

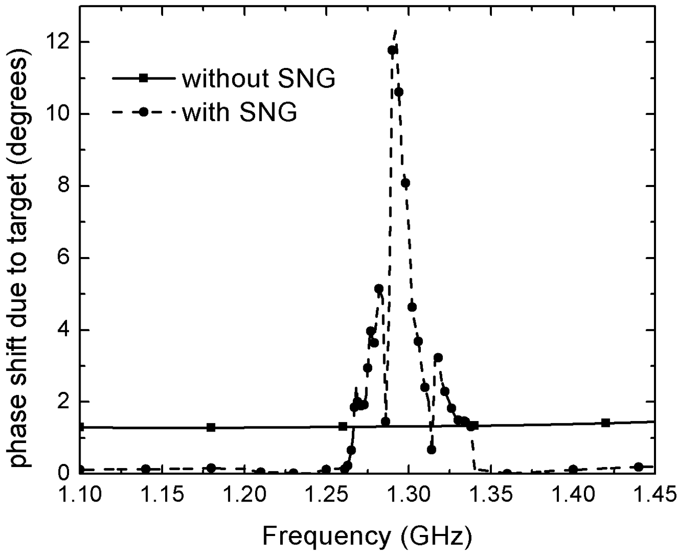

Figure 6.13: The difference between the reflection coefficients when the target distance is 1 mm 0.004λ and when the target distance is 20 mm 0.08λ for the configurations shown in Figs 6.11 (a) and (b). The phase shift is improved from 1.32° to 12.31° at 1.292 GHz

of the permeability is very high, the sensitivity is reduced. The maximum phase shift is observed at 1.292 GHz with a relative permeability of $\mu_r = -0.91 - \jmath 0.06$. The phase shift is improved by 9.3 times compared to the case without the SNG medium.

Fig. 6.14 shows the effect of the SNG layer and the target on the **H**-field distribution. The change in the position of the target does not result in a significant change in the field distribution when the SNG layer is not used. On the other hand, when the SNG layer is present in the structure, the target perturbs the field distribution within the SNG layer. Although in earlier work [23] (Chapter 2), quantitative results showed the pronounced change in energy distribution around the target due to the presence of the SNG medium, Fig. 6.14 show qualitatively the same conclusion but for a physical real-world probe. In Fig. 6.14, the same colormap is used for all images. Note that the field distribution presented in Figs. 6.14(c) and 6.14(d) are generated at 1.292 GHz where maximum phase shift is achieved.

The reflection phase plot and the phase shift due to the target plot for the case shown in Fig. 6.11 (c) are presented in Figs. 6.15 and 6.16, respectively. Similar improvements in the phase shift are observed in this case as well. The frequency band over which the sensitivity is improved is narrower compared to the previous case. Within the improvement band of 1.267 GHz - 1.278 GHz, the relative permeability is between -2.5 and -1.25.

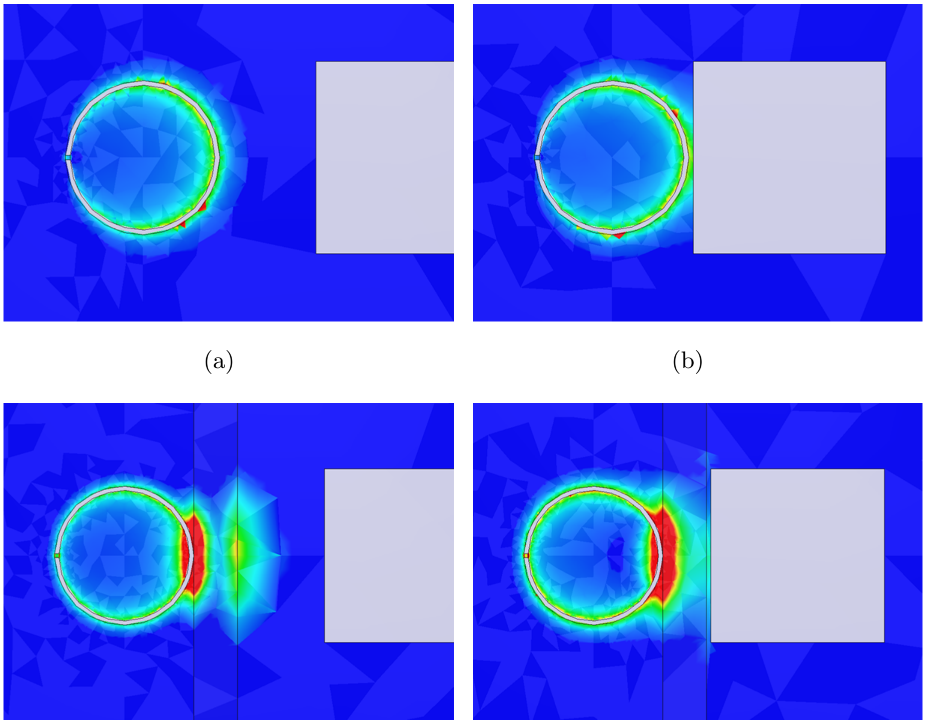

(a)

(b)

(c)

(d)

Figure 6.14: Effect of the target position on the **H**-field distribution. Structures in (a) and (b) does not have any SNG layer. (c) and (d) show the case with the SNG layer, at the frequency where maximum sensitivity is achieved in Fig. 6.13, 1.292 GHz. In (b), target changes the field distribution around it only. (d) shows that the target changes the field distribution in the SNG layer.

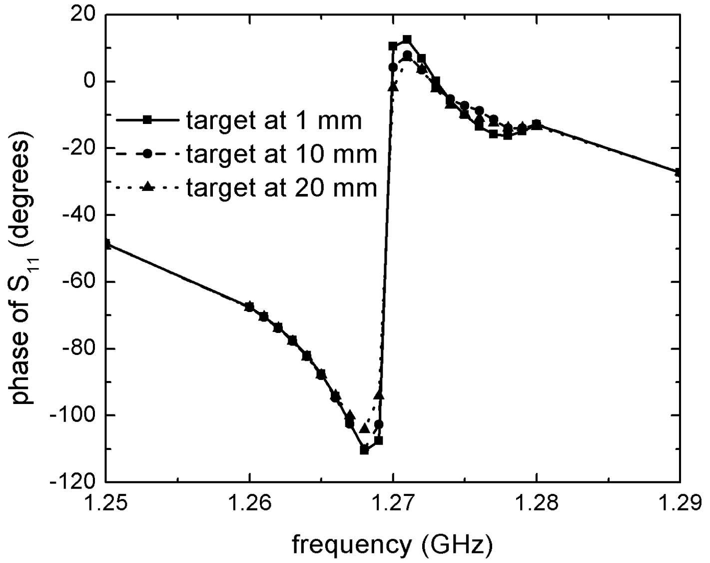

Figure 6.15: The phase of the reflection coefficient for the case shown in Figs. 6.11 (c).

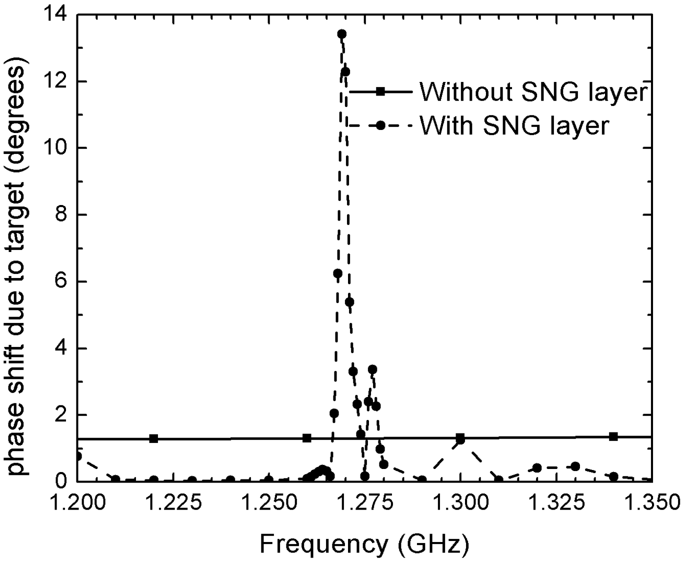

Figure 6.16: The difference between the reflection coefficients when the target distance is 1 mm 0.004λ and when the target distance is 20 mm 0.08λ for the configurations shown in Figs 6.11 (a) and (c). The phase shift is improved from 1.31° to 13.41° at 1.269 GHz

The phase shift is improved by 10.2 times compared to the case without the SNG layer.

6.4 Experimental Results

6.4.1 Experimental Setup

The experimental setup consists of three major components. The first component is the electrically small loop [103]. The radius of the loop is 15 mm 0.06λ, which is equal to, same as the simulated probe. Therefore the loop behaves as a small non-radiating evanescent TE wave generator. The probe is connected to a vector network analyzer by an SMA connector as shown in Fig. 6.17(a).

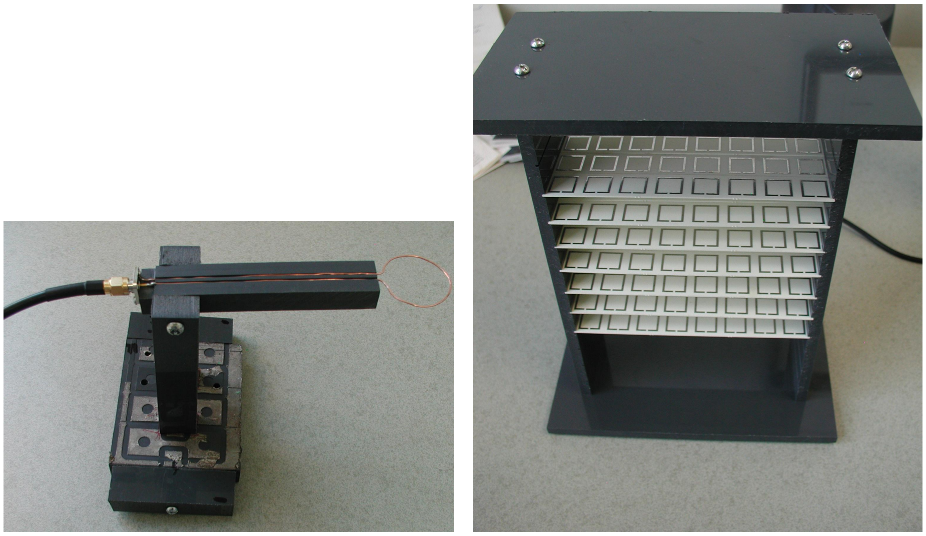

(a) (b)

Figure 6.17: (a) The electrically small loop. (b) The metamaterial region. The separation between the strips is 16 mm

The second component consists of the metameterial inclusions and the strip holder. Since the effective medium parameters are sensitive to the periodicity of the structure, it is crucial to maintain the separation between the strips as designed in Section 6.2 . As shown in Fig. 6.17(b), the holder has 3 × 7 strips.

The last component is the target. The position of the target in the $\hat{z}$-direction is selected so that the center of the target faces the probe. Two cubic targets, one with a side length of 20 mm (0.08λ) and the other with a side length of 40 mm (0.16λ), are used. The targets are made of aluminum.

The position of the target is defined by two parameters. The *target distance* represent the separation between the probe and the target if there is no metamaterial layer. Otherwise it corresponds to the separation between the metamaterial layer and the target. The second parameter, the *target location*, represents the misalignment between the probe and the target. The position in $\hat{z}$-direction is kept constant for all measurements.

All the fixtures are fabricated using polyvinyl chloride (PVC). The material is non-magnetic with a relative permittivity of 2.38 [104].

The complete setup is presented in Fig. 6.18. The loop is placed inside the metamaterial region, touching the middle strip layer, to couple more energy to the MSRRs. Therefore, although the total thickness of the metamaterial region is equal to 48 mm, the thickness of the layer between the target and the probe is less than half of its total thickness. In addition, the response of the probe is very sensitive to the relative location of the loop with respect to the MSRR alignments. This shows that individual resonances of MSRRs affect the response.

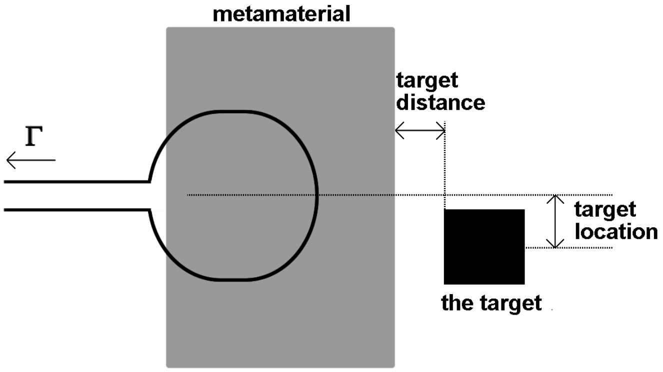

Figure 6.18: The position of the target is defined by two distances. The first one is the separation between the metamaterial layer and the target. The second one is the shift between the alignments of the loop and the target. Please note that when there is no metamaterial the target distance is redefined as the distance between the probe and the target.

6.5 Measurements

The sensitivity as a function of target distance is analyzed for both targets at two different frequencies in the negative μ region. The sensitivity is defined as the variation in the reflection phase due to the target movement. Therefore, the phase shift corresponds to the difference between the phase of the reflection coefficient when the target is at the

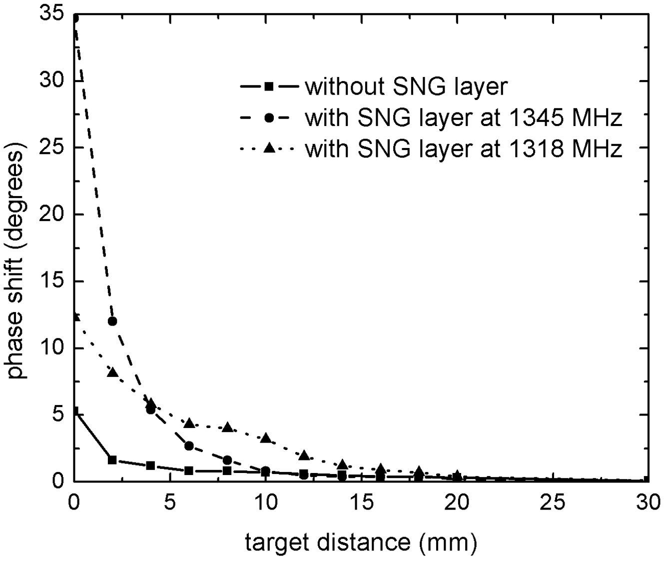

Figure 6.19: The phase shift due to a cubic target with a side length of 40 mm ($\simeq \lambda/6.12$). When the split ring resonators act as a μ-negative material, the sensitivity is improved.

corresponding location and the phase of the reflection coefficient when the target is at infinity.

Fig. 6.19 shows the sensitivity improvement for the 40 mm target. The phase shift is improved from 5° to 35° when the target distance is equal to 0. When the μ-negative material is employed, a target 5 mm away from the probe results in the same phase shift as a target touching to the probe without the metamaterial. Therefore the range is increased using the SNG layer.

Fig. 6.20 shows that the sensitivity improvement is also valid for small targets. The phase shift due to a 20 mm target at target distance equal to 0 is improved to 18°, compared to the classical case with 2.1° phase shift. For all data points presented in Figs. 6.19 and 6.20, the target location is equal to 0.

In addition to the sensitivity measurements as a function of target distance, 1D images are produced by varying the target location. 1D images generated for 20 mm target with and without metamaterial are presented in Fig. 6.21. The images show that although the metamaterial layer improves the sensitivity appreciably, the image quality is slightly distorted. To analyze the image quality, the width of the image is defined as the width where the phase shift is reduced to $1/\sqrt{2}$ times the maximum phase shift. The image width is 31 mm when the metamaterial is used. On the other hand, the case without the

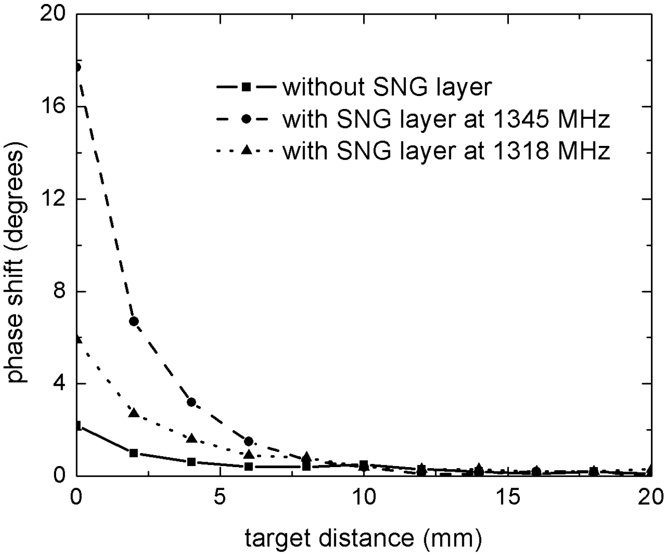

Figure 6.20: The phase shift due to a cubic target with a side length of 20 mm ($\simeq \lambda/12.2$). The sensitivity improvement is also valid for a small target. The phase shift is reduced by a factor of 2 compared to the bigger target.

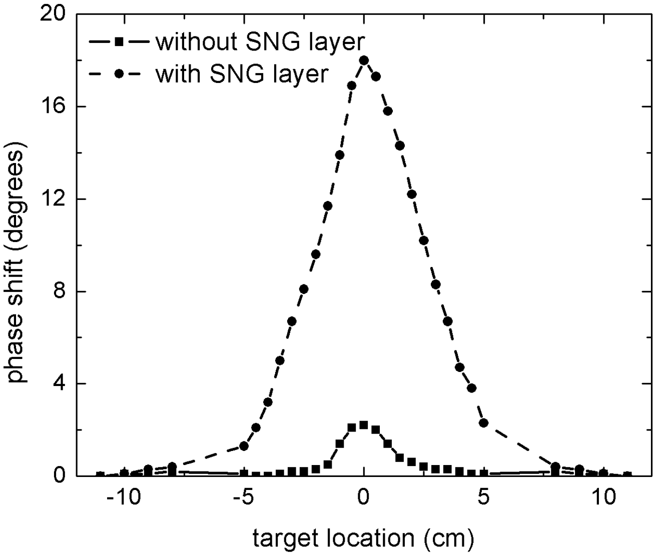

Figure 6.21: 1D images of the 20 mm target. Images are generated at 1345 MHz by changing the target location while keeping target distance.

metamaterial produces an image width of 19 mm.

6.6 Conclusion

The effect of using μ-negative metamaterial on a near field probe is studied numerically and experimentally. Modified split ring resonators are designed and fabricated to obtain an effective μ-negative material. The numerical studies show that up to 10.2 times improvement in the phase shift can be obtained by employing the designed metamaterial within the frequency range where the material has a negative permeability. Experimental validation of the design was performed using fabricated resonators and a small circular loop made of copper. Measurements showed that the sensitivity of the small probe considered here can be increased by up to 9 times by employing a metamaterial layer in comparison to the case without μ-negative metamaterial. The sensitivity improvement was demonstrated for $\lambda/6.12$ and $\lambda/12.2$ sided cubic aluminum targets.

Chapter 7

Conclusion

7.1 Contributions

7.1.1 Theoretical Analysis

In this thesis, effect of using negative materials on the near field probe sensitivity is analyzed. A theoretical sensitivity definition is proposed based on the change in the reactive energy stored around the probe. Plane wave analysis of adding a planar negative material between a probe and a target showed that the sensitivity of a probe can be enhanced considerably. The enhancement can be used to increase the range of probes or to detect smaller objects.

Both SNG and DNG materials enhance the sensitivity. While the enhancement obtained by SNG materials have additional limitations compared to DNG materials, SNG materials are easier to realize and, if used in an appropriate configuration, they have potential of being more effective than the DNG materials.

The spectrum analysis of lossless matched DNG layers shows that the sensitivity enhancement is valid for the whole evanescent spectrum. Therefore the sensitivity of any near field probe can be increased by employing an ideal DNG layer. In practical applications, DNG materials are lossy and it is extremely challenging to realize an exactly matched material. Having a lossy DNG layer results a degradation in the sensitivity enhancement. The degradation is more effective in the evanescent spectrum with higher spatial frequency. Therefore smaller probes are expected to suffer more from electromagnetic loss of the material. When the DNG layer is not matched, the amplification process can be only observed within a limited evanescent spectrum range.

The SNG materials exhibit a spectrum response similar to the response of the unmatched DNG materials. The enhancement is limited to an evanescent spectrum range. Since the SNG materials usually have smaller electromagnetic loss, SNG materials are advantageous for sensitivity enhancement purposes, in comparison to unmatched DNG layers.

In addition to the plane wave analysis, the sensitivity of an electrically small dipole placed within a spherical DNG shell is investigated. The change on the antenna parameters as a function of target distance is analyzed. When a DNG layer is employed, the position of the target results a higher change in the antenna parameters.

7.1.2 Numerical Analysis

Sensitivity of the following structures are analyzed numerically using HFSS. The sensitivity is defined as the change in the phase of the reflection coefficient due to the presence of the target.

- **Waveguide Structures:** μ-negative SNG layers are implemented to crack detection schemes. Two cases are studied. First one is adding an SNG layer to the opening of the waveguide, outside the waveguide. The phase shift due to a $\lambda/10$ crack on an aluminum surface is enhanced by 35 times by optimizing the standoff distance and SNG layer thickness. The SNG layer both increases the sensitivity of the open-ended waveguide and quality of the image simultaneously. The second case is using a dielectric loaded waveguide with an SNG region added right before the opening of the waveguide (SNG is inside the waveguide). Similar improvements are obtained by changing the SNG thickness and standoff distance. Since the second case employs the SNG layer within the waveguide, it is a more compact design and a smaller SNG region is needed.
- **Coaxial line Structures:** ϵ-negative SNG layers are used to increase the sensitivity of open-ended coaxial lines. Phase shift due to a $\lambda/20$ crack on an aluminum surface is studied. The phase shift is improved by 11 times by using appropriate SNG thickness and standoff distance for a coaxial line with an inner radius of $\lambda/20$. When a bigger coaxial line is used, the phase shift due to the same target reduces. The improvement is analyzed for coaxial lines with dielectric constants ranging from 1 to 5. For all geometries and dielectrics, a characteristic impedance of 50 Ω is maintained.

- **Small Dipoles:** Electrically small dipole with lengths of $\lambda/15$ and $\lambda/10$ are investigated as near field probes. The phase shift due to a $\lambda/20$ sized, metallic, cubic target is analyzed with different DNG layer thicknesses. 5.4 times improvement is achieved by a DNG layer with $\lambda/30$ thickness.
- **Small Loops:** An electrically small loop is analyzed and its sensitivity is improved by using a μ-negative SNG material. Effective permeability and permittivity of an experimentally realizable SNG medium is used as the amplifying region. The sensitivity is improved by 9.3 times within the frequency band where the material exhibits negative permeability.

7.1.3 Experimental Analysis

The sensitivity of an electrically small loop is studied experimentally. A μ-negative SNG material, composed of MSRR inclusions is designed and fabricated. The fabricated SNG medium increased the sensitivity of the electrically small loop. The sensitivity due to two targets, one with a size of $\lambda/6.12$ and the other with a size of $\lambda/12.2$ are analyzed. The phase shift due to the presence of the target is increased from 2.1° to 18° for the small target.

7.2 Future Directions

7.2.1 Theoretical Directions

The spectrum response of adding a negative layer is studied in this thesis. In achieving the sensitivity improvement, the evanescent spectrum components present in the near field play an extremely important role, especially in the case of SNG and unmatched DNG layers. The relation between the probe geometry and emanated evanescent spectrum can be studied by decomposing the field distributions generated by probes to their fourier components. As a result probe selection or probe designs for specific negative materials can be formulated.

Theoretical studies can be conducted for specific problems. One example can be the formulation of an electrically small probe placed over an infinite ground plane. The small probe can be assumed as a very small dipole, and a negative spherical shell can be added around the dipole or a negative layer can be added to the surface of the infinite layer. Another study can be conducted for the open-ended coaxial line structures. The problem of a coaxial line opened to a multilayered dielectric medium can be analyzed.

The sensitivity improvement can be analyzed theoretically by replacing one of the layers by a negative layer.

7.2.2 Material Research

One of the most important limitations on the sensitivity improvement is the loss tangent of the engineered artificial materials. New inclusion geometries can be designed to reduce the electromagnetic loss of the medium or to achieve specific material properties at specific frequencies. In this sense, optimization techniques can be applied to the design process to obtain better material properties. In sensitivity improvements, the loss of the material is more important than the bandwidth of the material. Therefore goals of the optimization are not too many, making the process possible.

Another important limitation is the size of the unit cell. The unit cell of the engineered material must be smaller than the size of the target and the size of the probe. Therefore miniaturization of the unit cell is an important task for the improvement of the technique. As the unit cell gets smaller, the material is expected to behave as a homogenous negative material. As a result the effect of individual resonators can be minimized and the material can be modeled with a homogeneous material with effective permittivity and permeability. In addition, the required SNG layer thicknesses for the sensitivity enhancement is usually much smaller than the wavelength. Miniaturization can make the fabrication of very thin SNG layers possible.

7.2.3 Experimental Directions

The sensitivity improvement can be analyzed for different type of probes, and for different type of inclusions used for the material design, such as SRRs, dielectric particles, fractal hilbert curves, etc. An experimental setup and a convention can be developed to test different probes and materials under exactly same conditions.

The study can be extended to the detection of targets buried in lossy mediums. Controlled experiments for different probe types can be conducted to analyze the range improvements of the probes. Biological tissue phantoms can be used as the lossy medium material. In addition, by controlling the ingredients of the phantom, the loss tangent of the medium can be changed. Therefore the effect of the medium loss on the detectability can be analyzed.

Until this point, the artificial materials are assumed to behave as homogeneous mediums and the sensitivity improvements are discussed for homogenous materials. In addition, single electrically small resonators, meaning that one unit cell of the MSRR structures, can be used as the probe. Since resonators confine very high electromagnetic energies, these structures can be used individually to increase the field localization and the field strength. Therefore the resonators themselves can be used as the probe, rather than employing them for improving a readily available probe. The study can be extended by investigating other types of resonators. The relations between the size, shape of the probe and the sensitivity, range of the probe can be studied.

Appendix A

Field Calculations in DNG Medium

The superlensing phenomenon is based on the idea of reconstructing both evanescent and propagating waves generated by the object at the image location. Conventional lenses focuses only the propagating waves and as a result the image generated by a conventional lens has limitations on the maximum achievable resolution. On the other hand the lens proposed in Ref. [5] both focuses the propagating waves and also amplifies the evanescent fields. Therefore an image with a subwavelength resolution can be obtained.

A superlens is a slab made of DNG material. The formulation of the superlensing phenomenon is presented in this appendix.

Helmholtz equation is solved for the boundary value problem shown in Figure A.1 for a slab with ϵ_2, μ_2 and with a thickness of a. Note that the arrows shown in Figure A.1 represent the direction of the $\hat{z}$ component of the $\mathbf{k}$ vector. Therefore the arrows indicate phase propagation if the fields are propagating and indicate amplitude change if the fields are evanescent.

The sign selection in Equation 2.20 for DNG materials is the opposite of the sign that is selected for positive materials [62]. The sign selection must be consistent in order to have a correct solution. For this reason, the transmission through a slab and the field inside the slab is presented without specifying any square root sign.

Using the boundary conditions, i.e. continuity of E and H fields, for an incident E-wave with $\mathbf{k} = \hat{x}k_x + \hat{z}k_{z1}$, the coefficients described in Figure A.1 can be found as

$$t = \frac{4\mu_1\mu_2 k_{z1}k_{z2}}{(\mu_2 k_{z1} + \mu_1 k_{z2})^2 e^{j(k_{z2}-k_{z1})a} - (\mu_2 k_{z1} - \mu_1 k_{z2})^2 e^{-j(k_{z1}+k_{z2})a}} \tag{A.1}$$

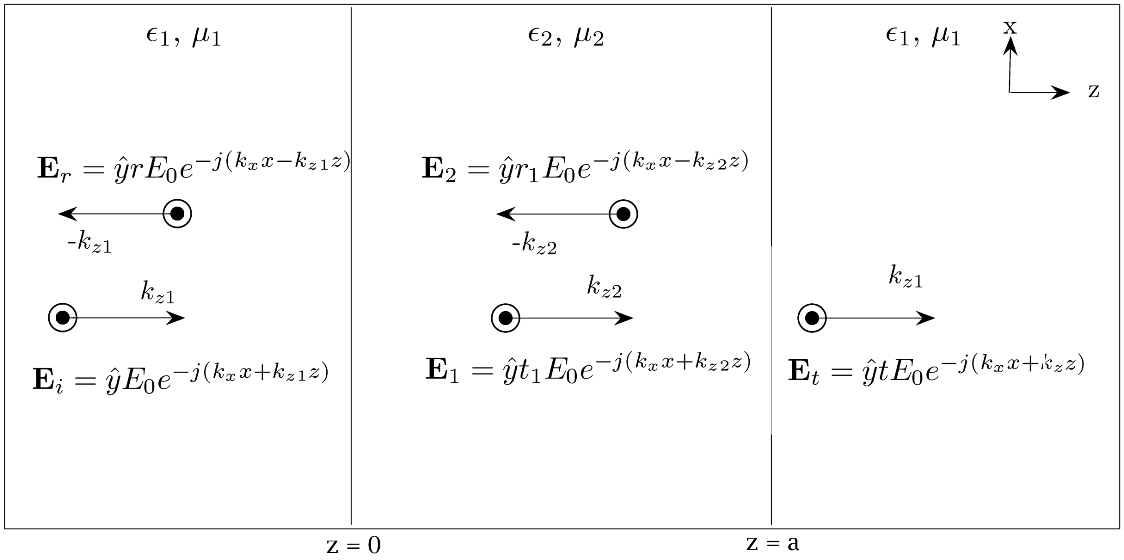

Figure A.1: Structure for the boundary condition problem solved in Equations A.1, A.2, A.3 and A.4

$$r = \frac{2\mu_2 k_{z1}[(\mu_2 k_{z1} + \mu_1 k_{z2})e^{j(k_{z2}-k_{z1})a} - (\mu_2 k_{z1} - \mu_1 k_{z2})e^{-j(k_{z1}+k_{z2})a}]}{(\mu_2 k_{z1} + \mu_1 k_{z2})^2 e^{j(k_{z2}-k_{z1})a} - (\mu_2 k_{z1} - \mu_1 k_{z2})^2 e^{-j(k_{z1}+k_{z2})a}} - 1 \tag{A.2}$$

$$t_1 = \frac{2\mu_2 k_{z1}(\mu_1 k_{z2} + \mu_2 k_{z1})e^{j(k_{z2}-k_{z1})a}}{(\mu_2 k_{z1} + \mu_1 k_{z2})^2 e^{j(k_{z2}-k_{z1})a} - (\mu_2 k_{z1} - \mu_1 k_{z2})^2 e^{-j(k_{z1}+k_{z2})a}} \tag{A.3}$$

$$r_1 \frac{2\mu_2 k_{z1}(\mu_1 k_{z2} - \mu_2 k_{z1})e^{-j(k_{z1}+k_{z2})a}}{(\mu_2 k_{z1} + \mu_1 k_{z2})^2 e^{j(k_{z2}-k_{z1})a} - (\mu_2 k_{z1} - \mu_1 k_{z2})^2 e^{-j(k_{z1}+k_{z2})a}} \tag{A.4}$$

where

$$k_{z1}^2 = \omega^2 \epsilon_1 \mu_1 - k_x^2 \tag{A.5}$$

$$k_{z2}^2 = \omega^2 \epsilon_2 \mu_2 - k_x^2. \tag{A.6}$$

This solution is valid for both evanescent and propagating waves. Sign selections in Equations A.5 and A.6 must be selected according to the values of ϵ_1, μ_1 and ϵ_2, μ_2, respectively. If one of the medium is DNG, the corresponding k_z must be selected as positive.

When the $\epsilon_1 = -\epsilon_1$ and $\mu_2 = -\mu_1$ are satisfied,

$$t{=}e^{j2k_{z1}a} \tag{A.7}$$

$$r{=}0 \tag{A.8}$$

can be found. As a result the field at $z = a$ becomes

$$\mathbf{E}_t = \hat{y} E_0 e^{-jk_x x} e^{jk_{z1}a}. \tag{A.9}$$

Therefore both the evanescent and propagating components at the plane $z = -d$ are reconstructed at $z = 2a - d$ if $0 \leq d \leq a$ is satisfied.

Appendix B

Transmission Through a Lossy Slab

The penetration of electromagnetic fields to the target medium is a challenge for noninvasive detection applications such as land mine detections or detection of biological anomalies. As a result of diffraction limit, in order to have high resolution, higher frequency is needed. But at higher frequencies, electromagnetic waves decay faster compared to lower frequencies, so the fields cannot penetrate to deeper regions. In this part, the transmission of propagating and evanescent waves through a lossy slab is presented. The transmission of normally incident propagating plane waves at higher frequencies is compared to the transmission of evanescent spectrum at lower frequencies to provide a mathematical background for using low frequency evanescent waves instead of propagating waves [105].

When a medium has a conductivity σ, the current in the medium can be expressed as $\mathbf{J} = \sigma\mathbf{E}$. Then Equation 2.9 becomes

$$\nabla^2\mathbf{E} + \omega^2\mu(\epsilon - j\frac{\sigma}{\omega})\mathbf{E} = 0 \tag{B.1}$$

and the complex permittivity, ϵ_c, is defined as

$$\epsilon_c = \epsilon - j\frac{\sigma}{\omega}. \tag{B.2}$$

The wave number k becomes

$$k^2 = \omega^2\mu\epsilon_c = \omega^2\mu\epsilon - j\omega\mu\sigma. \tag{B.3}$$

The imaginary part of k is the reason for the attenuation of electromagnetic fields in lossy mediums. As the frequency increases, the imaginary part of k increases which results in a higher attenuation.

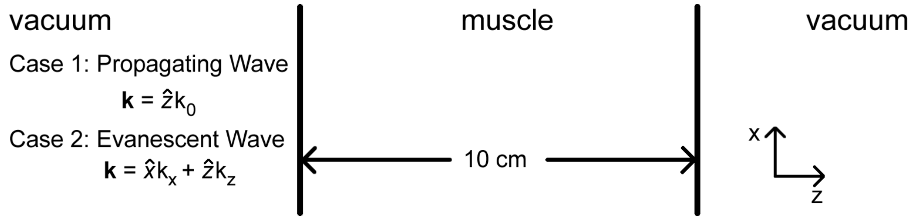

Figure B.1: In order to compare the penetration of propagating and evanescent waves into a lossy medium, the transmission through a 10 cm slab of muscle is solved for propagating waves and evanescent fields.

The analysis of the attenuation with a constant conductivity (as a function of frequency) is not complete since the conductivities of lossy media, such as human body [106, 107] and soil [108, 109], are functions of frequency. The conductivity increases dramatically in the microwave frequencies as frequency increases. For example, the conductivity of dry soil at 10 GHz is 25 times higher than the conductivity at 1 GHz or the conductivity of muscle at 10 GHz is 10 times higher than the conductivity at 100 MHz.

As an example, the transmission of propagating waves through a 10 cm muscle, labeled as Case 1 in Figure B.1, is studied for frequencies from 100 MHz to 10 GHz. A boundary condition problem that consists of vacuum - muscle - vacuum regions is solved for a normally incident plane wave. The frequency dependent complex permittivity of the muscle is calculated using [110],

$$\epsilon_c(\omega) = \epsilon_\infty + \sum_n \frac{\Delta\epsilon_n}{1 + (j\omega\tau_n)^{(1-\alpha_n)}} + \frac{\sigma_i}{j\omega\epsilon_0}. \tag{B.4}$$

The constants used in Equation B.4 are obtained from Ref. [110]. The incident field has an amplitude of 1 and a phase of 0° at the first boundary. The amplitude and phase of the field right after the second boundary are defined as the phase and amplitude of the transmission.

Figure B.2 shows the transmission. Waves with frequencies higher than 3 GHz have almost no transmission whereas lower frequencies can have around 8 % transmission.

The same problem for an incident evanescent plane wave is solved to analyze the evanescent spectrum transmission. Since vacuum-muscle and muscle-vacuum boundaries are in xy plane, the incident field is selected to decay in $+z$ direction. The **k** vector of incident field consists of $\hat{x}$ and $\hat{z}$ components as described in Equation 2.20 (see Figure B.1), and the field has an amplitude of 1 and a phase of 0° at the first boundary. The phase and magnitude of the transmitted wave are shown in Figure B.3 as a function of

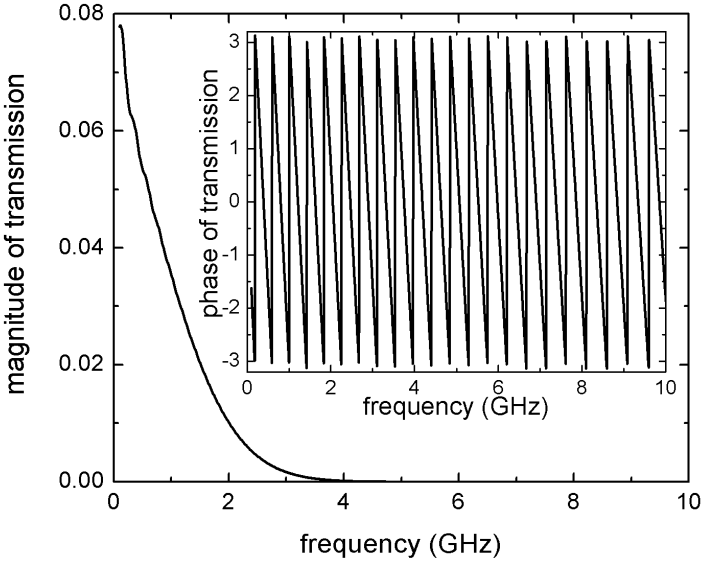

Figure B.2: Magnitude (a) and phase (b) of propagating wave transmission through a 10 cm slab of muscle as a function of frequency. The frequency changes from 100 MHz to 10 GHz. This frequency interval corresponds to an interval of free space wavelength between 3 cm to 3 m.

normalized parallel **k** component, i.e. as a function of k_x normalized to the free space wave number, k_0.

Figure B.3 shows that a wide evanescent spectrum (spatial spectrum) at 100 MHz has better transmission compared to the higher frequencies shown in Figure B.2. To put in perspective, assume that we have a 10 cm by 10 cm rectangular waveguide and there is a 10 cm muscle layer in it. The TE_{10} mode at 100 MHz, which has an evanescent behavior, has a better transmission than the TE_{10} mode at 2.1 GHz.

The attenuation of the evanescent field inside a lossy medium is a result of two mechanisms. One is the evanescence of the field, and the other is the loss of the medium. When the incident evanescent field has a low decay constant, the attenuation of the field inside the lossy medium is dominated by the loss. Thus, in this loss-dominant region, using different decay constants does not change the attenuation characteristics dramatically. The overall transmission depends on the attenuation of the field inside the slab, and the transmission and reflection coefficients at the vacuum-muscle and muscle-vacuum boundaries. Since the transmission coefficient at the boundaries increases with the decay constant of the incident field, while increasing decay constant is not changing the attenuation considerably, evanescent fields can have better transmission compared to the

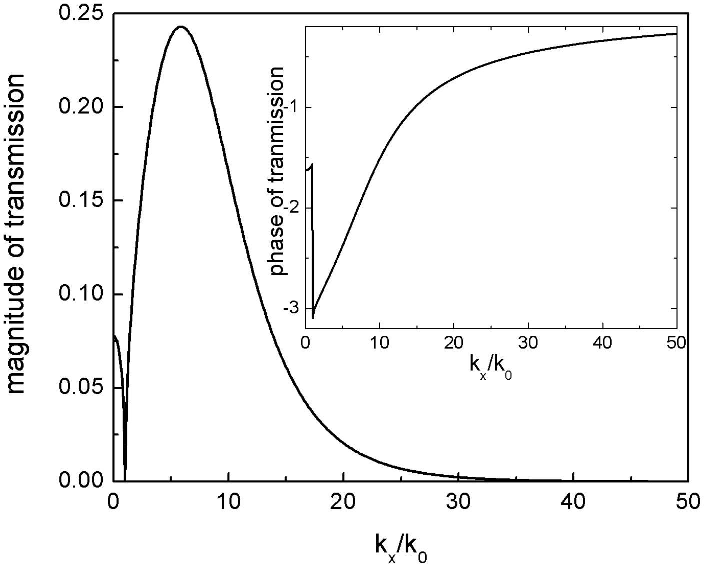

Figure B.3: Transmission of evanescent spectrum at 100 MHz through a 10 cm slab of muscle

propagating waves even if the frequency is fixed.

Appendix C

Spherical Bessel Functions

C.1 Bessel Functions

The solutions of such a differential

$$x^2\frac{d^2y}{dx^2}+x\frac{dy}{dx}+(x^2-n^2)y=0 \tag{C.1}$$

are defined as the Bessel functions. Bessel function of the first kind can be expressed as

$$J_n(x)=\sum_{m=0}^{\infty}\frac{(-1)^m}{m!\Gamma(m+n+1)}\left(\frac{x}{2}\right)^{2m+n} \tag{C.2}$$

where n can have non-integer values. Bessel function of the second kind is expressed as

$$Y_n(x)=\frac{J_n(x)\cos(n\pi)-J_{-n}(x)}{\sin(n\pi)}. \tag{C.3}$$

Note that Bessel function of the second kind has a singularity at $x=0$. In addition, Hankel functions of first and second kind are also a solution of the C.1:

$$\begin{aligned} H_n^{(1)}(x) &= J_n(x)+iY_n(x) \quad (\text{C.4})\\ H_n^{(2)}(x) &= J_n(x)-iY_n(x) \quad (\text{C.5}) \end{aligned}$$

The derivatives of all types of functions presented above can be found using

$$\frac{dF_n}{dx}=\frac{F_{n-1}(x)-F_{n+1}(x)}{2}. \tag{C.6}$$

C.2 Spherical Bessel Functions

Spherical bessel functions are the solutions of the differential equations in the form of

$$x^2\frac{d^2y}{dx^2}+2x\frac{dy}{dx}+[x^2-n(n+1)]y=0 \tag{C.7}$$

Similar to the canonical bessel functions, the solutions of the Eq. C.7 are expressed in four types, spherical bessel functions of the first kind, second kind and the spherical hankel functions of first kind and second kind. These four types of equations can be expressed in terms of the canonical bessel functions.

$$\begin{aligned} j_n(x) &= \sqrt{\frac{\pi}{2x}} J_{n+1/2}(x), && \text{(C.8)} \\ y_n(x) &= \sqrt{\frac{\pi}{2x}} Y_{n+1/2}(x) = (-1)^{n+1} \sqrt{\frac{\pi}{2x}} J_{-n-1/2}(x), && \text{(C.9)} \\ h_n^{(1)}(x) &= j_n(x) + i y_n(x), && \text{(C.10)} \\ h_n^{(2)}(x) &= j_n(x) - i y_n(x). && \text{(C.11)} \end{aligned}$$

For the results presented in Chapter 5, these relations were used. The spherical bessel functions were calculated using the MATLAB's library for canonical bessel functions.

The spherical bessel functions can be also calculated using

$$\begin{aligned} j_n(x) &= (-x)^n \left(\frac{1}{x}\frac{d}{dx}\right)^n \frac{\sin x}{x}, && \text{(C.12)} \\ y_n(x) &= -(-x)^n \left(\frac{1}{x}\frac{d}{dx}\right)^n \frac{\cos x}{x}. && \text{(C.13)} \end{aligned}$$

Therefore the functions used in Chapter 5 can be expressed as

$$\begin{aligned} j_1(x) &= \frac{\sin x}{x^2} - \frac{\cos x}{x}, && \text{(C.14)} \\ y_1(x) &= -\frac{\cos x}{x^2} - \frac{\sin x}{x}. && \text{(C.15)} \end{aligned}$$

Appendix D

MATLAB Script for Solving Fields in Multi-Shell Structures

The boundary conditions for the equations presented in Section 5.2.2 for a multilayer spherical structure are solved by using the following MATLAB script. The structure is presented in Fig. 5.1. The script calculates the unknown coefficients in Eqs. 5.9-5.17 and plots Fig. 5.3. The spherical bessel and hankel functions are calculated as described in Appendix C.

```
clear all
%% Definitions
f = 300e6; %so that lambda is 1 m
w = 2*pi*f;
e0 = 8.854e-12;
m0 = pi*4e-7;
c0 = 1/sqrt(e0*m0);
lambda = c0/f; % all other dimensions are defined in terms of free space wavelength
a = lambda/1000; %radius of the smallest circle that can enclose the dipole

% regions are defined by their material properties e(relative permittivity)
% and m (relative permeability). t defines the thickness of the
% corresponding region.

%First Sphere:
e1 = 1;   m1 = 1;   t1 = lambda/300;   k1 = w*sqrt(m1*e1)/c0;   eta1 = sqrt(m1/e1)*377;
%Second Spherical Shell:
e2 = -1;  m2 = -1;  t2 = 0.02*lambda;  k2 = -w*sqrt(m2*e2)/c0;  eta2 = sqrt(m2/e2)*377;
%Third Spherical Shell:
e3 = 1;   m3 = 1;   t3 = 1*lambda;     k3 = w*sqrt(m3*e3)/c0;   eta3 = sqrt(m3/e3)*377;
%Fourth Spherical Shell:
```

```
e4 = 1;   m4 = 1;   t4 = 1*lambda;     k4 = w*sqrt(m4*e4)/c0;   eta4 = sqrt(m4/e4)*377;
%Fifth Spherical Shell:
e5 = 1;   m5 = 1;                      k5 = w*sqrt(m5*e5)/c0    eta5 = sqrt(m5/e5)*377;

% the equations 6.9 to 6.17 will be solved by representing the correspinding
% boundary conditions by matrices. At each boundary there are two conditions,
% one for e field and the other h field. Therefore there are 8 equations.

c_matrix = zeros(8,8); % the solution will be stored in this vector.
right_hand_side = zeros(8,1);
count = 1;
sweep = t1:t1/10:10*t1;
r1 = t1;
for r2 = sweep
    r3 = r2+t3; r4 = r2+t3+t4;
%% First Boundary, r = r1
    %H field
    c_matrix(1,1) = spherical_bessel(1,1,k1*r1);
    c_matrix(1,2) = -spherical_bessel(1,1,k2*r1);
    c_matrix(1,3) = -spherical_bessel(2,1,k2*r1);
    right_hand_side(1) = -j*k1*2*a / 4/pi/r1 * (1+1/j/k1/r1) * exp(-j*k1*r1);
    %E field
    c_matrix(2,1) = (k1*r1*spherical_bessel_derivative(1,1,k1*r1)...
    + spherical_bessel(1,1,k1*r1)) / e1;
    c_matrix(2,2) = -(k2*r1*spherical_bessel_derivative(1,1,k2*r1)...
    + spherical_bessel(1,1,k2*r1)) / e2;
    c_matrix(2,3) = -(k2*r1*spherical_bessel_derivative(2,1,k2*r1)...
    + spherical_bessel(2,1,k2*r1)) / e2;
    right_hand_side(2) = (j*w*e0*r1)*j*eta1*k1*2*a /...
    4/pi/r1 * (1 + 1/j/k1/r1 - 1/(k1*r1)^2) * exp(-j*k1*r1);
%% Second Boundary, r = r2
    %H field
    c_matrix(3,2) = spherical_bessel(1,1,k2*r2);
    c_matrix(3,3) = spherical_bessel(2,1,k2*r2);
    c_matrix(3,4) = -spherical_bessel(1,1,k3*r2);
    c_matrix(3,5) = -spherical_bessel(2,1,k3*r2);
    right_hand_side(3) = 0;
    %E field
    c_matrix(4,2) = (k2*r2*spherical_bessel_derivative(1,1,k2*r2)...
    + spherical_bessel(1,1,k2*r2)) / e2;
    c_matrix(4,3) = (k2*r2*spherical_bessel_derivative(2,1,k2*r2)...
    + spherical_bessel(2,1,k2*r2)) / e2;
    c_matrix(4,4) = -(k3*r2*spherical_bessel_derivative(1,1,k3*r2)...
    + spherical_bessel(1,1,k3*r2)) / e3;
    c_matrix(4,5) = -(k3*r2*spherical_bessel_derivative(2,1,k3*r2)...
```

```
    + spherical_bessel(2,1,k3*r2)) / e3;
    right_hand_side(4) = 0;
%% Third Boundary, r = r3
    %H field
    c_matrix(5,4) = spherical_bessel(1,1,k3*r3);
    c_matrix(5,5) = spherical_bessel(2,1,k3*r3);
    c_matrix(5,6) = -spherical_bessel(1,1,k4*r3);
    c_matrix(5,7) = -spherical_bessel(2,1,k4*r3);
    right_hand_side(5) = 0;
    %E field
    c_matrix(6,4) = (k3*r3*spherical_bessel_derivative(1,1,k3*r3)...
    + spherical_bessel(1,1,k3*r3)) / e3;
    c_matrix(6,5) = (k3*r3*spherical_bessel_derivative(2,1,k3*r3)...
    + spherical_bessel(2,1,k3*r3)) / e3;
    c_matrix(6,6) = -(k4*r3*spherical_bessel_derivative(1,1,k4*r3)...
    + spherical_bessel(1,1,k4*r3)) / e4;
    c_matrix(6,7) = -(k4*r3*spherical_bessel_derivative(2,1,k4*r3)...
    + spherical_bessel(2,1,k4*r3)) / e4;
    right_hand_side(6) = 0;
%% Fourth Boundary, r = r4
    %H field
    c_matrix(7,6) = spherical_bessel(1,1,k4*r4);
    c_matrix(7,7) = spherical_bessel(2,1,k4*r4);
    c_matrix(7,8) = -spherical_hankel(2,1,k5*r4);
    right_hand_side(7) = 0;
    %E field
    c_matrix(8,6) = (k4*r4*spherical_bessel_derivative(1,1,k4*r4)...
    + spherical_bessel(1,1,k4*r4)) / e4;
    c_matrix(8,7) = (k4*r4*spherical_bessel_derivative(2,1,k4*r4)...
    + spherical_bessel(2,1,k4*r4)) / e4;
    c_matrix(8,8) = -(k5*r4*spherical_hankel_derivative(2,1,k5*r4)...
    + spherical_hankel(2,1,k5*r4)) / e5;
    right_hand_side(8) = 0;
%% Solution of The System
    c_values = inv(c_matrix)*right_hand_side;
%% Poynting Vector

    c1 = c_values(1);
    h_phi_a = j*k1/2/pi * (1+1/j/k1/a) * exp(-j*k1*a) + c1*spherical_bessel(1,1,k1*a);
    e_theta_a = j*eta1*k1/2/pi * (1 + 1/j/k1/a - 1/(k1*a)^2) * exp(-j*k1*a)...
        - c1/j/w/e1/e0/a * (k1*a*spherical_bessel_derivative(1,1,k1*a)...
        + spherical_bessel(1,1,k1*a));
    poyn = e_theta_a*conj(h_phi_a); % The Poynting Vector is proportional to this value
    prad(count) = real(poyn); % radiated real power
    x_r(count) = imag(poyn)/real(poyn); % normalized reactance (equation 6.19)
```

```
    count = count+1;

end
hold on
plot(sweep/t1,abs(x_r)/abs(x_r(1)),'r') % plots normalized reactance ratio
plot(sweep/t1,abs(prad)/abs(prad(1)),'r') % plots radiated real power gain
```

References

[1] F. S. Azar. Imaging techniques for detecting breast cancer: Survey and perspectives. Technical Report MS-CIS-00-11, University of Pennsylvania Department of Computer and Information Science, Philadelphia, PA, 2000.

[2] S. Fletcher. False-positive screening mammograms: Good news, but more to do. *Ann Intern Med*, 131:60–62, July 1999.

[3] D. J. Paul. Picturing people: non-intrusive imaging. Technical report, Foresight Directorate, Office of Science and Technology, London, UK, February 2004.

[4] J. A. MacDonald et al. *Alternatives for Landmine Detection.* Santa Monica, CA, RAND Corporation, 2003.

[5] J. B. Pendry. Negative refraction makes perfect lens. *Phys. Rev. Lett.*, 85:3966–3969, October 2000.

[6] R. F. Soohoo. A microwave magnetic microscope. *J. Appl. Phys.*, 33:1276–1277, March 1962.

[7] E. A. Ash and G. Nicholls. Super-resolution aperture scanning microscope. *Nature*, 237:510–512, June 1972.

[8] L. Diener. Microwave near field imaging with open ended waveguide - comparison with other techniques of nondestructive testing. *Res Nondestr Eval*, 7:137–152, June 1995.

[9] D. E. Steinhauer, C. P. Vlahacos, S. K. Dutta, B. J. Feenstra, F. C. Wellstood, and S. M. Anlage. Quantitative imaging of sheet resistance with a scanning near-field microwave microscope. *Applied Physics Letters*, 72(7):861–863, 1998.

[10] S. M. Anlage, D. E. Steinhauer, C. P. Vlahacos, B. J. Feenstra, A. S. Thanawalla, H. Wensheng, S. K. Dutta, and F. C. Wellstood. Superconducting material diagnos-

tics using a scanning near-field microwave microscope. *Applied Superconductivity, IEEE Transactions on*, 9(2):4127–4132, June 1999.

[11] M. T. Ghasr, S. Kharkovsky, R. Zoughi, and R. Austin. Comparison of near-field millimeter-wave probes for detecting corrosion precursor pitting under paint. *IEEE Trans. Instrum. Meas.*, 54:1497–1504, August 2005.

[12] M. Tabib-Azar, P. S. Pathak, G. Ponchak, and S. LeClair. Nondestructive superresolution imaging of defects and nonuniformities in metals, semiconductors, dielectrics, composites, and plants using evanescent microwaves. *Rev. Sci. Instrum.*, 70:2783–2792, June 1999.

[13] S. Kalinin and A. Gruverman. *Scanning Probe Microscopy Electrical and Electromechanical Phenomena at the Nanoscale*, chapter I.7. Pringer, New York, NY, 2007.

[14] Y. Ju, M. Saka, and H. Abe. Microwave nondestructive detection of delamination in ic packages utilizing open-ended coaxial line sensor. *NDT and E International*, 32(5):259–264, July 1999.

[15] J. Yang, M. Saka, and H. Abe. Ndi of delamination in ic packages using millimeter-waves. *Instrumentation and Measurement, IEEE Transactions on*, 50(4):1019–1023, August 2001.

[16] M. Saka, J. Yang, D. Luo, and H. Abe. A method for sizing small fatigue cracks in stainless steel using microwaves. *JSME International Journal Series A*, 45(4):573–578, 2002.

[17] S. I. Ganchev, N. Qaddoumi, S. Bakhtiari, and R. Zoughi. Calibration and measurement of dielectric properties of finite thickness composite sheets with open-ended coaxial sensors. *Instrumentation and Measurement, IEEE Transactions on*, 44(6):1023–1029, December 1995.

[18] M. Tabib-Azar, D.-P. Su, A. Pohar, S. R. LeClair, and G. Ponchak. 0.4 mu m spatial resolution with 1 ghz ($\lambda = 30$ cm) evanescent microwave probe. *Review of Scientific Instruments*, 70(3):1725–1729, 1999.

[19] S. Hong, J. Kim, W. Park, and K. Lee. Improved surface imaging with a near-field scanning microwave microscope using a tunable resonator. *Appl. Phys. Lett.*, 80:524–526, January 2002.

[20] A. F. Lann, M. Golosovsky, D. Davidov, and A. Frenkel. Combined millimeter-wave near-field microscope and capacitance distance control for the quantitative mapping of sheet resistance of conducting layers. *Appl. Phys. Lett.*, 73:2832–2834, November 1998.

[21] C. Gao, T. Wei, F. Duewer, Y. Lu, and X. D. Xiang. High spatial resolution quantitative microwave impedance microscopy by a scanning tip microwave near-field microscope. *Appl. Phys. Lett.*, 71:1872–1874, September 1997.

[22] M. S. Boybay and O. M. Ramahi. Near-field probes using double and single negative media. In *Proc. of the NATO Advanced Research Workshop: Metamaterials for Secure Information and Communication Technologies*, pages 725–731, Marrakesh, Morocco, May 2008.

[23] M. S. Boybay and O. M. Ramahi. Near-field probes using double and single negative media. *Phys. Rev. E*, 79:016602, January 2009.

[24] J. B. Pendry, A. J. Holden, W. J. Stewart, and I. Youngs. Extremely low frequency plasmons in metallic mesostructures. *Phys. Rev. Lett.*, 76:4773–4776, June 1996.

[25] J. B. Pendry, A. J. Holden, D. J. Robbins, and W. J. Stewart. Magnetism from conductors and enhanced nonlinear phenomena. *IEEE Trans. Microwave Theory Tech.*, 47:2075–2084, November 1999.

[26] R. A. Shelby, D. R. Smith, and S. Schultz. Experimental verification of a negative index of refraction. *Science*, 292:77–79, April 2001.

[27] R. Marques, F. Medina, and R. Rafii-El-Idrissi. Role of bianisotropy in negative permeability and left-handed metamaterials. *Phys. Rev. B*, 65:144440, April 2002.

[28] J. D. Baena, L. Jelinek, R. Marques, and F. Medina. Near-perfect tunneling and amplification of evanescent electromagnetic waves in a waveguide filled by a metamaterial: Theory and experiments. *Phys. Rev. B*, 72:075116, August 2005.

[29] M. Ricci, N. Orloff, and S. M. Anlage. Superconducting metamaterials. *Apply. Phys. Lett.*, 87:034102, July 2005.

[30] K. Aydin, I. Bulu, and E. Ozbay. Subwavelength resolution with a negative-index metamaterial superlens. *Apply. Phys. Lett.*, 90:254102, June 2007.

[31] A. Grbic and G. V. Eleftheriades. Overcoming the diffraction limit with a planar left-handed transmission-line lens. *Phys. Rev. Lett.*, 92:117403, March 2004.

[32] S. Maslovski, S. Tretyakov, and P. Alitalo. Near-field enhancement and imaging in double planar polariton-resonant structures. *J. Appl. Phys.*, 96:1293–1300, August 2004.

[33] P. Alitalo, S. Maslovski, and S. Tretyakov. Three dimensional isotropic perfect lens based on lc loaded transmission lines. *J. Appl. Phys.*, 99:064912, March 2006.

[34] P. Alitalo, S. Maslovski, and S. Tretyakov. Experimental verification of the key properties of a three-dimensional isotropic transmission-line superlens. *J. Appl. Phys.*, 99:124910, March 2006.

[35] P. Alitalo and S. Tretyakov. Subwavelength resolution with three-dimensional isotropic transmission-line lenses. *Metamaterials*, 1:81–88, December 2007.

[36] M. K. Karkkainen and S. I. Maslovski. Wave propagation, refraction, and focusing phenomena in lorentzian double-negative materials: A theoretical and numerical study. *Microwave Opt. Technol. Lett.*, 37:4–7, April 2003.

[37] M. K. Karkkainen. Numerical study of wave propagation in uniaxially anisotropic lorentzian backward-wave slabs. *Phys. Rev. E*, 68:026602, August 2003.

[38] Y. Shi and C. H. Liang. Analysis of the double-negative materials using multi-domain pseudospectral time-domain algorithm. *Progress In Electromagnetics Research*, 51:153–165, 2005.

[39] D. Correia and J. M. Jin. 3d-fdtd-pml analysis of lefthanded metamaterials. *Microwave Opt. Technol. Lett.*, 40:201–205, February 2004.

[40] S. Foteinopoulou, E. N. Economou, , and C. M. Soukoulis. Refraction in media with a negative refractive index. *Phys. Rev. Lett.*, 90:107402, March 2003.

[41] D. Van Labeke and D. Barchiesi. Scanning-tunneling optical microscopy: a theoretical macroscopic approach. *J. Opt. Soc. Am.*, 9:732–739, May 1992.

[42] G. Binnig, H. Rohrer, C. Gerber, and E. Weibel. Tunneling through a controllable vacuum gap. *Applied Physics Letters*, 40(2):178–180, 1982.

[43] G. Binnig, H. Rohrer, Ch. Gerber, and E. Weibel. Surface studies by scanning tunneling microscopy. *Phys. Rev. Lett.*, 49(1):57–61, Jul 1982.

[44] G. Binnig and H. Rohrer. Scanning tunneling microscopy. *Surface Science*, 126(1-3):236 – 244, 1983.

[45] C. Girard and A. Dereux. Near-field optics theories. *Rep. Prog. Phys.*, 59:657–699, May 1996.

[46] C. Gao and X. D. Xiang. Quantitative microwave near-field microscopy of dielectric properties. *Review of Scientific Instruments*, 69(11):3846–3851, 1998.

[47] D. M. Pozar. *Microwave Engineering.* Wiley, Hoboken, NJ, 2005.

[48] C. Gao, F. Duewer, and X. D. Xiang. Quantitative microwave evanescent microscopy. *Apply. Phys. Lett.*, 75:3005–3007, November 1999.

[49] C. Gao, B. Hu, P. Zhang, M. Huang, W. Liu, and I. Takeuchi. Quantitative microwave evanescent microscopy of dielectric thin films using recursive image charge approach. *Apply. Phys. Lett.*, 84:4647–4649, June 2004.

[50] A. Imtiaz and S. M. Anlage. Effect of tip geometry on contrast and spatial resolution of the near field microwave microscope. *J. Appl. Phys*, 100:044304, August 2006.

[51] R. W. P. King. Electromagnetic field of a vertical dipole over an imperfectly conducting half-space. *Radio Science*, 25(2):149–160, March 1990.

[52] M. Golosovsky, E. Maniv, D. Davidov, and A. Frenkel. Near-field of a scanning aperture microwave probe: a 3-d finite element analysis. *Instrumentation and Measurement, IEEE Transactions on*, 51(5):1090–1096, Oct 2002.

[53] D. E. Steinhauer, C. P. Vlahacos, F. C. Wellstood, Steven M. Anlage, C. Canedy, R. Ramesh, A. Stanishevsky, and J. Melngailis. Quantitative imaging of dielectric permittivity and tunability with a near-field scanning microwave microscope. *Review of Scientific Instruments*, 71(7):2751–2758, 2000.

[54] J. H. Lee, S. Hyun, and K. Char. Quantitative analysis of scanning microwave microscopy on dielectric thin film by finite element calculation. *Review of Scientific Instruments*, 72(2):1425–1434, 2001.

[55] V. G. Vaselago. The electrodynamics of substances with simultaneously negative values of ϵ and μ. *Sov. Phys. Usp.*, 10:509–514, January 1968.

[56] D. R. Smith, W. J. Padilla, D. C. Vire, S. C. Nemat-Nasser, and S. Schults. Composite medium with simultaneously negative permeability and permittivity. *Phys. Rev. Lett.*, 84:4184–4187, May 2000.

[57] N. Garcia and M. Nieto-Vesperinas. Left-handed materials do not make a perfect lens. *Phys. Rev. Lett.*, 88:207403, May 2002.

[58] D. R. Smith, D. Schurig, M. Rosenbluth, S. Schultz, S. A. Ramakrishna, and J. B. Pendry. Limitations on sub-diffraction imaging with a negative refractive index slab. *Apply. Phys. Lett.*, 82:1506–1508, March 2003.

[59] J. B. Pendry. Negative refraction. *Contemp. Phys.*, 45:191–202, May 2004.

[60] D. R. Smith, J. B. Pendry, and M. C. K. Wiltshire. Metamaterials and negative refractive index. *Science*, 305:788–792, August 2004.

[61] S. A. Ramakrishna. Physics of negative index materials. *Rep. Prog. Phys.*, 68:449–521, January 2005.

[62] R. W. Ziolkowski and E. Heyman. Wave propagation in media having negative permittivity and permeability. *Phys. Rev. E*, 64:056625, October 2001.

[63] R. W. Ziolkowski and A. D. Kipple. Causality and double-negative metamaterials. *Phys. Rev. E*, 68:026615, August 2003.

[64] P. F. Loschialpo, D. L. Smith, D. W. Forester, F. J. Rachford, and J. Schelleng. Electromagnetic waves focused by a negative-index planar lens. *Phys. Rev. E*, 67:025602, February 2003.

[65] T. Wei, X. D. Xianga, W. G. Wallace-Freedman, and P. G. Schultz. Scanning tip microwave near-field microscope. *Appl. Phys. Lett.*, 68:3506–3508, June 1996.

[66] M. Tabib-Azar, J. L. Katz, and S. R. LeClair. Evanescent microwaves: A novel super-resolution noncontact nondestructive imaging technique for biological applications. *IEEE Trans. on Instr. and Meas.*, 48:1111–1116, December 1999.

[67] M. Tabib-Azar, N. S. Shoemaker, and S. Harris. Non-desctrutive characterization of materials by evanescent microwaves. *Meas. Sci. Technol.*, 4:583–590, May 1993.

[68] T. J. Cui, W. C. Chew, X. X. Yin, and W. Hong. Study of resolution and super resolution in electromagnetic imaging for half space problems. *IEEE Trans. Antennas Propagat.*, 52:1398–1411, June 2004.

[69] L. Zhao and T. J. Cui. Super-resolution imaging of dielectric objects using a slab of left handed material. *Apply. Phys. Lett.*, 89:141904, October 2006.

[70] X. S. Rao and C. K Ong. Amplification of evanescent waves in a lossy left-handed material slab. *Phys. Rev. B*, 68:113103, September 2003.

[71] N. Engheta and R. W. Ziolkowski. A positive future for double-negative metamaterials. *IEEE Trans. Microwave Theory Tech.*, 53:1535–1556, April 2005.

[72] P. Kolinko and D. Smith. Numerical study of electromagnetic waves interacting with negative index materials. *Opt. Express*, 11:640–648, April 2003.

[73] C. Caloz, C. C. Chang, and T. Itoh. Full-wave verification of the fundamental properties of left-handed materials in waveguide configurations. *J. Appl. Phys.*, 90:5483–5486, December 2001.

[74] N. Fang, Z. Liu, T. J. Yen, and X. Zhang. Regenerating evanescent waves from a silver superlens. *Opt. Express*, 11:682–687, April 2003.

[75] N. Fang and X. Zhang. Imaging properties of a metamaterial superlens. *Appl. Phys. Lett.*, 82:161–163, January 2003.

[76] R. F. Harrington. *Time-Harmonic Electromagnetic Fields.* McGraw-Hill, New York, NY, 1961.

[77] J. D. Jackson. *Classical Electrodynamics.* John Wiley & Sons Inc., New York, NY, 1999.

[78] J. A. Kong. *Electromagnetic Wave Theory.* John Wiley & Sons Inc., New York, NY, 1990.

[79] N. Engheta and R. W. Ziolkowski. *Electromagnetic Metamaterials: Physics and Engineering Explorations.* John Wiley & Sons Inc., Hoboken, NJ, 2006, pp. 10.

[80] T. J. Cui and J. A. Kong. Time-domain electromagnetic energy in a frequency-dispersive left-handed medium. *Phys. Rev. B*, 70:205106, November 2004.

[81] A. D. Boardman and K. Marinov. Electromagnetic energy in a dispersive metamaterial. *Phys. Rev. B*, 73:165110, August 2006.

[82] A. Taflove and S. C. Hagness. *Computational Electrodynamics: The Finite-Difference Time-Domain Method, 2nd ed.* Artech House, Norwood, MA, 2000.

[83] O. M. Ramahi. Complementary boundary operators for wave propagation problems. *J. Comput. Phys*, 133:113–128, May 1997.

[84] M. S. Boybay and O. M. Ramahi. Waveguide resonators for verification of enhancing evanescent field detection using metamaterials. In *Proc. IEEE AP-S Int. Symp.*, pages 1–4, San Diego, CA, June 2008.

[85] M. S. Boybay and O. M. Ramahi. Evanescent field detection using negative refractive index lenses. In *Proc. IEEE AP-S Int. Symp.*, pages 5507–5510, Honolulu, HI, June 2007.

[86] Y. Ju, M. Saka, and H. Abe. Detection of delamination in ic packages using the phase of microwaves. *NDT and E International*, 34(1):49–56, January 2001.

[87] J. P. Grant, R. N. Clarke, G. T. Symm, and N. M. Spyrou. In vivo dielectric properties of human skin from 50 mhz to 2.0 ghz. *Physics in Medicine and Biology*, 33(5):607–612, 1988.

[88] J. Baker-Jarvis, M. D. Janezic, P. D. Domich, and R. G. Geyer. Analysis of an open-ended coaxial probe with lift-off for nondestructive testing. *Instrumentation and Measurement, IEEE Transactions on*, 43(5):711–718, October 1994.

[89] S. Bakhtiari, S. I. Ganchev, and R. Zoughi. Analysis of radiation from an open-ended coaxial line into stratified dielectrics. *Microwave Theory and Techniques, IEEE Transactions on*, 42(7):1261–1267, July 1994.

[90] C. A. Balanis. *Antenna Theory Analysis and Design.* Wiley, Hoboken, NJ, 2005.

[91] R. W. Ziolkowski and A. D. Kipple. Application of double negative materials to increase the power radiated by electrically small antennas. *Antennas and Propagation, IEEE Transactions on*, 51(10):2626–2640, October 2003.

[92] J. B. Pendry, A. J. Holden, D. J. Robbins, and W. J. Stewart. Low frequency plasmons in thin-wire structures. *J. Phys.: Condens. Matter*, 10:4785–4809, June 1998.

[93] L. Yousefi and O. M. Ramahi. Engineered magnetic materials with improved dispersion using multi-resonator structures. In *Proc. of the 20th IEEE Canadian Conference on Electrical and Computer Engineering*, pages 966–969, Vancouver, Canada, April 2007.

[94] L. Yousefi and O. M. Ramahi. New artificial magnetic materials based on fractal hilbert curves. In *International Workshop on Antenna Technology: Small and Smart Antennas Metamaterials and Applications. IWAT '07.*, pages 237–240, Cambridge, U.K, March 2007.

[95] A. Erentok, R. W. Ziolkowski, J. A. Nielsen, R. B. Greegor, C. G. Parazzoli, M. H. Tanielian, S. A. Cummer, B.-I. Popa, T. Hand, D. C. Vier, and S. Schultz. Low frequency lumped element-based negative index metamaterial. *Appl. Phys. Lett.*, 91(18):184104, November 2007.

[96] G. V. Eleftheriades, A. K. Iyer, and P. C. Kremer. Planar negative refractive index media using periodically l-c loaded transmission lines. *IEEE Trans. Microwave Theory Tech.*, 50:2702–2712, December 2002.

[97] A. Grbic and G. V. Eleftheriades. Negative refraction, growing evanescent waves, and sub-diffraction imaging in loaded transmission-line metamaterials. *IEEE Trans. Microwave Theory Tech.*, 51:2297–2305, December 2003.

[98] K. Guven and E. Ozbay. Near field imaging in microwave regime using double layer split-ring resonator based metamaterial. *Opto-Electron. Rev.*, 14:213–216, September 2006.

[99] S. Maslovski, P. Ikonen, I. Kolmakov, S. Tretyakov, and M. Kaunisto. Artificial magnetic materials based on the new magnetic particle: Metaselanoid. *Progr. Electromagn. Res*, 54:61–81, 2005.

[100] X. Chen, T. Grzegorczyk, B. Wu, J. Pacheco, , and J. Kong. Robust method to retrieve the constitutive effective parameters of metamaterials. *Phys. Rev. E*, 70:016608, July 2004.

[101] D. R. Smith, S. Schultz, P. Markos, and C. M. Soukoulis. Determination of negative permittivity and permeability of metamaterials from reflection and transmission coefficients. *Phys. Rev. B*, 65:195104, November 2002.

[102] P. Markos and C. M. Soukoulis. Transmission properties and effective electromagnetic parameters of double negative metamaterials. *Optics Express*, 11(7):649–661, November 2003.

[103] M. S. Boybay and O. M. Ramahi. Experimental verification of sensitivity improvement in near field probes using single negative metamaterials. In *IMS 2009 : Proceedings of the IEEE MTT-S International Microwave Symposium*, Boston, MA, July 2009.

[104] E. D. V. Nagesh, G. Santosh Babua, V. Subramanian, V. Sivasubramanian, and V. R. K. Murthy. Two-dimensional microwave band-gap structures of different dielectric materials. *Pramana*, 65(6):1115–1120, 2005.

[105] M. S. Boybay and O. M. Ramahi. Double negative metamaterials for subsurface detection. In *Proceedings of the 29th Annual International Conference of the IEEE EMBS*, pages 3485–3488, Lyon, France, August 2007.

[106] C. Gabriel, S. Gabriel, and E. Corthout. The dielectric properties of biological tissues: I. literature survey. *Phys. Med. Biol.*, 41:2231–2249, November 1996.

[107] C. Gabriel, S. Gabriel, and E. Corthout. The dielectric properties of biological tissues: Ii. measurements in the frequency range 10 hz to 20 ghz. *Phys. Med. Biol.*, 41:2251–2269, November 1996.

[108] J. E. Hipp. Soil electromagnetic parameters as functions of frequency, soil density, and soil moisture. In *Proc. IEEE*, pages 98–103, January 1974.

[109] T. P. Montoya and G. S. Smith. Land mine detection using a ground-penetrating radar based on resistively loaded vee dipoles. *IEEE Trans. Antennas Propagat.*, 47:1795–1806, December 1999.

[110] C. Gabriel, S. Gabriel, and E. Corthout. The dielectric properties of biological tissues: Iii. parametric models for the dielectric spectrum of tissues. *Phys. Med. Biol.*, 41:2271–2293, November 1996.

[111] A. Grbic and G. V. Eleftheriades. A backward-wave antenna based on negative refractive index l-c networks. In *Proc. IEEE AP-S Int. Symp./USNC/URSI Nat. Radio Science Meeting*, pages 340–343, San Antonio, TX, June 2002.

[112] S. A. Ramakrishna and A. D. Armour. Propagating and evanescent waves in absorbing media. *Am. J. Phys.*, 71(6):562–567, June 2003.